國 立 交 通 大 學

電信工程學系碩士班

碩士論文

有近似週期性導引之 TDD-OFDMA 信號之頻率同步

Frequency-Synchronization for TDD-OFDMA Systems with Almost-Periodic Preamble

研 究 生：楊士賢　　Student: Shih-Hsien Yang

指導教授：蘇育德 博士　　Advisor: Dr. Yu Ted Su

中 華 民 國 九 十 五 年 七 月

有近似週期性導引之 TDD-OFDMA 信號之頻率同步

Frequency-Synchronization for TDD-OFDMA Systems with Almost-Periodic Preamble

研 究 生：楊士賢　　Student : Shih-Hsien Yang

指導教授：蘇育德 博士　　Advisor : Dr. Yu T. Su

國 立 交 通 大 學

電信工程學系碩士班

碩 士 論 文

A Thesis Submitted to
The Institute of Communication Engineering
College of Electrical Engineering and Computer Science
National Chiao Tung University
In Partial Fulfillment of the Requirements
For the Degree of Master of Science
In
Communication Engineering
July 2006

Hsinchu, Taiwan, Repubic of China

中華民國九十五年七月

有近似週期性導引之 TDD-OFDMA 信號之頻率同步

研究生：楊士賢　　指導教授：蘇育德 博士

國立交通大學電信工程學系碩士班

中文摘要

本文旨在研究 OFDMA 系統的頻率同步相關課題。跟一般 OFDM 系統不同的是來從事頻率同步的導引信號只具備近似的週期性。缺乏理想週期性的原因是由於離散傅立葉轉換大小為 2 的冪次方，無法被奇數整除。我們若仍然運用傳統基於週期性導引信號的相關性來做頻率估計的方法，其性能將可能很不理想。

我們利用內插法從接收的信號樣本中重建具完整週期性的導引信號，使得應用時域相關性的頻率偏移估測方法可以適當的使用而不至造成性能損失。我們會比較線性和基於 sinc 函數（即理想低通）的內插濾波器。如同我們所預期的，電腦模擬的結果顯示我們所提出的解決方法在 AWGN 和複徑衰退的通道下皆有性能的改善，尤以後者更為顯著。我們也觀察到性能增益與 OFDM 符號(或者 FFT)長度的有很大的關係。這個長度決定了非週期性的程度也直接影響了內插（或性能）增益的多寡。

Frequency-Synchronization for TDD-OFDMA Systems with Almost-Periodic Preamble

Student : Shih-Hsien Yang Advisor : Dr. Yu Ted Su

Department of Communications Engineering

National Chiao Tung University

Abstract

This thesis deals with the frequency synchronization issue of an OFDMA system. We consider the situation that the preamble used for synchronization and channel estimation has an almost-periodic structure. The lack of ideal periodicity is due to the fact that the discrete Fourier transform size, being a power of two, is not divisible by three. This non-periodicity causes the frequency synchronizer that assumes a periodic pilot structure to suffer from serious performance loss.

We propose an interpolation approach to reconstruct the received preamble samples in a periodic format so that conventional time-domain correlation-based frequency offset estimation algorithms become applicable. We examine both linear and sinc-based interpolation filters. Simulation results indicate that, as expected, the proposed solution brings about performance improvement in both AWGN and multipath fading channels. Significant performance enhancement is obtained in the latter case. We also observe that the performance gain is a function of the OFDM symbol (or FFT) size which determines the extent of non-periodicity and therefore the interpolation gain.

Contents

List of Figures

List of Tables

Chapter 1

Introduction

The Orthogonal Frequency Division Multiplexing (OFDM) technique enjoys several distinct advantages–multipath immunity, bandwidth efficiency, and resistance to narrowband interference–that make it a very attractive transmission scheme for high rate wireless communications.

It has been adopted in several international communication standards, e.g., digital audio broadcasting (DAB), digital video broadcasting-terrestrial (DVB-T), high performance local area networks (HIPERLAN/2) [7], IEEE 802.11a/g wireless local area networks (WLAN) [6], and very-high-speed digital subscriber line (VDSL). Recently, it has been used or is being considered in IEEE 802.11n , IEEE 802.16 [1]-[4], and IEEE 802.20. Some of these standards are likely to include the Multiple Input Multiple Output (MIMO) option for capacity enhancement.

The main difference between traditional frequency division multiplexing (FDM) and OFDM is that in OFDM, the spectra of the individual carriers do overlap. The overlapping property can increase the frequency efficiency in an OFDM system. Nevertheless, the OFDM carriers exhibit orthogonality over a symbol interval only if they are spaced in frequency domain exactly at the reciprocal of the symbol interval, which can be accomplished by using the discrete Fourier transform (DFT). Hence, a set of equally spaced subcarriers is used for parallel data transmission in OFDM systems.

Both intersymbol interference (ISI) and intercarrier interference (ICI) can be com-

pletely eliminated by inserting between symbols a small time interval known as a guard interval (GI). The length of the GI is made equal to or greater than the maximum delay spread of the class of multipath fading channels of concern. If the symbol signal waveform is extended periodically into the GI (normally referred to as cyclic prefix, CP), orthogonality of the carrier is maintained over the symbol period, thus eliminating ICI. ISI is also eliminated because successive symbols do not overlap due to the CP. Hence the receiver needs only to perform one-tap equalization, greatly reducing its complexity. Such an arrangement enables an OFDM-based system to overcome frequency selective fading in broadband wireless transmission and is the major reason for its current popularity.

With all its merits, OFDM systems, unfortunately, are far more sensitive to synchronization errors, especially the carrier frequency offset (CFO), than single-carrier systems. The CFO is caused by the misalignment in subcarrier frequencies due to fluctuations in transmitter and receiver radio frequency (RF) oscillators or the Doppler shift induced by the time-varying channel effect. This frequency offset can destroy the subcarrier orthogonality and introduces ICI. Hence, if the CFO is not properly estimated and compensated for, the ICI would cause significantly degradation of the bit-error-rate (BER) performance.

Therefore, the main purpose of frequency synchronizer is to ensure inter-carrier orthogonality. Various approaches have been proposed to estimate the CFO, either blindly or with the aid of pilot symbols and training sequences. Blind estimation algorithms achieve higher spectrum efficiency at the cost of increased complexity and slow convergence rate whence are not suitable for tracking time-varying CFO. An alternative design technique is data-aided estimation which inserts pilot tones in some or all subcarriers. It is a simpler method to obtain reliable estimate at the cost of lower effectively data rate [13].

OFDM can also be used in conjunction with a multiple access scheme. If frequency

division multiple access is employed then the resulting transmission technique is referred to as OFDMA. This scheme has been adopted by IEEE 802.16e [1]-[4]; it is proposed as a candidate air interface for the next generation broadband wireless networks [8]. In an OFDMA system, each user is assigned an exclusive set of orthogonal subcarriers for transmission. There are two major subcarrier-assignment schemes, namely, subband based and interleaved. The former scheme divides the whole bandwidth into small continuous subbands, and each user is assigned to one or several subbands. For the interleaved subcarrier assignment scheme, subcarriers assigned to different users are interleaved over the whole bandwidth. Both schemes, however, inherit from OFDM the weakness of being sensitive to frequency error. In an OFDMA system, CFO will further cause multiple-access interference (MAI) which might become the dominant factor that limits the system performance.

In this thesis, we use IEEE 802.16e standard (WiMAX) uplink as a model system for it has an almost-periodic pilot format that we are interested in. For the broadcast link (downlink) of the WiMAX system, CFO estimation is relatively simple since relative orthogonality among different users' assigned subcarriers can be maintained.

The remainder of this thesis is organized as follows. In Chapter 2, the system model and a time-domain correlation-based pilot-aided fractional CFO estimation method are introduced. Chapter 3 then presents two interpolations to generate periodic time-domain preamble for CFO estimation application. Based on the repetitive structure of the interpolated preamble, we examine the performance of the correlation-based algorithms in Chapter 4 in details. In Chapter 5, we further investigate the performance of the optimal maximum-likelihood frequency estimator and its simplified version. We extend our discussion to frequency synchronization of a subband-based OFDMA system in Chapter 6, assuming multiple preambles are available. A guard band between subbands is inserted so that signals from different users can be separated by filter banks. Existing CFO estimation algorithms can then be applied after each user signal is filtered. Finally,

we draw conclusion and suggest future works in Chapter 7.

Chapter 2

Frequency Synchronization with Almost-Periodic Preamble for TDD-OFDMA System

For practical OFDM(A) applications, data transmission is organized in frames, and training blocks (carrying known symbols) are located at the beginning of each frame for synchronization purposes. In this chapter, we will explore the downlink fractional CFO estimation based on the received preamble symbols.

2.1 OFDM System Fundamentals

OFDM is a multi-carrier transmission technique that subdivides the whole bandwidth into multiple frequency sub-carriers as shown in **Fig. 2.1**. In an OFDM system, the input data stream is divided into several parallel sub-streams of reduced data rate (thus increased symbol duration) and each sub-stream is modulated and transmitted on a separate orthogonal sub-carrier. The increased symbol duration improves the robustness of OFDM against the channel delay spread. Furthermore, the introduction of the CP can completely eliminate ISI as long as the CP duration is longer than the channel delay spread. The CP is typically a repetition of the last samples of data portion of the block that is appended to the beginning of the data payload as shown in **Fig. 2.2**. Hence, each time-domain OFDM symbol waveform contains a "useful interval" of

length T_u and CP with duration T_g. The value of T_g/T_u might be 1/4, 1/8, 1/16 and 1/32, depending on the transmission environment. The CP prevents inter-block interference and makes the channel appear circular and permits low-complexity frequency domain equalization. A perceived drawback of CP is that it introduces overhead, which effectively reduces bandwidth efficiency.

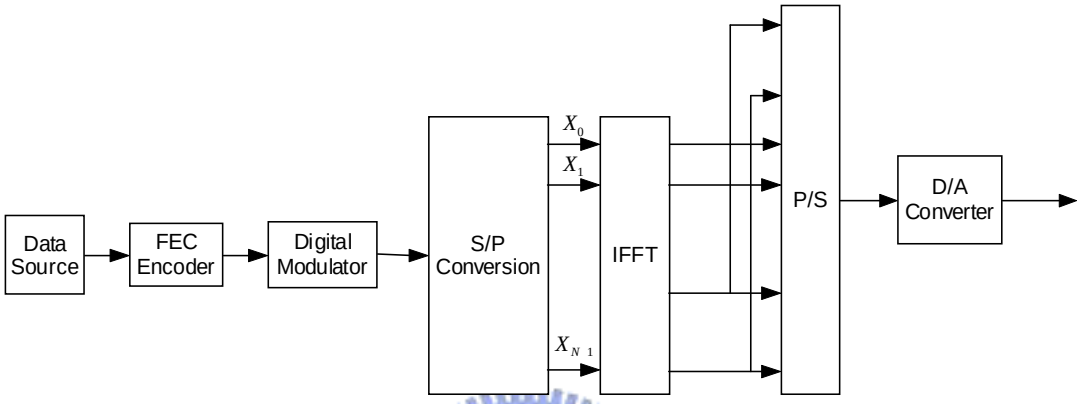

Figure 2.1: Block diagram of an OFDM transmitter.

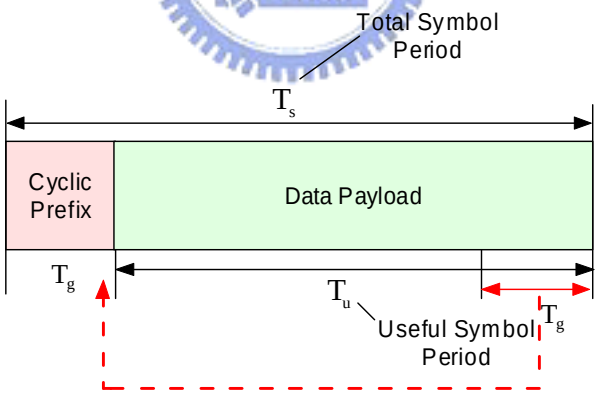

Figure 2.2: Insertion of Cyclic Prefix (CP).

A typical OFDM transmitter takes an N-point inverse discrete fourier transform (IDFT) on every block of N complex datas $\{X_k\}$ drawn from a QAM or PSK constellation before making parallel-to-serial conversion on the resulting time-domain block. An OFDM symbol (block) is then preceded by an N_g-sample cyclic prefix that is longer

than the maximum channel delay spread to form an "extended" symbol so that ISI can be eliminated at the receiving end by simply discarding the prefix part. The received (time-domain) OFDM signal, $y(n)$, are given by

$$\begin{aligned} y(n) &= \frac{1}{\sqrt{N}} \sum_{k=0}^{N-1} X_k H_k e^{\frac{j2\pi n(k+\varepsilon)}{N}} + w(n) \\ &= x(n) e^{\frac{j2\pi n\varepsilon}{N}} + w(n) \\ n &= -N_g, -(N_g - 1), ..., 0, 1, 2, ..., N-1 \end{aligned} \tag{2.1}$$

where the subscripts, n and k denote the nth OFDM sample in one OFDM block and the kth subcarrier, respectively. X_k is the transmitted frequency-domain complex data. H_k is the complex transfer function of the channel at the frequency of the kth subcarrier. $x(n)$ is the time-domain complex signal after passing X_k through a multipath channel without both CFO and AWGN effect. ε is the CFO normalized to the subcarrier spacing (assume the sampling interval is T_s (or T_u/N), the subcarrier spacing is $1/NT_s$ (or $1/T_u$)) and $w(n)$ denotes the samples of the complex envelop of AWGN.

2.2 OFDMA System Fundamentals

OFDMA is a multiple-access and multiplexing scheme that provides multiplexing operation of data streams from multiple users through the downlink sub-channels and uplink multiple access by means of uplink sub-channels. The OFDMA symbol structure consists of three types of sub-carriers as shown in **Fig. 2.3**.

- Data sub-carriers for data transmission
- Pilot sub-carriers for channel estimation and synchronization purposes
- Null sub-carriers for no transmission; used for guard bands and DC carriers

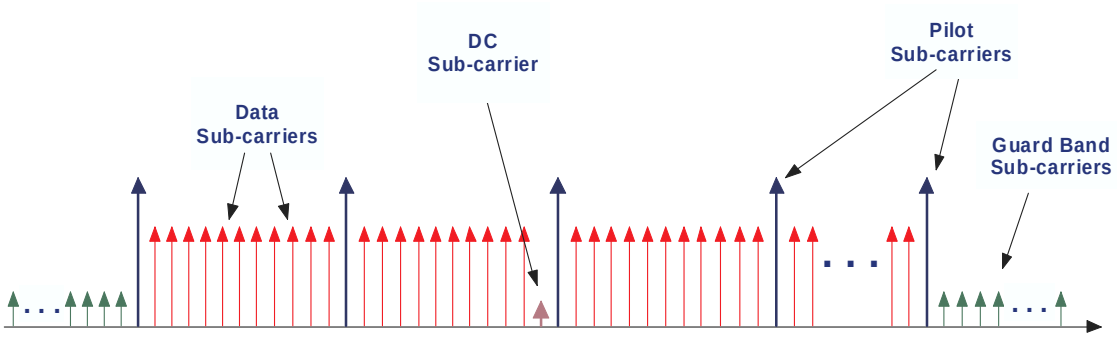

Figure 2.3: OFDMA Sub-Carrier Structure.

2.3 Downlink Structure

In IEEE 802.16e system, the downlink can be divided into a three segment structure and includes a preamble which begins the transmission. This preamble subcarriers are divided into three carrier-sets. There are three possible groups consisting of a carrier-set. Each of them may be used by any segment. A typical downlink period is illustrated in **Fig. 2.4**.

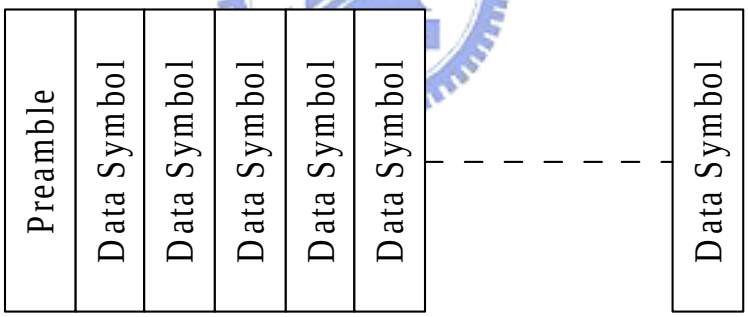

Figure 2.4: Basic structure of OFDMA downlink transmission.

2.3.1 Preamble Structure

The first symbol of the downlink transmission is the preamble. There are three types of preamble carrier-sets, those are defined by allocation of different subcarriers for each one of them. Those subcarriers are modulated using a boosted BPSK modulation with a specific Pseudo-Noise (PN) code. 114 preambles forms sequentially indexed with

	k	Guard Band Length (GB)	N_u
FFT size $(N) = 128$	-18 $\sim$ 17	10	54
FFT size $(N) = 512$	-72 $\sim$ 71	40	216
FFT size $(N) = 1024$	-142 $\sim$ 141	86	426
FFT size $(N) = 2048$	-284 $\sim$ 283	172	852

Table 2.1: Parameter setting of OFDMA downlink preamble.

$\{0, 1, ..., 113\}$. The 114 preamble forms can be divided into three segments indexed from segment 0 to segment 2 and every segment has 38 preamble forms. The preamble modulation series in Hexadecimal format can be found in Appendix A.

The preamble carrier-sets in frequency-domain are defined in (2.2),

$$PreambleCarrierSet_n = n + 3 \cdot k \tag{2.2}$$

where

- $PreambleCarrierSet_n$ specifies all subcarriers allocated to the specific preamble,
- n is the segment of the preamble carrier-set indexed 0...2,
- k is a running index defined as in **Tab. 2.1**.

Each segment uses one type of preamble composed of a carrier-set out of the three available carrier-sets in the following manner: (In the case of segment 0, the DC carrier will not be modulated at all and the appropriate PN will be discarded; therefore, DC carrier shall always be zeroed. For the preamble symbol, there will be GB guard band subcarriers defined as in **Tab. 2.1** on the left side and the right side of the spectrum.)

- Segment 0 uses preamble carrier-set 0
- Segment 1 uses preamble carrier-set 1
- Segment 2 uses preamble carrier-set 2

From above definition, (2.1) can be rewritten as

$$\begin{aligned} y(n) &= \frac{1}{\sqrt{N}} \sum_{k \in D_i} X_k H_k e^{\frac{j2\pi n(k+\varepsilon)}{N}} + w(n) \\ &= x(n) e^{\frac{j2\pi n\varepsilon}{N}} + w(n) \\ n &= -N_g, -(N_g - 1), ..., 0, 1, 2, ..., N - 1 \end{aligned} \tag{2.3}$$

where the subscripts, i denotes the ith segment, $D_i = \{-N_u+i, -N_u+i+3, ..., -3+i, 0+i, 3+i, ..., N_u-3+i\}$ is the set of modulated subcarrier indices and N_u is defined in **Tab. 2.1**. As an example, **Fig. 2.5** depicts the frequency-domain preamble structure of each segment for 128-point FFT size. The subcarrier locations of preamble in segment 1 and segment 2 are only circular frequency-shifting in segment 0. From circular frequency-shifting theorem [27], the inverse DFT of the circularly frequency-shifted DFT $X[k] = G[\langle k - k_0 \rangle_N]$, with k_0 an integer, is given by $x[n] = W_N^{-k_0 n} g[n]$, where $g[n]$ is the IDFT of $G[k]$ and W_N is defined as $e^{\frac{j2\pi}{N}}$; that is,

$$W_N^{-k_0 n} g[n] \Leftrightarrow G[\langle k - k_0 \rangle_N] \tag{2.4}$$

Hence, each segment has the same structure in time-domain but with some different phase rotation (or called linear phase shift).

From above, this preamble structure can be visualized as upsampling in frequency-domain [26]. A factor-of-L sampling rate expansion thus leads to a L-fold repetition of the original time-domain waveform, indicating that the inverse Fourier transform is compressed by a factor of L. Hence, in IEEE 802.16e preamble structure, every third subcarrier is used, preamble consists of three identical parts within an OFDM symbol. Figure 2.6 shows the structure of preamble in time domain, where N is the FFT length. Due to the periodic property, we can utilize the correlation between any two parts of the received (time-domain) preamble sequences to perform frequency synchronization.

Unfortunately, these three repetitions are not exactly the same, since the FFT size (N=128, 512, 1024, 2048) is not the multiple of 3. Hence, the N samples obtained from

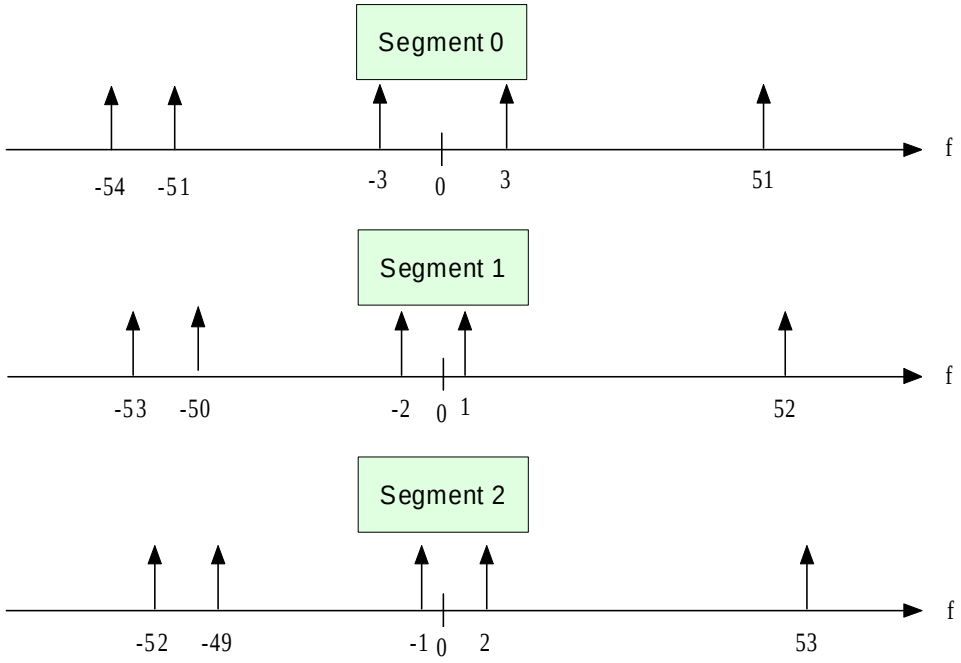

Figure 2.5: Frequency-domain structure of OFDMA downlink preamble for 128-point FFT size.

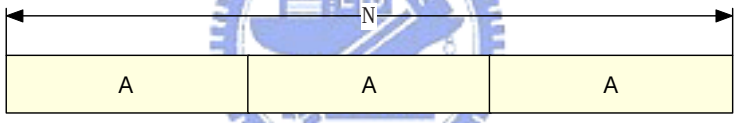

Figure 2.6: Time-domain preamble of TDD-OFDMA WiMAX system.

the A/D converter can not be divided by 3 exactly and will lead to three incomplete repetitions. The reason is owing to the samples obtained from the A/D converter is not complete. Therefore, this imperfectly repetitive structure in time-domain will lead to fault frequency synchronization. This almost-periodic property can be depicted in **Fig. 2.7**. The blue solid curve denotes the continuous waveform before the A/D converter and the red circles denote the discrete samples after the A/D converter. Hence, we can easily know that there is no alignment of the samples between any two parts of the three repetitions in **Fig. 2.7**.

A practical example for 128-point FFT size is shown in **Fig. 2.8** and we overlap

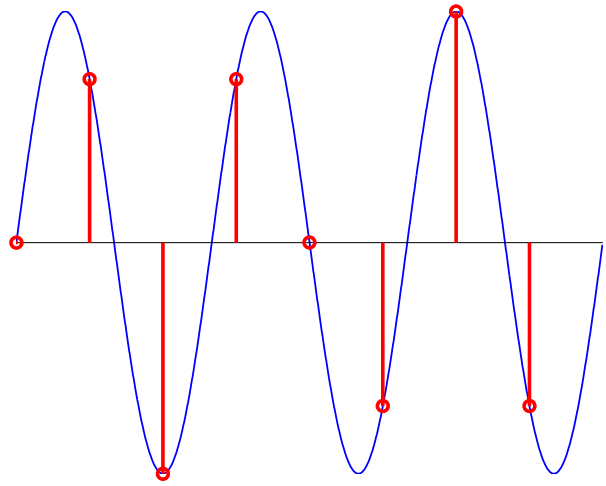

Figure 2.7: Almost-periodic preamble sequences in time-domain.

the three truncated repetition for demonstration. Because 128 is not multiple of 3 and the remainder of 128 divided by 3 is equal to 2, we discard two points (the 43-th point and the 86-th point) to keep the three incomplete repetition and utilize the three parts to implement correlation-based CFO estimation. Hence, repetition 1 is indexed from sample 1 to sample 42, repetition 2 is indexed from sample 44 to sample 85 and repetition 3 is indexed from sample 87 to sample 128.

2.4 Time-Domain Correlation-Based Fractional CFO Estimation by Using Almost-Periodic Preamble

After the division of preamble sequences as shown in **Fig. 2.8**, each part of the three sections can be considered as a repetition. Then, we will present four correlation-based algorithms for fractional CFO estimation. In the following, we still take 128-point FFT size ($N = 128$) as an applicable example and the other cases ($N = 512, 1024, 2048$) can also be implemented by the same way.

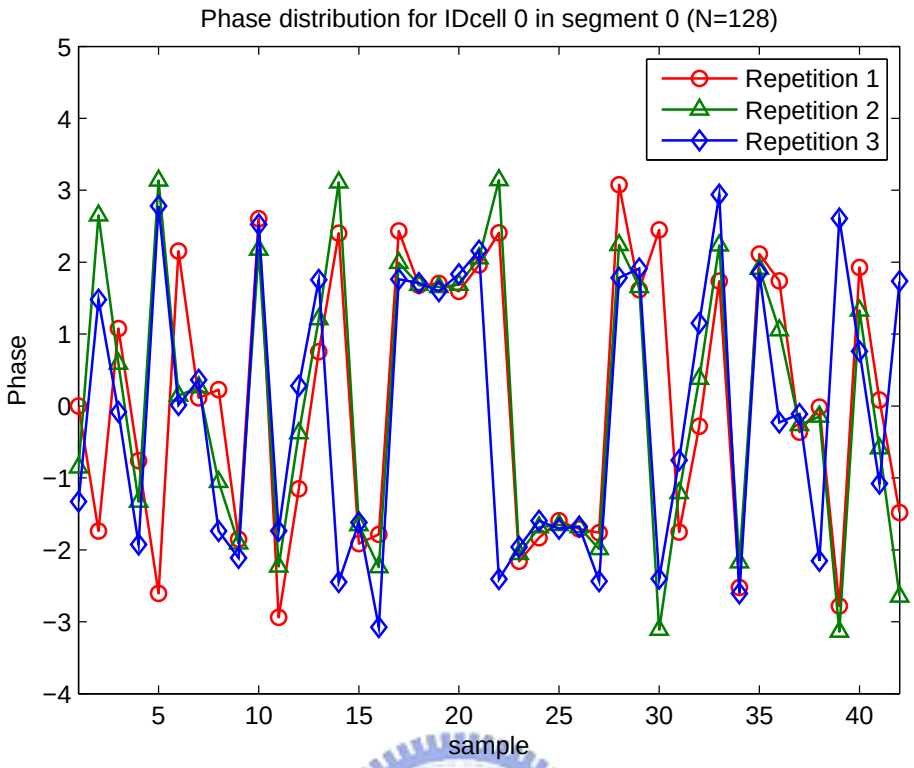

Figure 2.8: Illustration of the almost-periodic preamble samples for IDcell 0 preamble in segment 0.

2.4.1 Algorithm 1

First, we consider the correlation between the first two incomplete repetitions as shown in **Fig. 2.9**. According to (2.3), the sample-by-sample correlation function ignoring the noise effect can be written as

$$\begin{aligned}
\text{C1} &= \sum_{n=0}^{41} y(n)y(n+43)^* \\
&= \sum_{n=0}^{41} x(n)e^{j2\pi n\varepsilon/N} \cdot [x(n+43)e^{j2\pi(n+43)\varepsilon/N}]^* \\
&= \sum_{n=0}^{41} x(n)x(n+43)^* e^{j2\pi n\varepsilon/N} e^{-j2\pi(n+43)\varepsilon/N} \\
&= e^{-j2\pi\cdot 43\cdot\varepsilon/N} \sum_{n=0}^{41} x(n)\cdot x(n+43)^* \\
&= e^{-j86\pi\varepsilon/N}\cdot\Phi_1 \qquad (2.5)
\end{aligned}$$

where $\Phi_1 = \sum_{n=0}^{41} x(n) \cdot x(n+43)^*$ and $N = 128$.

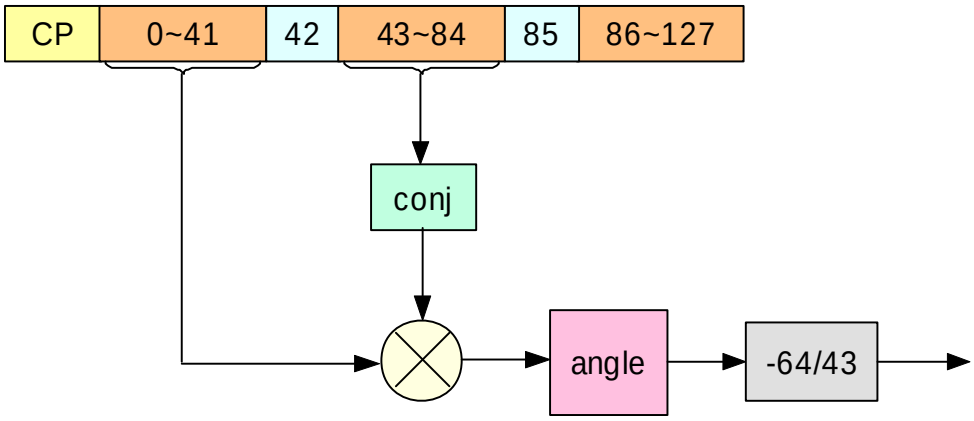

Figure 2.9: Block diagram of algorithm 1.

If we ignore the Φ_1 effect arises from the incomplete repetitions, the normalized CFO ε estimation can be obtained by using the phase of the correlation function C1 and is given by

$$\hat{\varepsilon_1} = -\frac{64}{43\pi}\angle \mathrm{C1}. \tag{2.6}$$

2.4.2 Algorithm 2

Then, we consider the correlation between the first and the third repetitions as shown in **Fig. 2.10**. According to (2.3), the sample-by-sample correlation function ignoring the noise effect can be written as

$$\begin{aligned}
\mathrm{C2} &= \sum_{n=0}^{41} y(n)y(n+86)^* \\
&= \sum_{n=0}^{41} x(n)e^{j2\pi n\varepsilon/N} \cdot [x(n+86)e^{j2\pi(n+86)\varepsilon/N}]^* \\
&= \sum_{n=0}^{41} x(n)x(n+86)^* e^{j2\pi n\varepsilon/N} e^{-j2\pi(n+86)\varepsilon/N} \\
&= e^{-j2\pi\cdot 86\cdot\varepsilon/N} \sum_{n=0}^{41} x(n)x(n+86)^* \\
&= e^{-j172\pi\varepsilon/N} \cdot \Phi_2
\end{aligned} \tag{2.7}$$

where $\Phi_2 = \sum_{n=0}^{41} x(n) \cdot x(n+86)^*$ and $N = 128$.

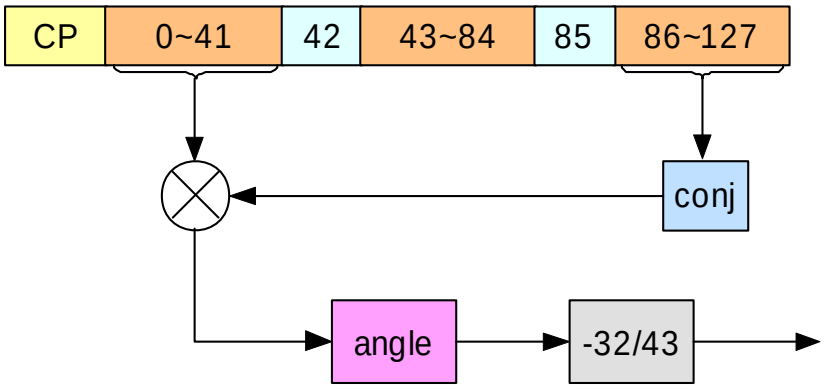

Figure 2.10: Block diagram of algorithm 2.

If we ignore the Φ_2 effect arises from the incomplete repetitions, the normalized CFO ε estimation can be obtained by using the phase of the correlation function C2 and is given by

$$\hat{\varepsilon_2} = -\frac{32}{43\pi}\angle \mathrm{C2}. \tag{2.8}$$

2.4.3 Algorithm 3

The algorithm 3 is a combination of algorithm 1 and algorithm 2 as shown in **Fig. 2.11**. Hence, the sample-by-sample correlation function can be obtained from the multiplication of C1 and C2 and is given by

$$\begin{aligned}
\mathrm{C3} &= \mathrm{C1} \times \mathrm{C2} \\
&= e^{-j86\pi\varepsilon/N} \sum_{n=0}^{41} x(n) \cdot x(n+43)^* \times e^{-j172\pi\varepsilon/N} \sum_{n=0}^{41} x(n)x(n+86)^* \\
&= e^{-j258\pi\varepsilon/N} \sum_{n=0}^{41} x(n) \cdot x(n+43)^* \times \sum_{n=0}^{41} x(n)x(n+86)^* \\
&= e^{-j258\pi\varepsilon/N} \Phi_1 \times \Phi_2 \\
&= e^{-j258\pi\varepsilon/N} \Phi_3
\end{aligned} \tag{2.9}$$

where $\Phi_3 = \Phi_1 \times \Phi_2$ and $N = 128$.

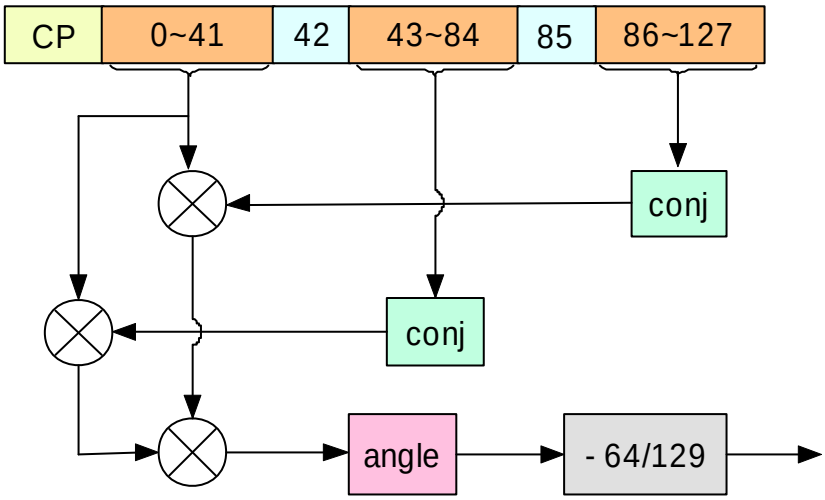

Figure 2.11: Block diagram of algorithm 3.

If we ignore the Φ_3 effect arises from the incomplete repetitions, the normalized CFO ε estimation can be obtained by using the phase of the correlation function C3 and is given by

$$\hat{\varepsilon}_3 = -\frac{64}{129\pi}\angle \mathrm{C3}. \tag{2.10}$$

2.4.4 Algorithm 4

Finally, the algorithm 4 is an extension of algorithm 1 by extending the length of the correlation window and is depict in **Fig. 2.12**.

$$\begin{aligned}
\text{C4} &= \sum_{n=0}^{41} y(n)y(n+43)^* \times \sum_{n=0}^{41} y(n+43)y(n+86)^* \\
&= \sum_{n=0}^{41} x(n)e^{j2\pi n\varepsilon/N} \cdot [x(n+43)e^{j2\pi(n+43)\varepsilon/N}]^* \times \\
&\quad \{\sum_{n=0}^{41} x(n+43)e^{j2\pi(n+43)\varepsilon/N} \cdot [x(n+86)e^{j2\pi(n+86)\varepsilon/N}]^*\} \\
&= \sum_{n=0}^{41} x(n)x(n+43)^* e^{j2\pi n\varepsilon/N} e^{-j2\pi(n+43)\varepsilon/N} \times \\
&\quad \sum_{n=0}^{41} x(n+43)x(n+86)^* e^{j2\pi(n+43)\varepsilon/N} e^{-j2\pi(n+86)\varepsilon/N} \\
&= e^{-j2\pi 86\varepsilon/N} \sum_{n=0}^{41} x(n)x(n+43)^* \times \sum_{n=0}^{41} x(n+43)x(n+86)^* \\
&= e^{-j172\pi\varepsilon/N}\Phi_4
\end{aligned} \tag{2.11}$$

where $\Phi_4 = \sum_{n=0}^{41} x(n)x(n+43)^* \times \sum_{n=0}^{41} x(n+43)x(n+86)^*$ and $N = 128$.

If we ignore the Φ_4 effect arises from the incomplete repetitions, the normalized CFO ε estimation can be obtained by using the phase of the correlation function C4 and is given by

$$\hat{\varepsilon_4} = -\frac{32}{43\pi}\angle\text{C4}. \tag{2.12}$$

2.5 Numerical Results and Discussion

Numerical results are provided in this section to demonstrate the performance of the four algorithms. The MSE is defined as

$$\text{MSE} = \frac{1}{M_c}\sum_{k=1}^{M_c}(\varepsilon - \hat{\varepsilon}(k))^2 \tag{2.13}$$

where M_c is the total Monte Carlo runs, and $\hat{\varepsilon}(k)$ is the normalized CFO estimate of the kth Monte Carlo run. From **Fig. 2.13** to **Fig. 2.15**, the four proposed estimators

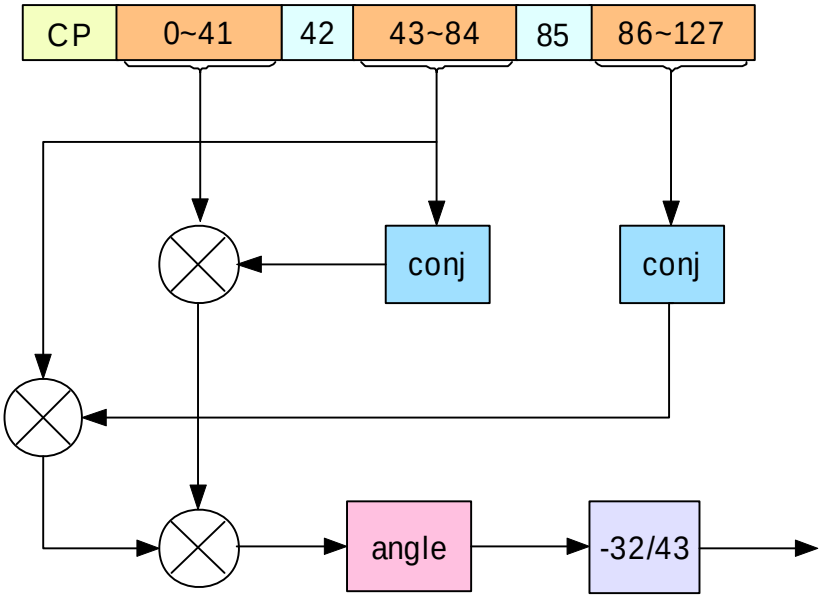

Figure 2.12: Block diagram of algorithm 4.

give good MSE performance in AWGN channel even if the three repetitions are not incomplete.

The frequency-selective fading channel is modelled as a linear FIR filter with impulse response given by

$$h(k) = \sum_{n=0}^{C_L-1} \alpha_n e^{-j\Phi} \delta(k-n) \tag{2.14}$$

where Φ is uniformly distributed in $[0, 2\pi)$ and α_n is Rayleigh distributed with an exponential power profile

$$\bar{\alpha_n^2} = (1 - e^{-T_s/T_{rms}}) e^{-nT_s/T_{rms}} \tag{2.15}$$

with $C_L = 16$, $T_{rms} = 30ns$ and $T_s = 50ns$. We use Jakes channel model with maximum Doppler shift of 500 Hz to simulate time-correlated Rayleigh fading α_n.

While multipath fading channel exists, the four proposed estimators give bad MSE performance if we do not do any things to deal with the three incomplete repetitions first; see **Fig. 2.16**, **Fig. 2.17** and **Fig. 2.18**. Even if the SNR is very high, the MSE of each algorithm is bounded at 10^{-2}.

Hence, in order to reduce the MSE of the four proposed estimators when multipath exists, we will introduce the interpolations in next chapter. The interpolations can be used to construct the losing samples from the existing samples by some proper weighting factor. Then, the three repetitions are nearly identical and the MSE performance will be better.

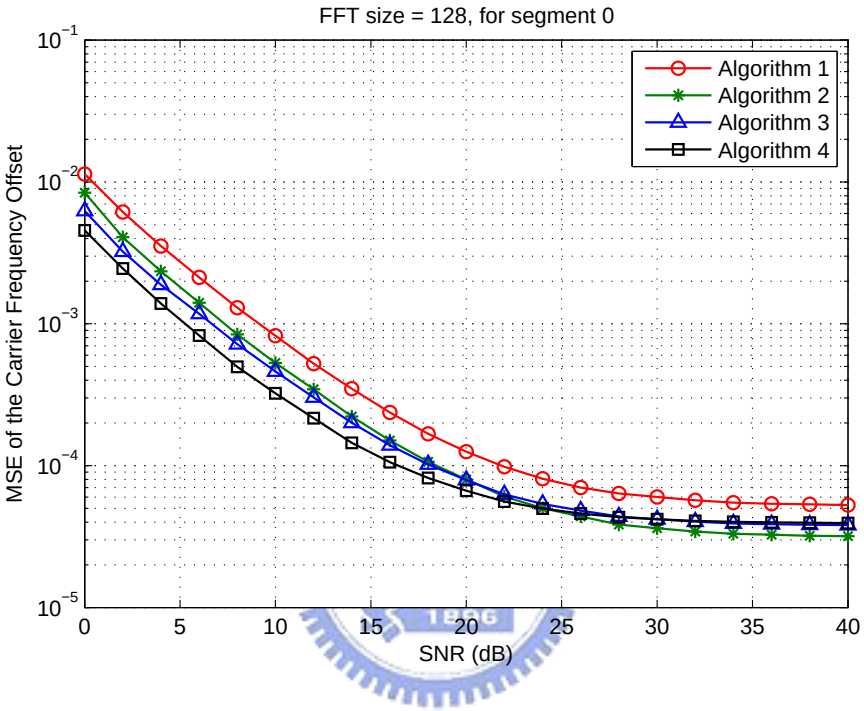

Figure 2.13: MSE of normalized CFO $\hat{\varepsilon}$ estimate as a function of the SNR in AWGN channel using IDcell 0 preamble in segment 0 without interpolation.

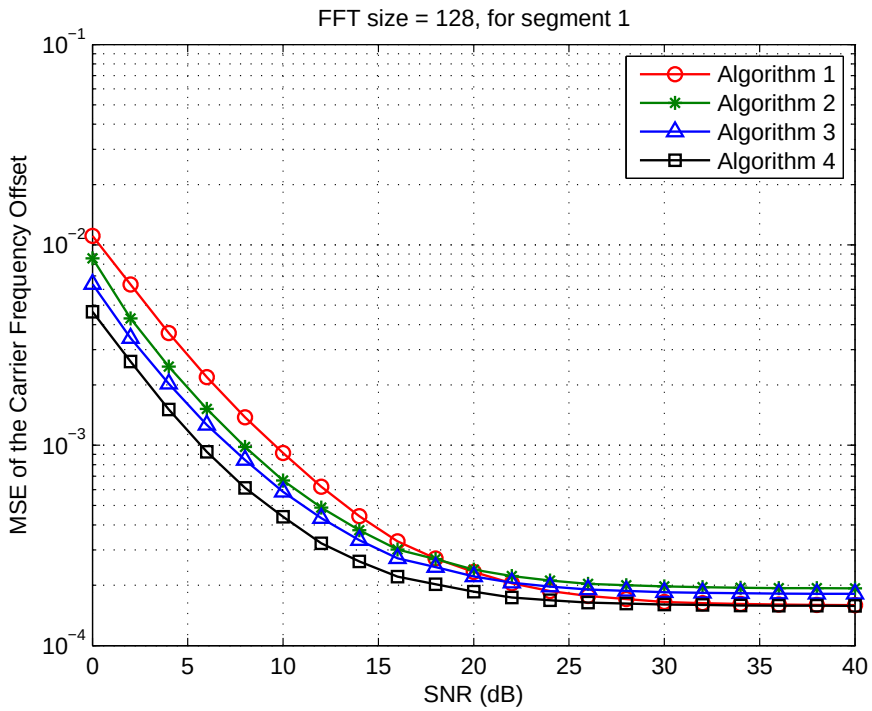

Figure 2.14: MSE of normalized CFO $\hat{\varepsilon}$ estimate as a function of the SNR in AWGN channel using IDcell 0 preamble in segment 1 without interpolation.

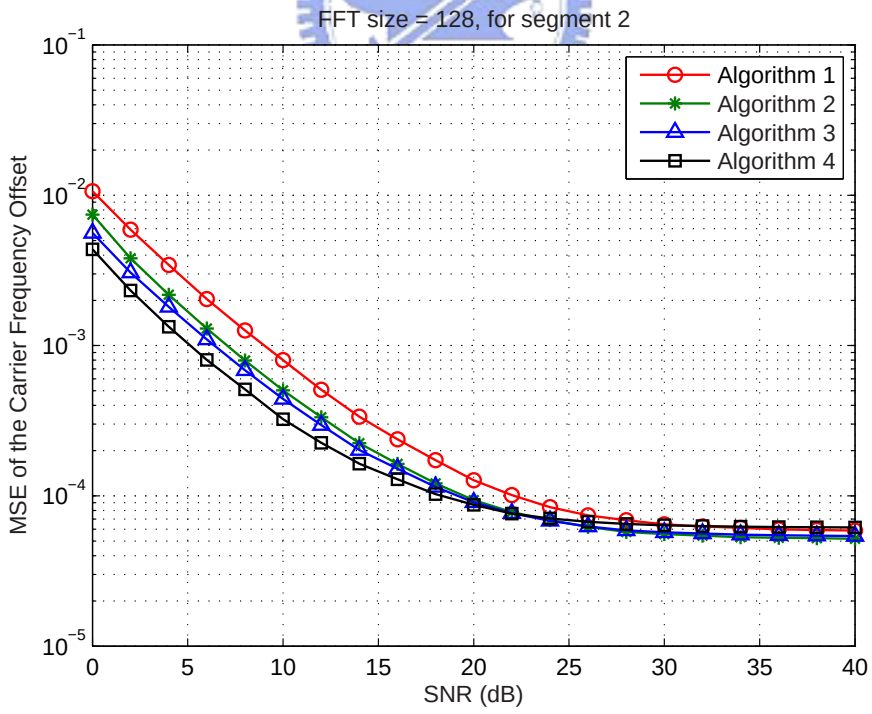

Figure 2.15: MSE of normalized CFO $\hat{\varepsilon}$ estimate as a function of the SNR in AWGN channel using IDcell 0 preamble in segment 2 without interpolation.

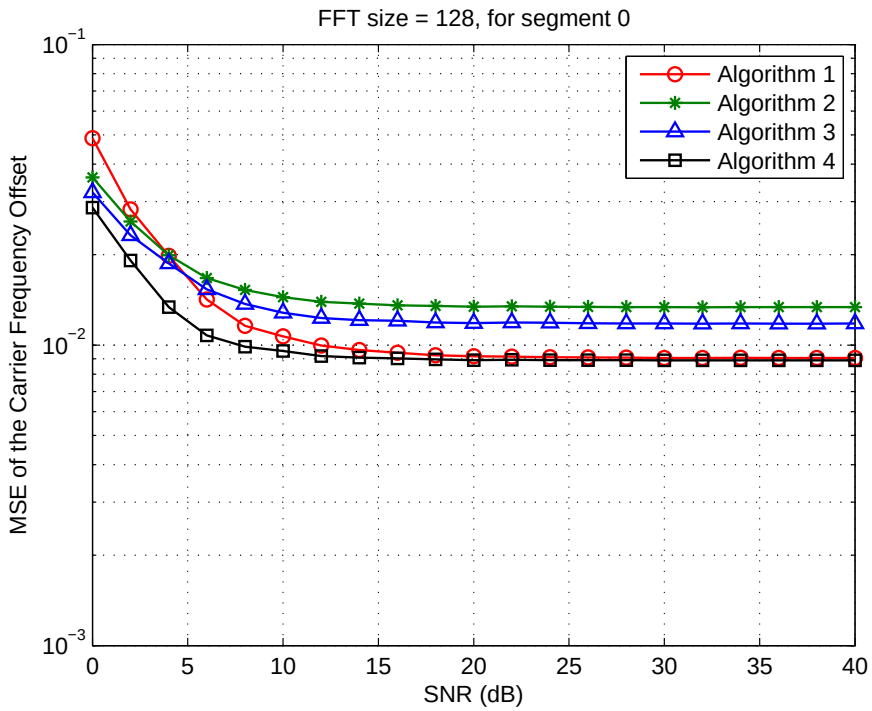

Figure 2.16: MSE of normalized CFO $\hat{\varepsilon}$ estimate as a function of the SNR in multipath fading channel using IDcell 0 preamble in segment 0 without interpolation.

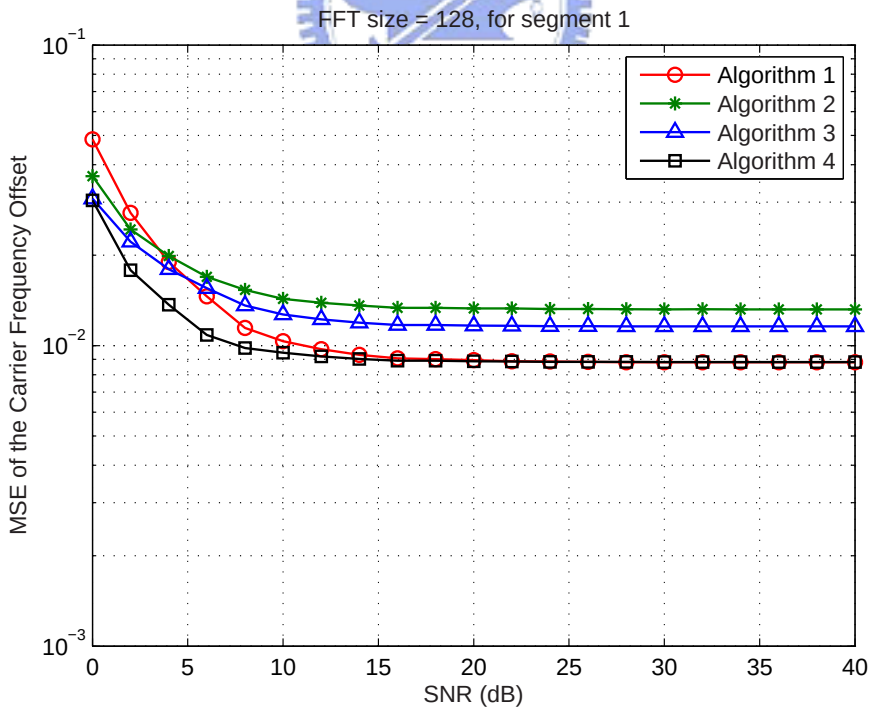

Figure 2.17: MSE of normalized CFO $\hat{\varepsilon}$ estimate as a function of the SNR in multipath fading channel using IDcell 0 preamble in segment 1 without interpolation.

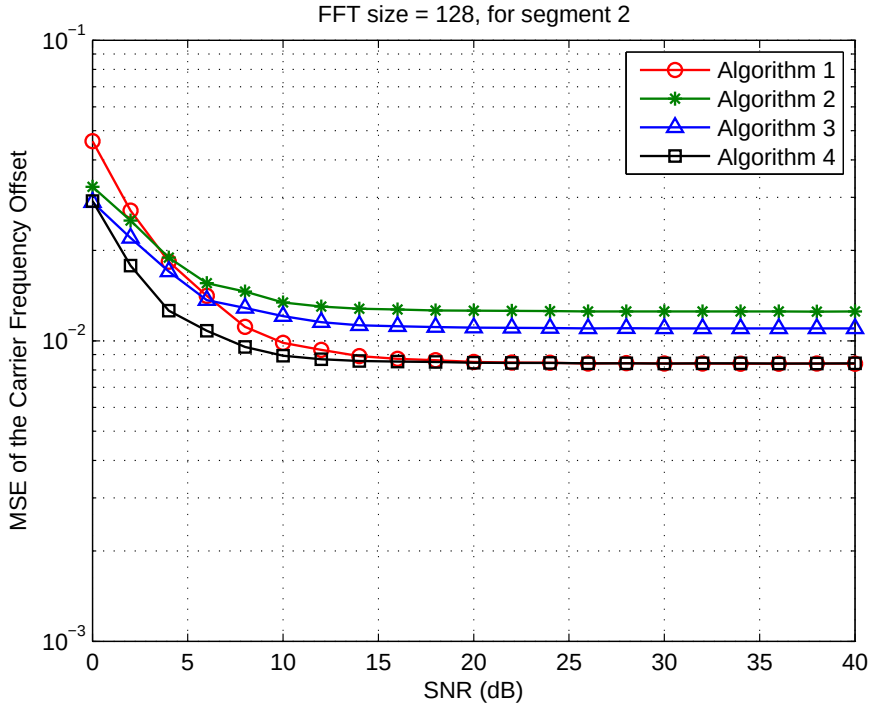

Figure 2.18: MSE of normalized CFO $\hat{\varepsilon}$ estimate as a function of the SNR in multipath fading channel using IDcell 0 preamble in segment 2 without interpolation.

Chapter 3

Interpolation Methods for Almost-Periodic Preamble in Time-Domain

In chapter 2, we have provided some general preamble-based fractional CFO estimation schemes for TDD OFDMA downlink system. However, the estimation performances are not very good especially when the multipath exists. The reason is that there is no alignment of the preamble samples between any two parts of the three incomplete repetitions as shown in **Fig. 2.7**. This property leads to fault correlation-based frequency synchronization. Hence, this chapter will develop two interpolation methods to reconstruct the complete preamble. Based on the interpolation methods, the correlation-based CFO estimation can be improved as well.

3.1 Oversampling

From **Fig. 2.7**, if we increase the sampling rate of the A/D converter by an integer factor of 3, we will have three completely identical parts. Then, the samples of the complex envelope of the received OFDM signal is given by

$$\begin{aligned} y_{os}(m) &= \frac{1}{\sqrt{N}} \sum_{k=0}^{N-1} X_k H_k e^{\frac{j2\pi m(k+\varepsilon)}{N}} + w(m) \\ &= x_{os}(m) e^{\frac{j2\pi m\varepsilon}{N}} + w(m) \\ m &= -N_g, -N_g + \frac{1}{3}, -N_g + \frac{2}{3}, -(N_g - 1), ..., 0, \frac{1}{3}, \frac{2}{3}, 1, 1\frac{1}{3}, ..., N - \frac{1}{3} \end{aligned} \quad (3.1)$$

where we assume that the oversampling interval is $T_u/3N$, T_u is the useful duration of one OFDMA block.

Then, the three perfectly repetitive structures in time domain can be obtained by oversampling if we ignore the channel, CFO, and noise effect; see **Fig. 3.1**. In **Fig. 3.1**, the red circles denote the originally discrete samples after the A/D converter without oversampling and the green squares denote the new samples obtained from oversampling. A practical example via oversampling for 128-point FFT size is shown in **Fig. 3.2**

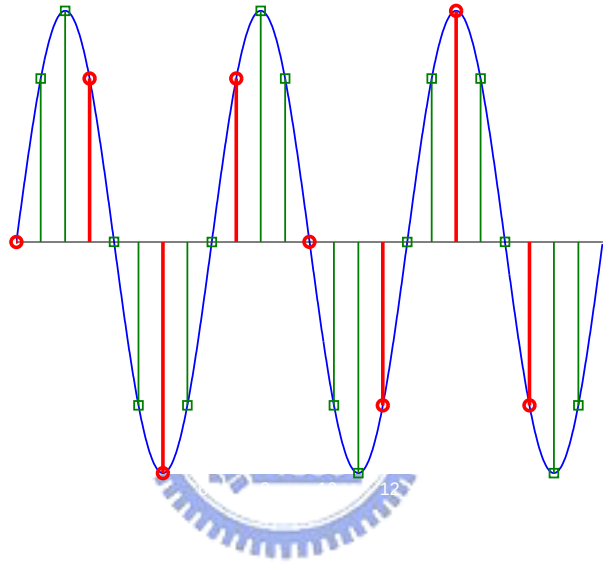

Figure 3.1: Preamble sequences via oversampling in time-domain.

In practical systems, however, to increase the sampling rate is almost impossible. Therefore, we should provide some alternative methods such as interpolations instead of oversampling. In order to obtain the green squares in **Fig. 3.1** without oversampling, we can utilize the original samples such as the red circles in **Fig. 3.1** to interpolate by taking weighted average. In the remaining of this chapter, some interpolations (either linear or sinc) will be presented. In other words, all these methods are based on the originally discrete samples (red circles) to generate the new samples (green squares). The detail description of the two interpolations will be introduced in **Sec. 3.2** and **Sec. 3.3** respectively.

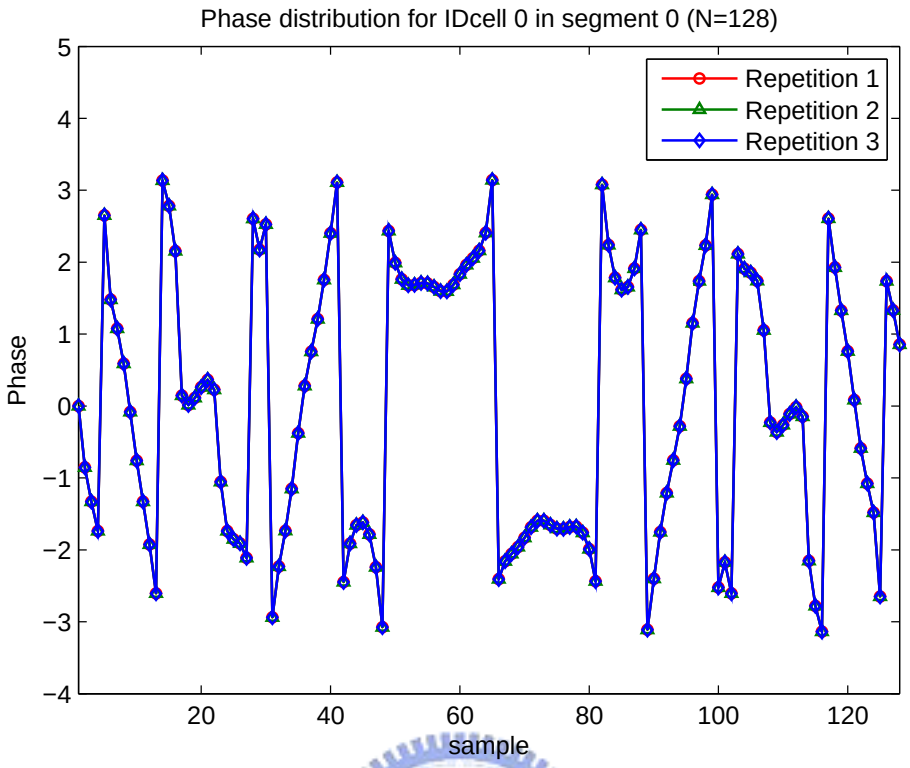

Figure 3.2: Three perfect preamble sequences via oversampling for IDcell 0 in segment 0.

3.2 Linear Interpolation

The first method is the linear interpolation that is often employed to estimate sample values between pairs of adjacent sample values of a discrete-time sequence. The linear interpolation is implemented by first passing the input sequence $y(n)$ to be interpolated through an up-sampler whose output $y_u(m)$ is then passed through a second discrete-time system that "fills in" the zero-valued samples inserted by the up-sampler with values obtained by a linear interpolation of the pair of input samples surrounding the zero-valued samples, as indicated in **Fig. 3.3**. In our case, we develop the input-output relation of a linear factor-of-3 interpolator. Hence, the output of the up-sampler can be

expressed as

$$y_u(m) = \begin{cases} y(n), & m = 3n \\ 0, & m = 3n+1 \\ 0, & m = 3n+2 \end{cases} \qquad 0 \le n \le N-1 \tag{3.2}$$

where $y(n)$ is the received preamble sequences after the A/D converter and is defined in (2.3).

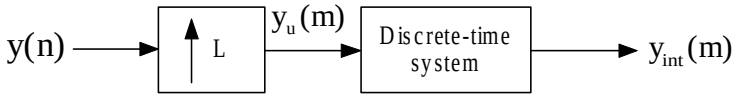

Figure 3.3: A factor-of-L interpolator.

The overall input-output relationship at the linear interpolator output can be written as

$$y_{linear}(m) = \begin{cases} y(n), & m = 3n \\ \frac{2}{3}y(n) + \frac{1}{3}y(n+1), & m = 3n+1 \\ \frac{1}{3}y(n) + \frac{2}{3}y(n+1), & m = 3n+2 \end{cases} \qquad 0 \le n \le N-1 \tag{3.3}$$

where $y_{linear}(m)$ is the output of the linear interpolator, and $(\frac{1}{3}, \frac{2}{3})$ are the weighting factors.

Here, if $y_u(m)$ is two zero-valued samples inserted between a pair of input samples, it is replaced with the average of the four original input samples, $y_u(m-2)$, $y_u(m-1)$, $y_u(m+1)$ and $y_u(m+2)$:

$$y_{linear}(m) = y_u(m) + \frac{2}{3}[y_u(m-1) + y_u(m+1)] + \frac{1}{3}[y_u(m-2) + y_u(m+2)]. \tag{3.4}$$

On the other hand, if $y_u(m)$ is one of the original input samples, its neighbors, $y_u(m-2)$, $y_u(m-1)$, $y_u(m+1)$ and $y_u(m+2)$ are all equal to 0. Hence, (3.4) can be expressed in convolution sum as

$$y_{linear}(m) \;=\; y_u(m) * h_{linear}(m) \qquad 0 \le m \le 3N-1 \tag{3.5}$$

where $h_{linear}(m)$ is the impulse response of the discrete-time system in **Fig. 3.3** and is

given by

$$h_{linear}(m) = \begin{cases} \frac{1}{3}, & m = -2 \\ \frac{2}{3}, & m = -1 \\ 1, & m = 0 \\ \frac{2}{3}, & m = 1 \\ \frac{1}{3}, & m = 2 \end{cases} \tag{3.6}$$

The interpolated samples thus lie on a straight line joining the pair of input samples, as illustrated in **Fig. 3.4** for a factor-of-3 linear interpolation. The green triangles denote the result of the linear interpolation and the orange dotted curve denotes the continuous waveform obtained from linear interpolation. From practical example, the repetitive property of the time-domain preamble sequences by linear interpolation can be shown in **Fig. 3.5**. Hence, linear interpolation is a feasible method to solve the foregoing problem.

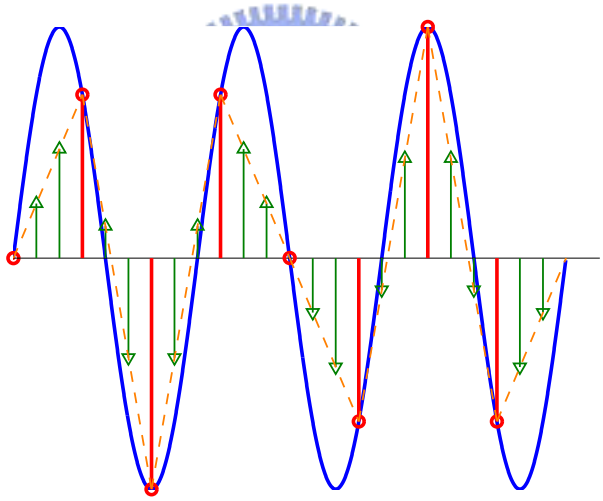

Figure 3.4: Illustration of the linear interpolation method.

3.2.1 Analysis of The Three Repetitive Structures via Linear Interpolation

In this subsection, we will compare the difference between any two parts of the three identical structures. A convenient way is to find the MSE. This result is shown in **Tab.**

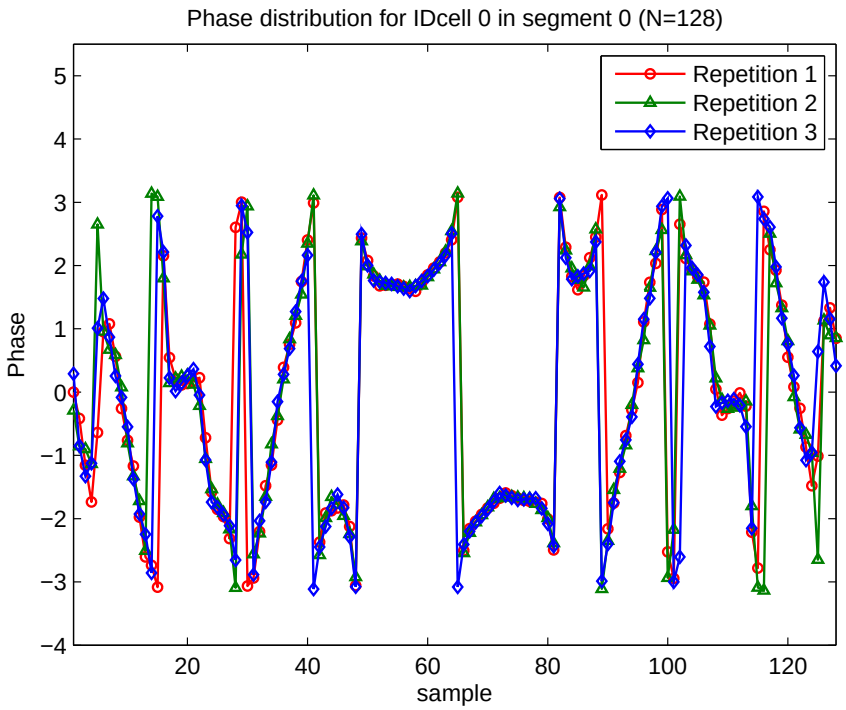

Figure 3.5: IDcell 0 preamble sequences in segment 0 via linear interpolation.

FFT size = 128 & IDcell = 0 in segment 0	MSE
repetition 1 & 2	0.1612×10^{-3}
repetition 2 & 3	0.1608×10^{-3}
repetition 1 & 3	0.1601×10^{-3}

Table 3.1: MSE between any two parts of the three repetitions by linear interpolation.

3.1. Although the MSE is quite small, there is little amount of information since each reconstructed sample is interpolated by only two neighboring samples. Therefore, this method is suboptimal and then we will present a better method in the next section.

3.3 Sinc Interpolation

The second method is sinc interpolation which is derived from the sampling theorem. We can utilize the sinc function to reconstruct the new samples from old samples. Likewise, it can be easily shown that for a factor-of-3 sinc interpolator, the discrete-time

system following the factor-of-3 up-sampler as illustrated in **Fig. 3.3** is characterized by the input-output relation written as

$$y_{sinc}(m) = y_u(m) * h_{sinc}(m) \qquad 0 \leq m \leq 3N-1 \tag{3.7}$$

where $h_{sinc}(m)$ is the impulse response of the discrete-time system in **Fig. 3.3** and is given by

$$h_{sinc}(m) = \text{sinc}(\frac{m}{3}) \qquad -3L \leq m \leq 3L \tag{3.8}$$

with L is the truncated sidelobe length of the sinc function. **Fig. 3.6** illustrates the impulse response of $h_{sinc}(m)$ with $L = 5$.

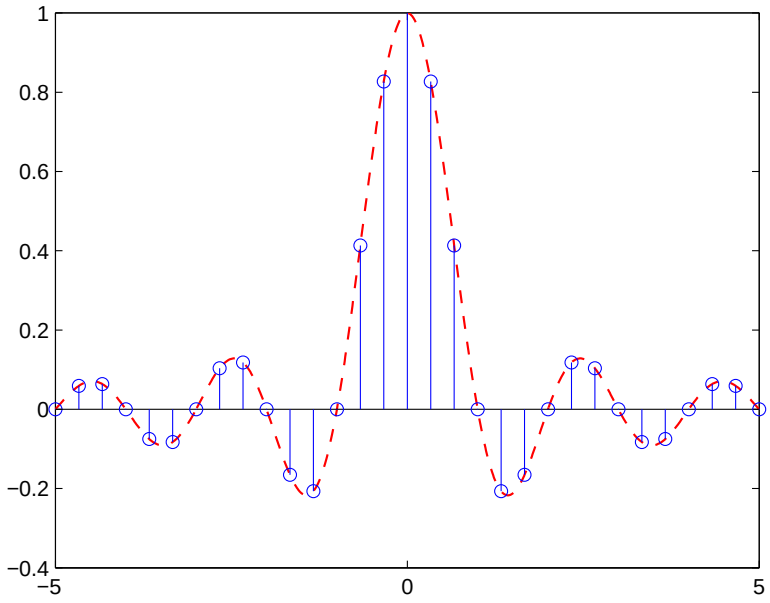

Figure 3.6: The impulse response of $h_{sinc}(m)$ with $L = 5$.

In **Fig. 3.7**, the black triangles denote the result of sinc interpolation. From practical examples, the repetitive property of the time-domain preamble sequences by sinc interpolation can be shown in **Fig. 3.8**. This result reveals that the sinc interpolation is more accurate than linear interpolation but with higher computational complexity.

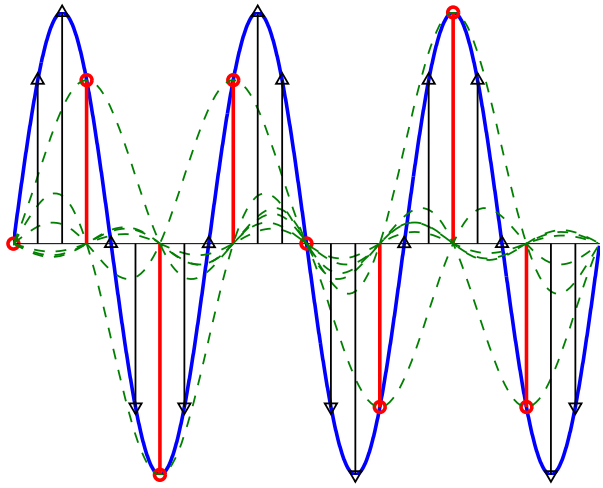

Figure 3.7: Illustration of the sinc interpolation method.

3.3.1 Analysis of The Three Repetitive Structures via Sinc Interpolation

Likewise, we still compare the difference between any two parts of the three repetitive structures. The MSE as a function of the sidelobe length is shown in **Fig. 3.9**. Hence, in order to achieve the MSE of 10^{-4}, the sidelobe length of 5 ($L = 5$) is enough.

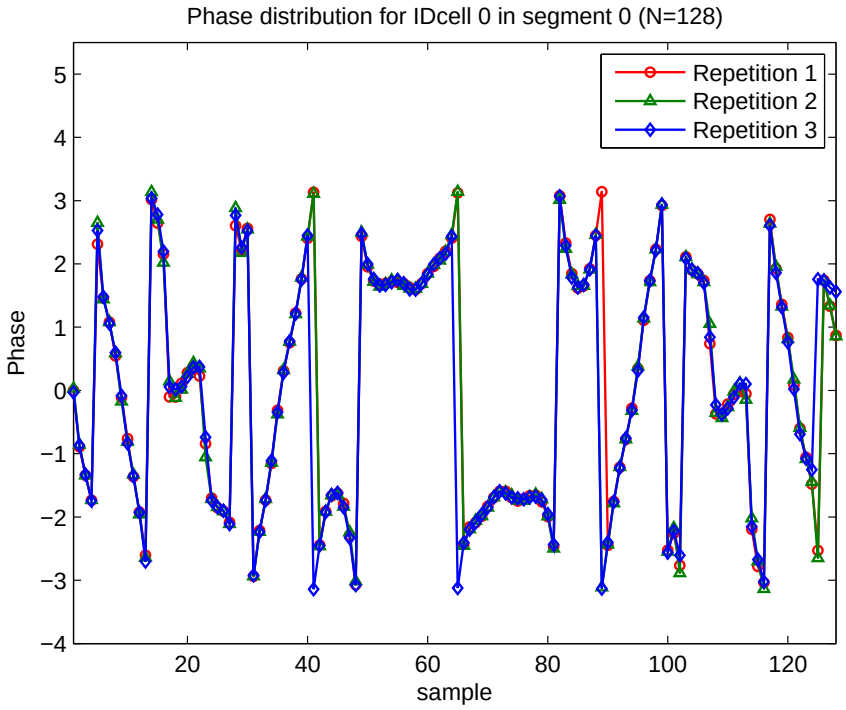

Figure 3.8: IDcell 0 preamble sequences in segment 0 via sinc interpolation with side-lobe length = 5.

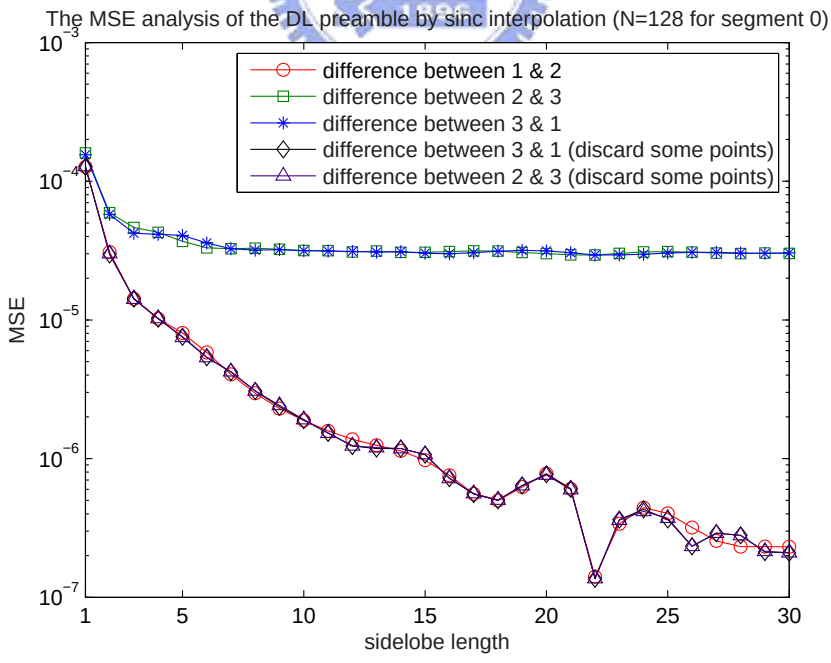

Figure 3.9: MSE between any two parts of the three repetition via sinc interpolation.

Chapter 4

Downlink Pilot-Assisted Frequency Synchronization via Interpolation

After the interpolations (either linear or sinc) introduced in chapter 3, we will have three repetitive structures. Based on the three repetitive structures, the correlation between the three repetitive samples in time-domain can be used to perform CFO estimation. This chapter still presents the same correlation-based algorithms as introduced in chapter 2 for CFO estimation but with interpolation. Hence, the four algorithms should be modified properly. Besides, the performance of the identical algorithms without interpolation is also illustrated. Finally, the simulation results verify the superior performance of the proposed methods (interpolations) with regard to estimation accuracy.

4.1 Repetitive Structure of Interpolated Preamble

The structure of the factor-of-3 interpolated preamble sequences with index set $\{0, 1, ..., 3N-1\}$ is illustrated in **Fig. 4.1**, where samples connected together by the same arrow-line are almost identical. After the factor-of-3 interpolation, in addition to the original N preamble samples, we will have additional $2N$ samples obtained from interpolations. In **Fig. 4.1**, the N original preamble samples are indexed with $\{0, 3, ..., 3(N-1)\}$, and the interpolated samples are indexed with $\{1, 2, ..., 3N-2, 3N-1\}$. Therefore, the total $3N$ samples are multiple of 3, and there is no misalignment

when the sample-by-sample correlation is implemented. Consequently, repetition 1 is indexed with $\{0, 1, ..., N-1\}$, repetition 2 is indexed with $\{N, N+1, ..., 2N-1\}$, and repetition 3 is indexed with $\{2N, 2N+1, ..., 3N-1\}$.

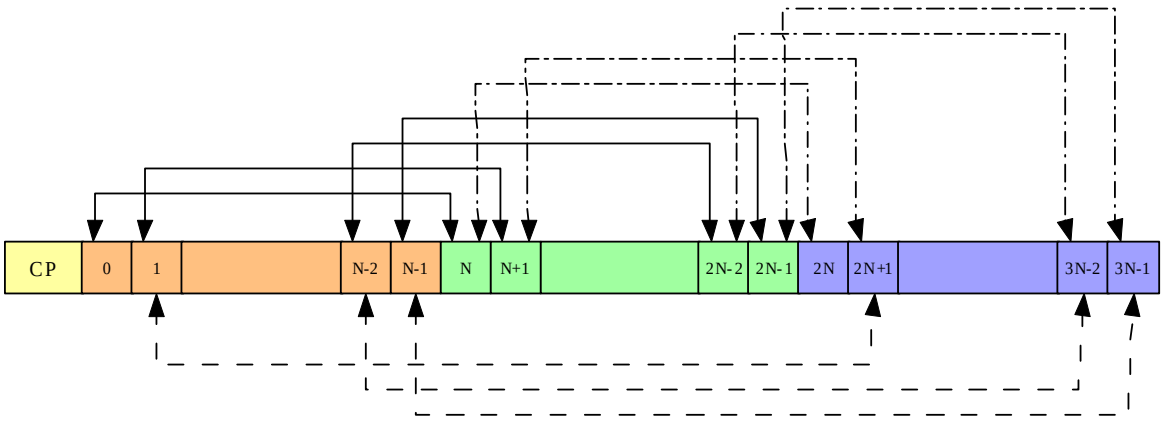

Figure 4.1: Structure of a interpolated preamble symbol, where samples connected together by the same arrow-line are almost identical.

From above descriptions, the four algorithms introduced in chapter 2 can be performed well without discarding some samples and only require some modifications when interpolation exists. The modification of each algorithm is described in detail in the next section.

4.2 Time-Domain Correlation-based Fractional CFO Estimation by Using Almost-Periodic Preamble with Interpolations

If we neglect the inaccuracy of the interpolated samples and AWGN effect, **THREE** conditions are satisfied in a preamble symbol

- ***Condition 1 :***

$$y_{int}(m) = \ y_{int}(m+N) \quad 0 \leq m \leq N-1 \tag{4.1}$$

- ***Condition 2 :***

$$y_{int}(m+N) = \ y_{int}(m+2N) \quad 0 \le m \le N-1 \tag{4.2}$$

- ***Condition 3 :***

$$y_{int}(m) = \ y_{int}(m+2N) \quad 0 \le m \le N-1 \tag{4.3}$$

where $y_{int}(m)$ is the output of the interpolator either form linear interpolation $y_{linear}(m)$ or from sinc interpolation $y_{sinc}(m)$.

Because we neglect the inaccuracy of the interpolated samples, the output of the interpolator $y_{int}(m)$ is equal to the oversampling sample $y_{os}(m)$ as defined in (3.1). Consequently, we can utilize (3.1) to modify the four algorithms as introduced in chapter 2 in the following. For derivation purpose, (3.1) can be rewritten as

$$\begin{aligned} y_{os}(m) &= \frac{1}{\sqrt{N}} \sum_{k=0}^{N-1} X_k H_k e^{\frac{j2\pi m(k+\varepsilon)}{3N}} + w(m) \\ &= x_{os}(m) e^{\frac{j2\pi m\varepsilon}{3N}} + w(m) \qquad 0 \le m \le 3N-1 \end{aligned} \tag{4.4}$$

where m is an integer. Hence, we can replace $y_{os}(m)$ with $y_{int}(m)$ and replace $x_{os}(m)$ with $x_{int}(m)$ respectively.

4.2.1 Modified Algorithm 1 via Interpolations

First, we consider the correlation between the first two repetitions satisfing condition 1 as shown in **Fig. 4.2**. If we ignore the noise effect, the sample-by-sample correlation

function can be written as

$$\begin{aligned}
\text{C1} &= \sum_{m=0}^{N-1} y_{int}(m) y_{int}(m+N)^* \\
&= \sum_{m=0}^{N-1} x_{int}(m) e^{j2\pi m\varepsilon/3N} \cdot [x_{int}(m+N) e^{j2\pi(m+N)\varepsilon/3N}]^* \\
&= \sum_{m=0}^{N-1} x_{int}(m) x_{int}(m+N)^* e^{j2\pi m\varepsilon/3N} e^{-j2\pi(m+N)\varepsilon/3N} \\
&= e^{-j2\pi N\varepsilon/3N} \sum_{m=0}^{N-1} \|x_{int}(m)\|^2 \\
&= e^{-j2\pi\varepsilon/3} \sum_{m=0}^{N-1} \|x_{int}(m)\|^2 \qquad (4.5)
\end{aligned}$$

where $y_{int}(m)$ is the output of the interpolator either form linear interpolation $y_{linear}(m)$ or from sinc interpolation $y_{sinc}(m)$.

The normalized CFO ε is estimated using the phase of the correlation function and is given by

$$\hat{\varepsilon}_1 = -\frac{3}{2\pi} \angle \text{C1}. \qquad (4.6)$$

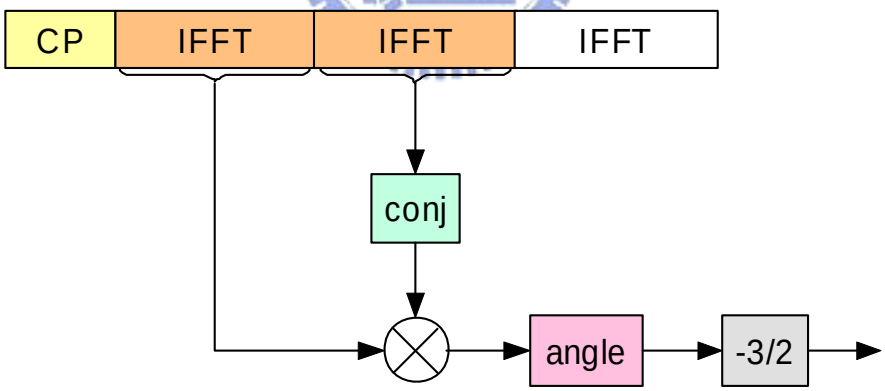

Figure 4.2: Block diagram of modified algorithm 1 via interpolations.

4.2.2 Modified Algorithm 2 via Interpolations

Then, we consider the correlation between the first and the third repetitions satisfying condition 3 as shown in **Fig. 4.3**. If we ignore the noise effect, the sample-by-sample

correlation function can be written as

$$\begin{aligned} \text{C2} &= \sum_{m=0}^{N-1} y_{int}(m) y_{int}(m+2N)^* \\ &= \sum_{m=0}^{N-1} x_{int}(m) e^{j2\pi m\varepsilon/3N} \cdot [x_{int}(m+2N) e^{j2\pi(m+2N)\varepsilon/3N}]^* \\ &= \sum_{m=0}^{N-1} x_{int}(m) x_{int}(m+2N)^* e^{j2\pi m\varepsilon/3N} e^{-j2\pi(m+2N)\varepsilon/3N} \\ &= e^{-j2\pi 2N\varepsilon/3N} \sum_{m=0}^{N-1} \|x_{int}(m)\|^2 \\ &= e^{-j4\pi\varepsilon/3} \sum_{m=0}^{N-1} \|x_{int}(m)\|^2 \end{aligned} \tag{4.7}$$

where $y_{int}(m)$ is the output of the interpolator either form linear interpolation $y_{linear}(m)$ or from sinc interpolation $y_{sinc}(m)$.

The normalized CFO ε is estimated using the phase of the correlation function and is given by

$$\hat{\varepsilon}_2 = -\frac{3}{4\pi} \angle C2. \tag{4.8}$$

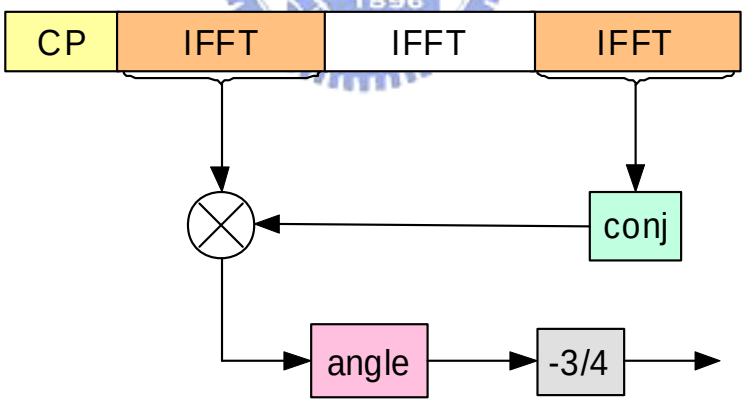

Figure 4.3: Block diagram of modified algorithm 2 via interpolations.

4.2.3 Modified Algorithm 3 via Interpolations

Algorithm 3 is a combination of algorithm 1 and algorithm 2, and is shown in **Fig. 4.4**. Hence, the sample-by-sample correlation function can be obtained from the

multiplication of C1 and C2 and is given by

$$\begin{aligned} \text{C3} &= \text{C1} \times \text{C2} \\ &= e^{-j2\pi\varepsilon/3} \sum_{m=0}^{N-1} \|x_{int}(m)\|^2 \times e^{-j4\pi\varepsilon/3} \sum_{m=0}^{N-1} \|x_{int}(m)\|^2 \\ &= e^{-j2\pi\varepsilon} \{\sum_{m=0}^{N-1} \|x_{int}(m)\|^2\}^2 \end{aligned} \tag{4.9}$$

where $y_{int}(m)$ is the output of the interpolator either form linear interpolation $y_{linear}(m)$ or from sinc interpolation $y_{sinc}(m)$.

The normalized CFO ε is estimated using the phase of the correlation function and is given by

$$\hat{\varepsilon}_3 = -\frac{1}{2\pi} \angle \text{C3}. \tag{4.10}$$

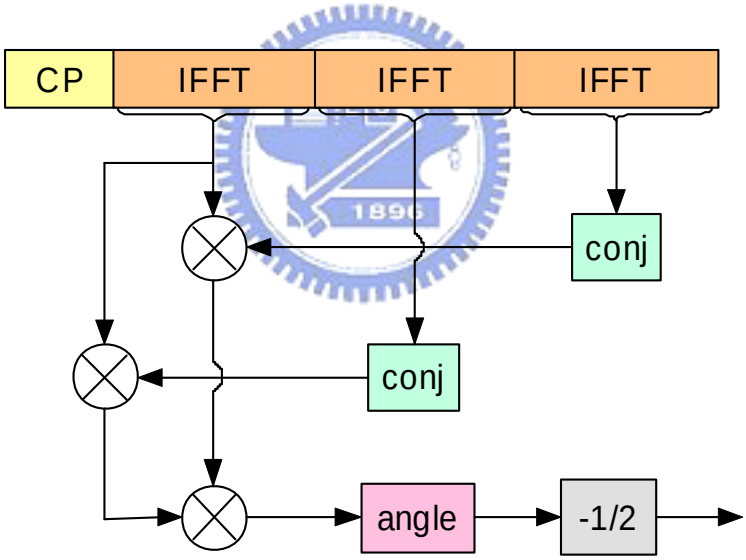

Figure 4.4: Block diagram of modified algorithm 3 via interpolations.

4.2.4 Modified Algorithm 4 via Interpolations

Finally, the modified algorithm 4 is an extension of modified algorithm 1 by extending the length of the correlation window from N samples to $2N$ samples. If we ignore

the noise effect, the sample-by-sample correlation function can be written as

$$\begin{aligned}
\text{C4} &= \sum_{m=0}^{2N-1} y_{int}(m) y_{int}(m+N)^* \\
&= \sum_{m=0}^{2N-1} x_{int}(m) e^{j2\pi m\varepsilon/3N} \cdot [x_{int}(m+N) e^{j2\pi(m+N)\varepsilon/3N}]^* \\
&= \sum_{m=0}^{2N-1} x_{int}(m) x_{int}(m+N)^* e^{j2\pi m\varepsilon/3N} e^{-j2\pi(m+N)\varepsilon/3N} \\
&= e^{-j2\pi N\varepsilon/3N} \sum_{m=0}^{2N-1} \|x_{int}(m)\|^2 \\
&= e^{-j2\pi\varepsilon/3} \sum_{m=0}^{2N-1} \|x_{int}(m)\|^2 \qquad (4.11)
\end{aligned}$$

where $y_{int}(m)$ is the output of the interpolator either form linear interpolation $y_{linear}(m)$ or from sinc interpolation $y_{sinc}(m)$.

The normalized CFO ε is estimated using the phase of the correlation function and is given by

$$\hat{\varepsilon}_4 = -\frac{3}{2\pi} \angle \text{C4}. \qquad (4.12)$$

4.3 Simulation Results and Discussions

Performance improvement due to linear or sinc interpolation can be obtained in the proposed correlation-based algorithms in both the AWGN channel and the multipath fading channel. We discuss each algorithm respectively and compare the performance improvement between the cases with and without interpolations (linear or sinc).

For AWGN channel, performance improvement of algorithm 1 is about 2 dB at low SNR if the interpolation is present. When SNR increases, the performance advantages of the proposed scheme will increase; see **Fig. 4.5**, **Fig. 4.13** and **Fig. 4.21**. Significant performance improvement can be obtained in the multipath fading channel by using the proposed interpolations; see **Fig. 4.6**, **Fig. 4.14** and **Fig. 4.22**. The performance improvement of algorithm 2 with interpolations in AWGN channel is about 5 dB at low

SNR. When SNR increases, the performance advantages of the proposed scheme will increase; see **Fig. 4.7**, **Fig. 4.15** and **Fig. 4.23**. When multipath exists, significant performance improvement is obtained under the interpolations; see **Fig. 4.8**, **Fig. 4.16** and **Fig. 4.24**. For the other two algorithms, we have similar simulation results.

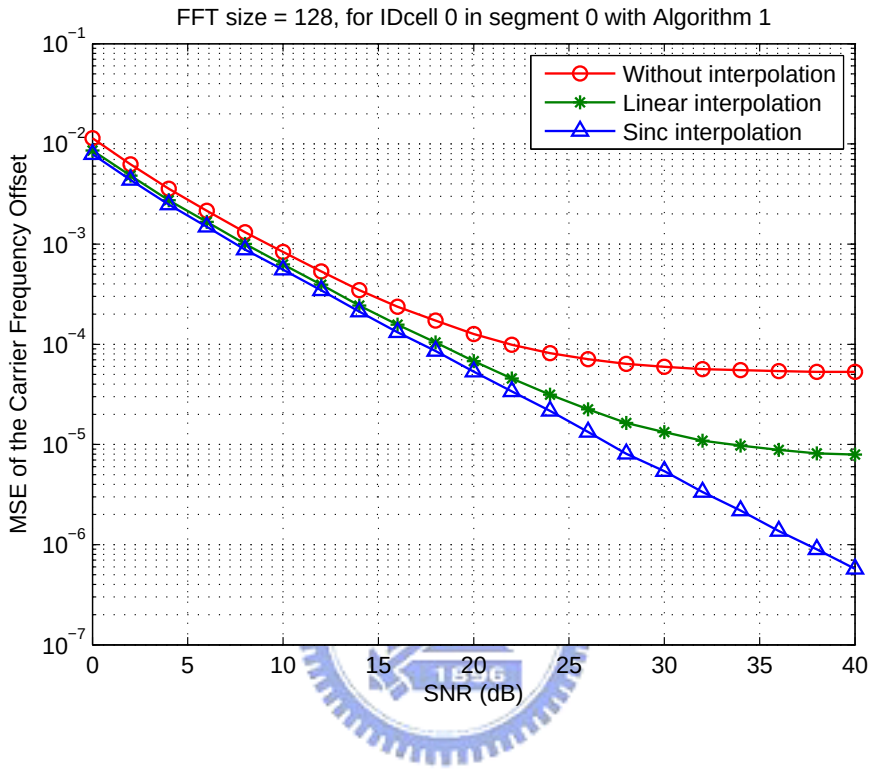

Figure 4.5: MSE of normalized CFO $\hat{\varepsilon}$ estimate as a function of the SNR in AWGN channel using IDcell 0 preamble in segment 0 via Algorithm 1.

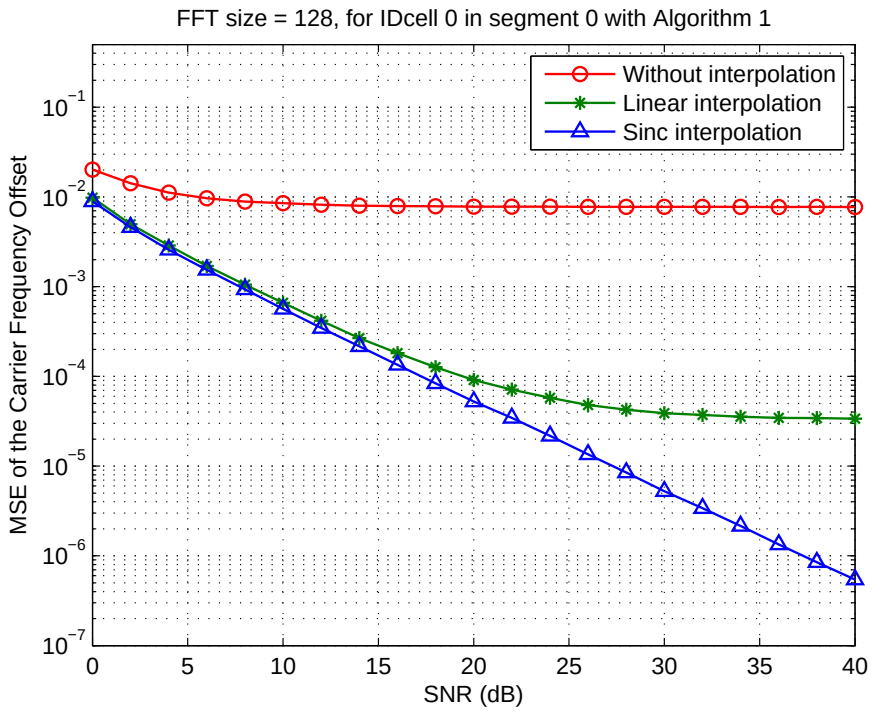

Figure 4.6: MSE of normalized CFO $\hat{\varepsilon}$ estimate as a function of the SNR in multipath fading channel using IDcell 0 preamble in segment 0 via Algorithm 1.

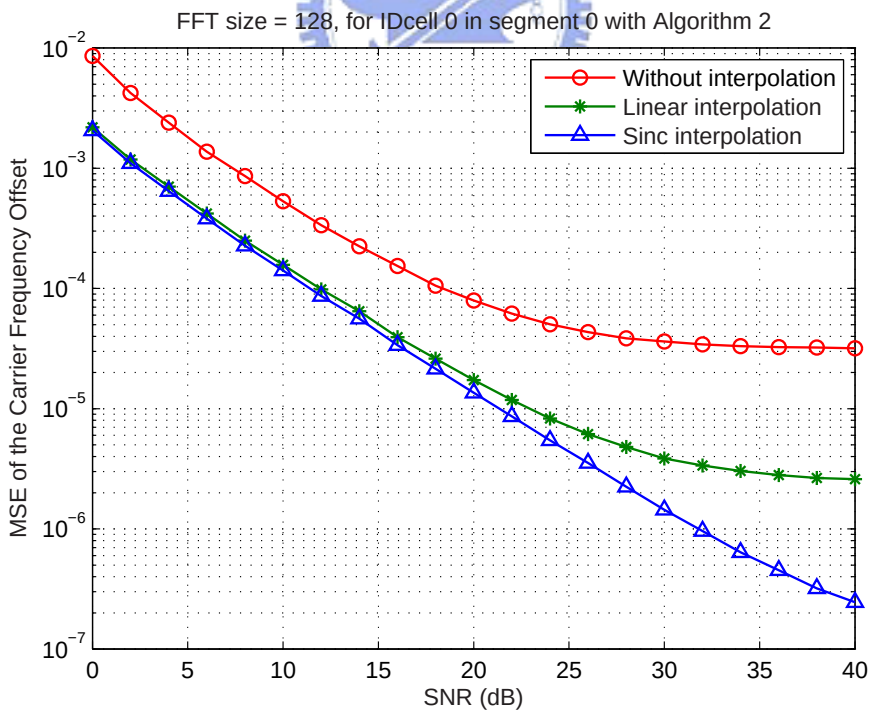

Figure 4.7: MSE of normalized CFO $\hat{\varepsilon}$ estimate as a function of the SNR in AWGN channel using IDcell 0 preamble in segment 0 via Algorithm 2.

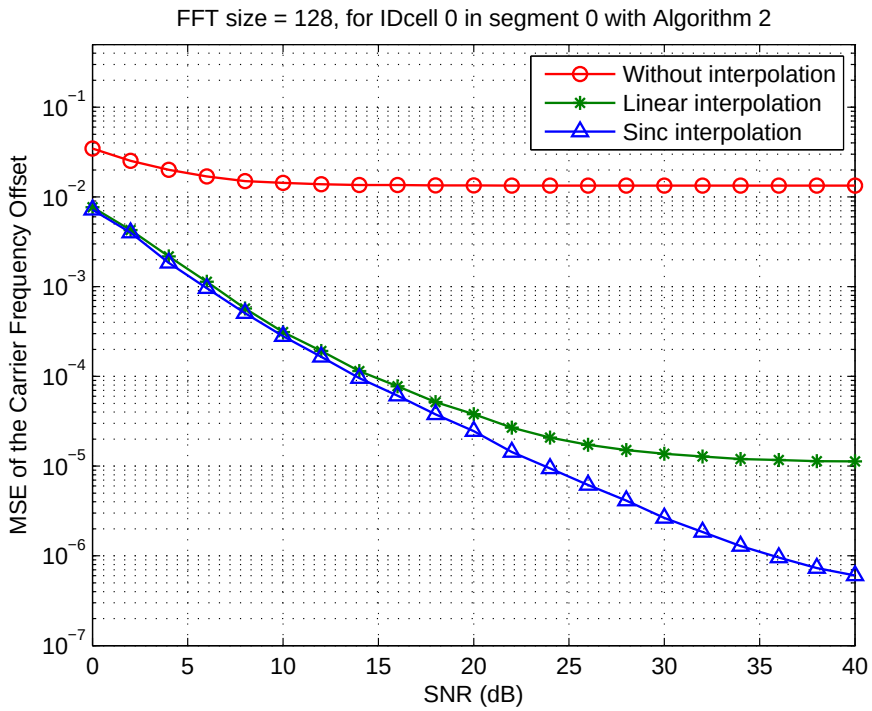

Figure 4.8: MSE of normalized CFO $\hat{\varepsilon}$ estimate as a function of the SNR in multipath fading channel using IDcell 0 preamble in segment 0 via Algorithm 2.

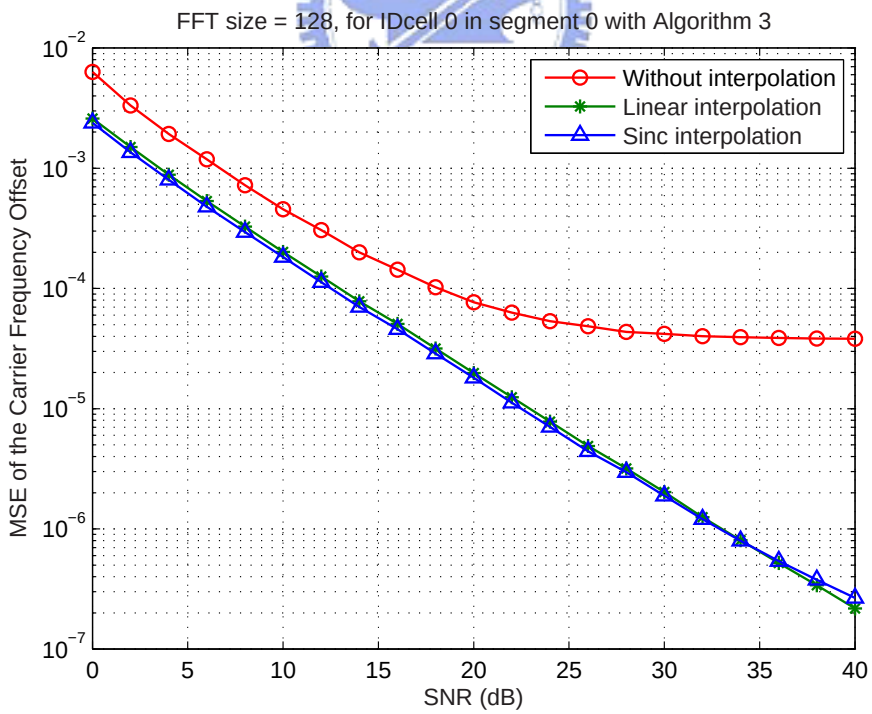

Figure 4.9: MSE of normalized CFO $\hat{\varepsilon}$ estimate as a function of the SNR in AWGN channel using IDcell 0 preamble in segment 0 via Algorithm 3.

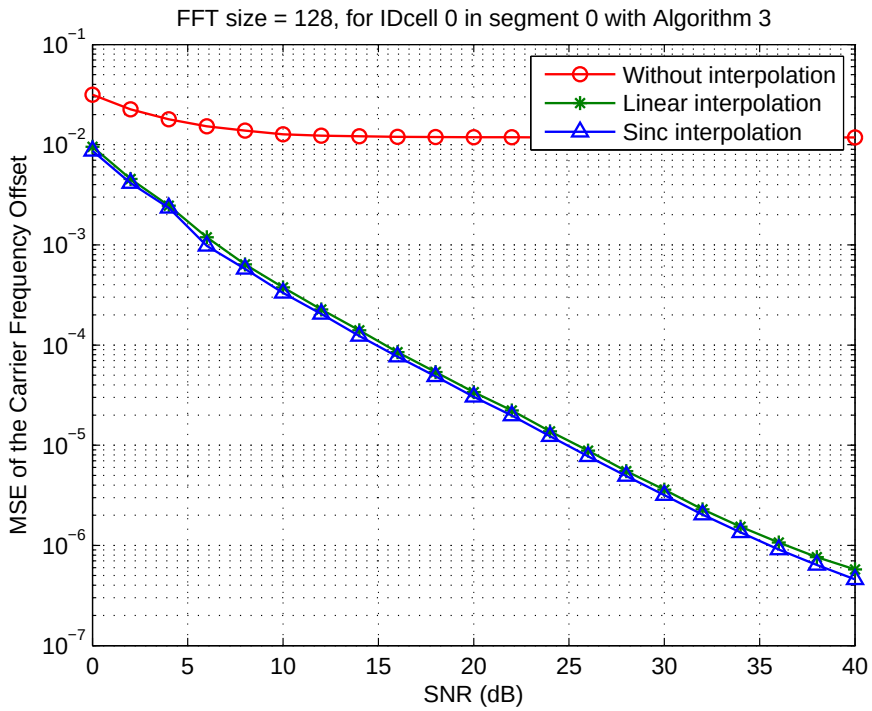

Figure 4.10: MSE of normalized CFO $\hat{\varepsilon}$ estimate as a function of the SNR in multipath fading channel using IDcell 0 preamble in segment 0 via Algorithm 3.

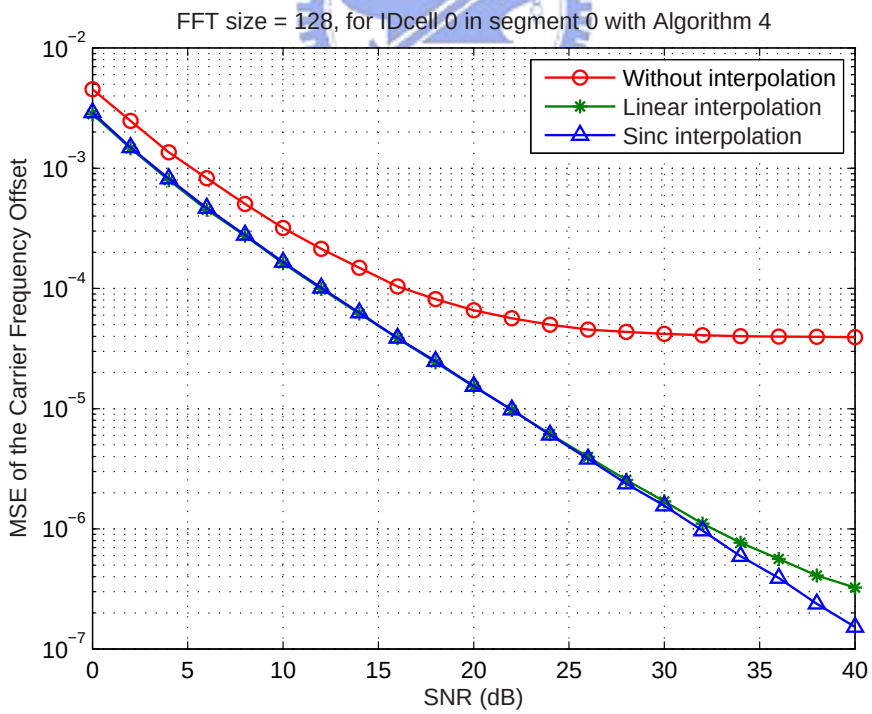

Figure 4.11: MSE of normalized CFO $\hat{\varepsilon}$ estimate as a function of the SNR in AWGN channel using IDcell 0 preamble in segment 0 via Algorithm 4.

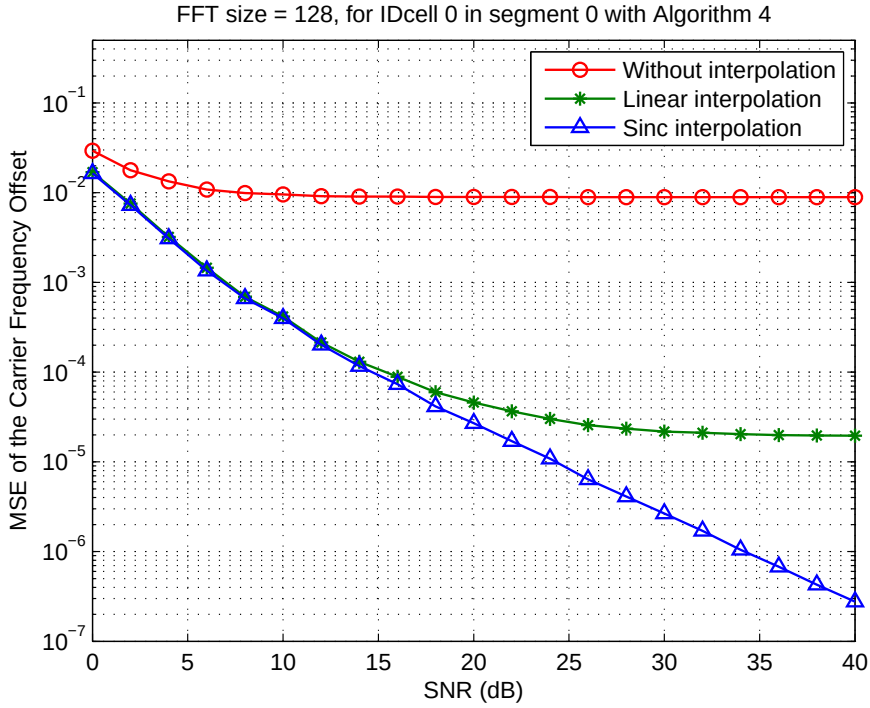

Figure 4.12: MSE of normalized CFO $\hat{\varepsilon}$ estimate as a function of the SNR in multipath fading channel using IDcell 0 preamble in segment 0 via Algorithm 4.

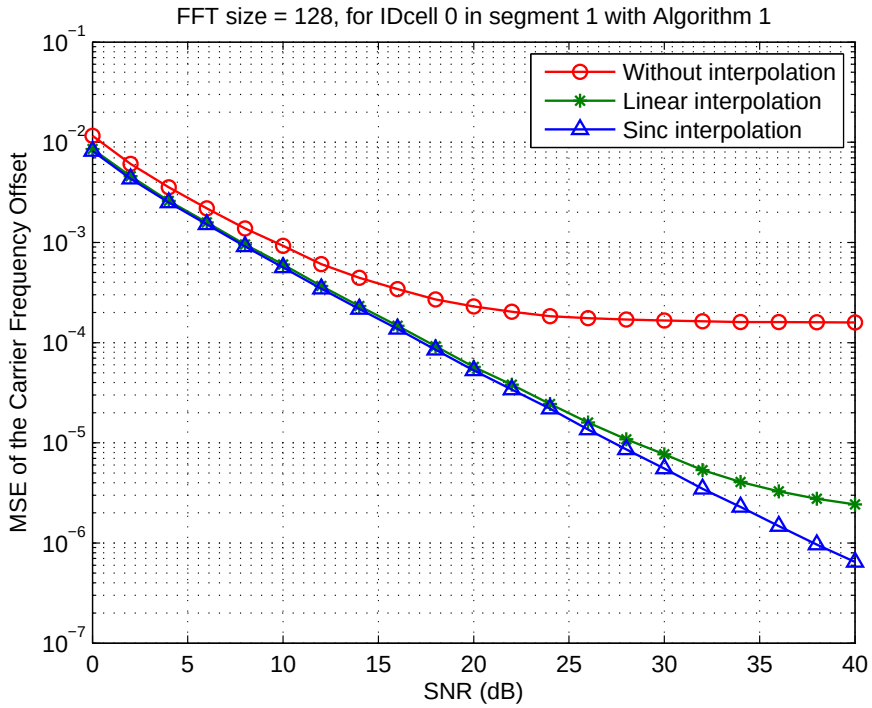

Figure 4.13: MSE of normalized CFO $\hat{\varepsilon}$ estimate as a function of the SNR in AWGN channel using IDcell 0 preamble in segment 1 via Algorithm 1.

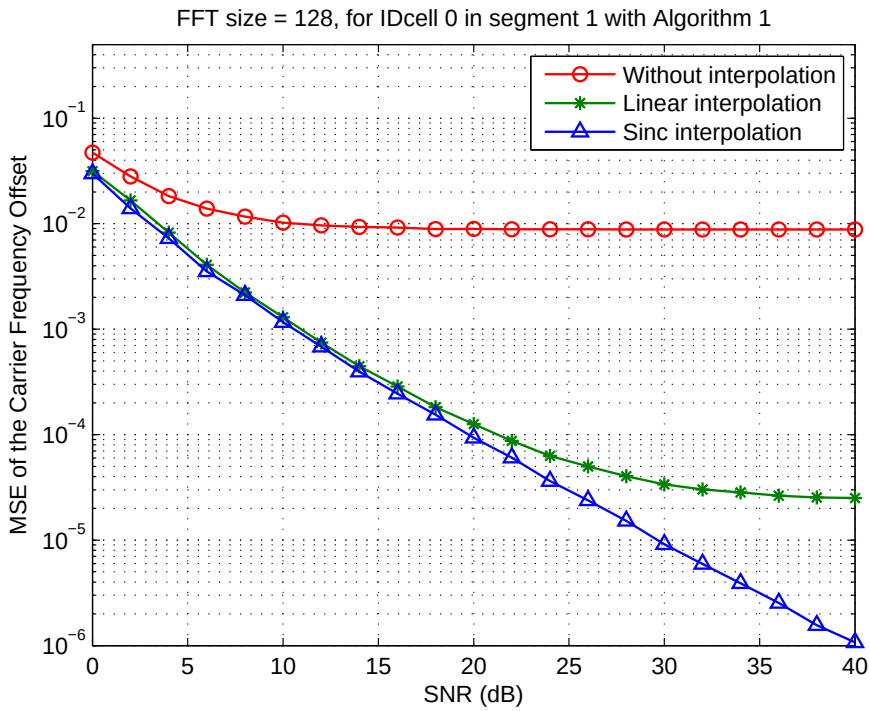

Figure 4.14: MSE of normalized CFO $\hat{\varepsilon}$ estimate as a function of the SNR in multipath fading channel using IDcell 0 preamble in segment 1 via Algorithm 1.

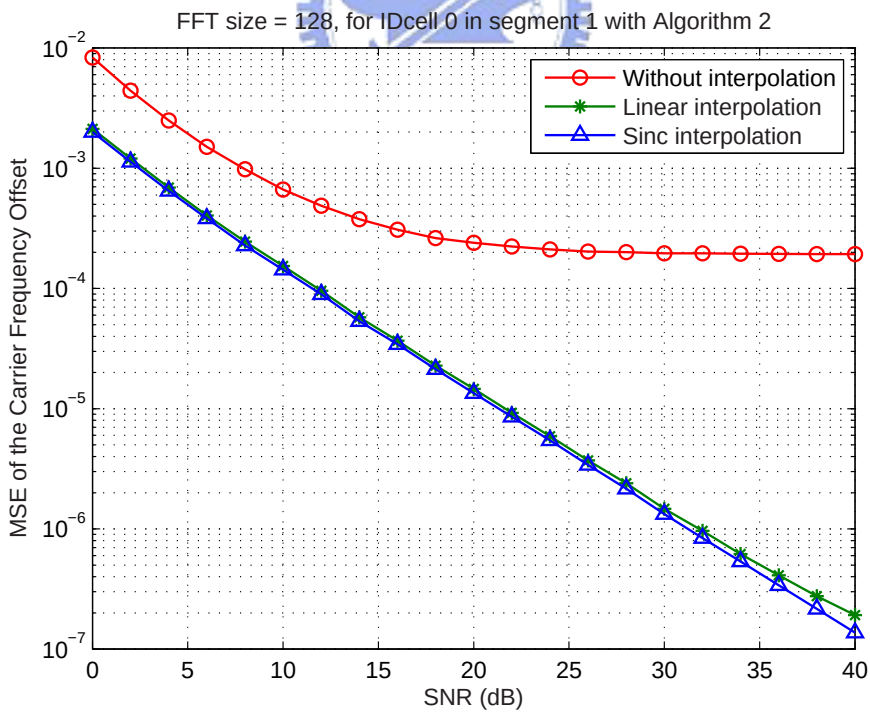

Figure 4.15: MSE of normalized CFO $\hat{\varepsilon}$ estimate as a function of the SNR in AWGN channel using IDcell 0 preamble in segment 1 via Algorithm 2.

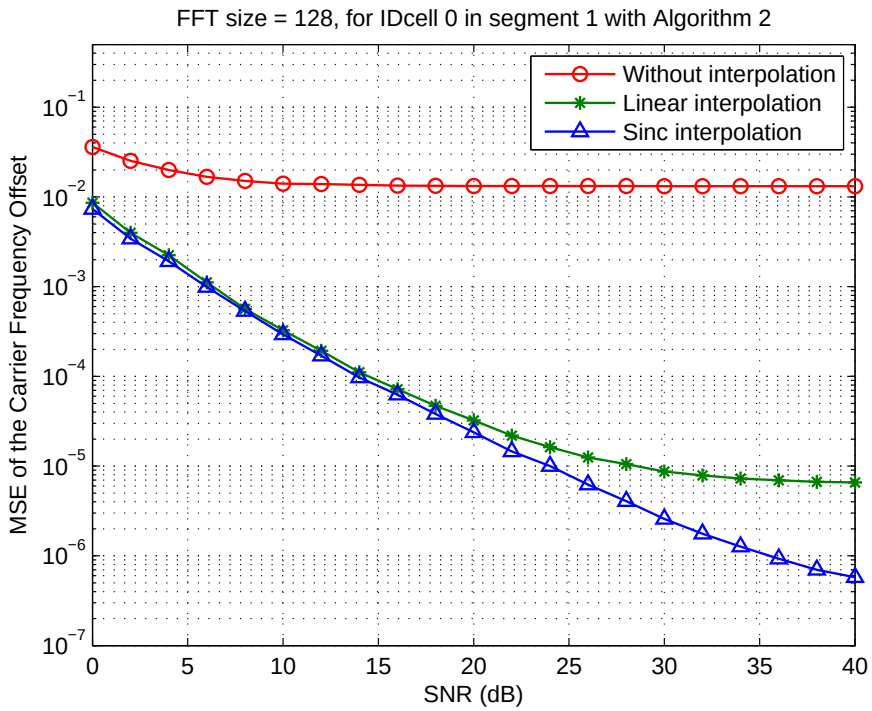

Figure 4.16: MSE of normalized CFO $\hat{\varepsilon}$ estimate as a function of the SNR in multipath fading channel using IDcell 0 preamble in segment 1 via Algorithm 2.

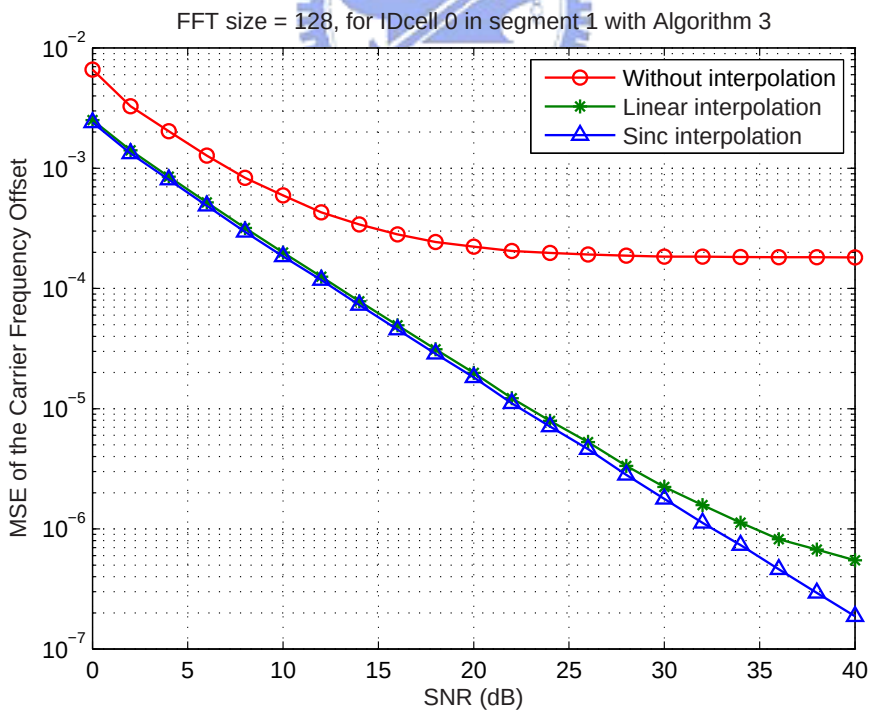

Figure 4.17: MSE of normalized CFO $\hat{\varepsilon}$ estimate as a function of the SNR in AWGN channel using IDcell 0 preamble in segment 1 via Algorithm 3.

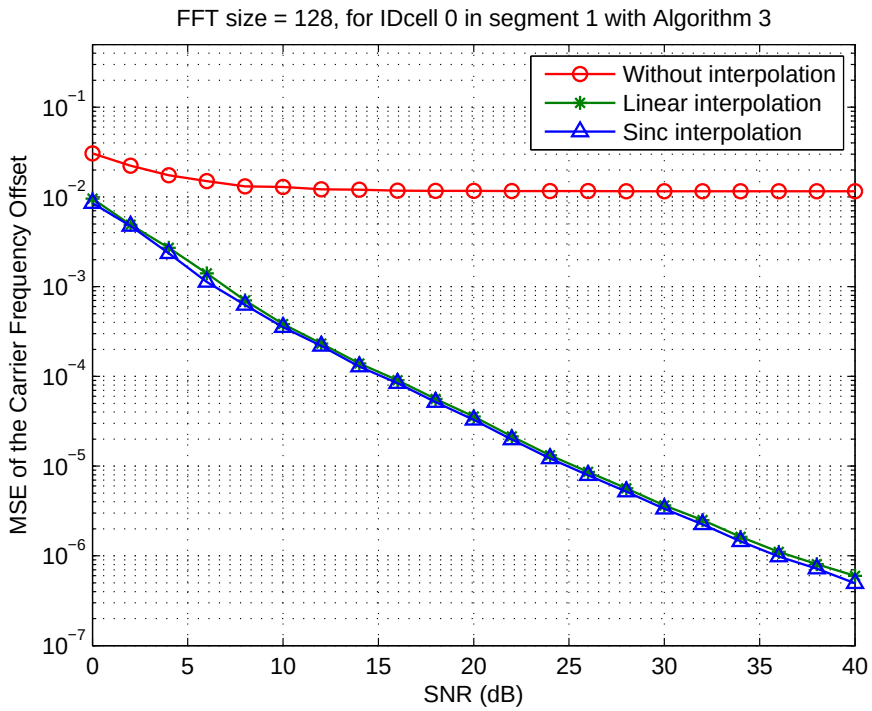

Figure 4.18: MSE of normalized CFO $\hat{\varepsilon}$ estimate as a function of the SNR in multipath fading channel using IDcell 0 preamble in segment 1 via Algorithm 3.

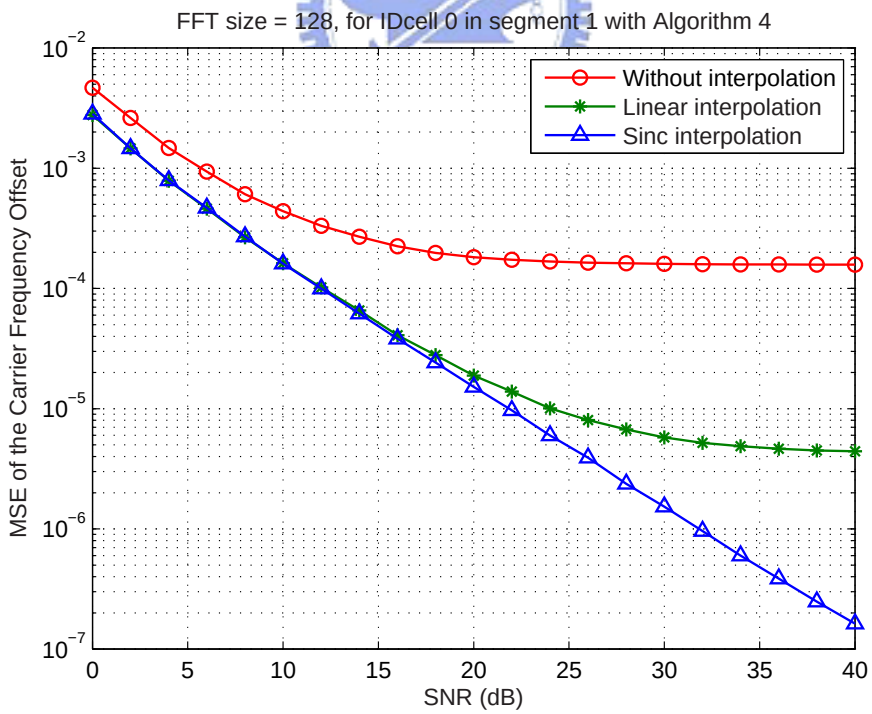

Figure 4.19: MSE of normalized CFO $\hat{\varepsilon}$ estimate as a function of the SNR in AWGN channel using IDcell 0 preamble in segment 1 via Algorithm 4.

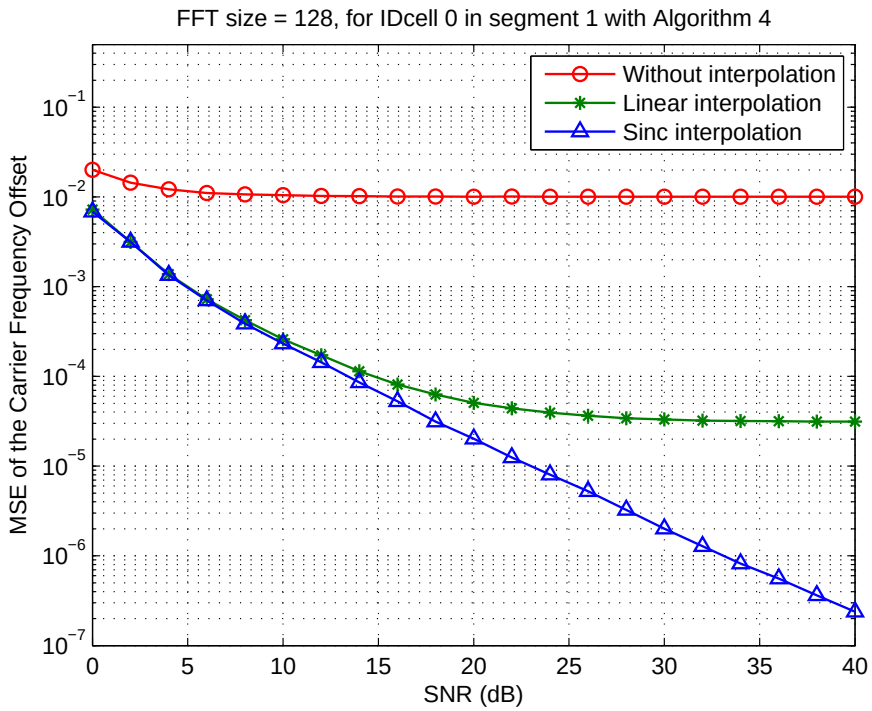

Figure 4.20: MSE of normalized CFO $\hat{\varepsilon}$ estimate as a function of the SNR in multipath fading channel using IDcell 0 preamble in segment 1 via Algorithm 4.

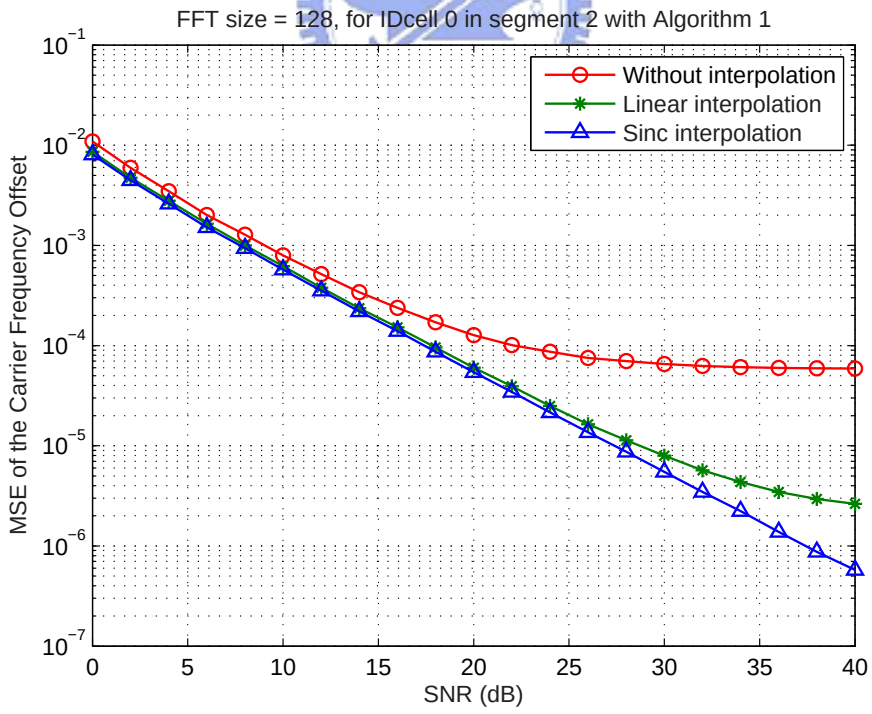

Figure 4.21: MSE of normalized CFO $\hat{\varepsilon}$ estimate as a function of the SNR in AWGN channel using IDcell 0 preamble in segment 2 via Algorithm 1.

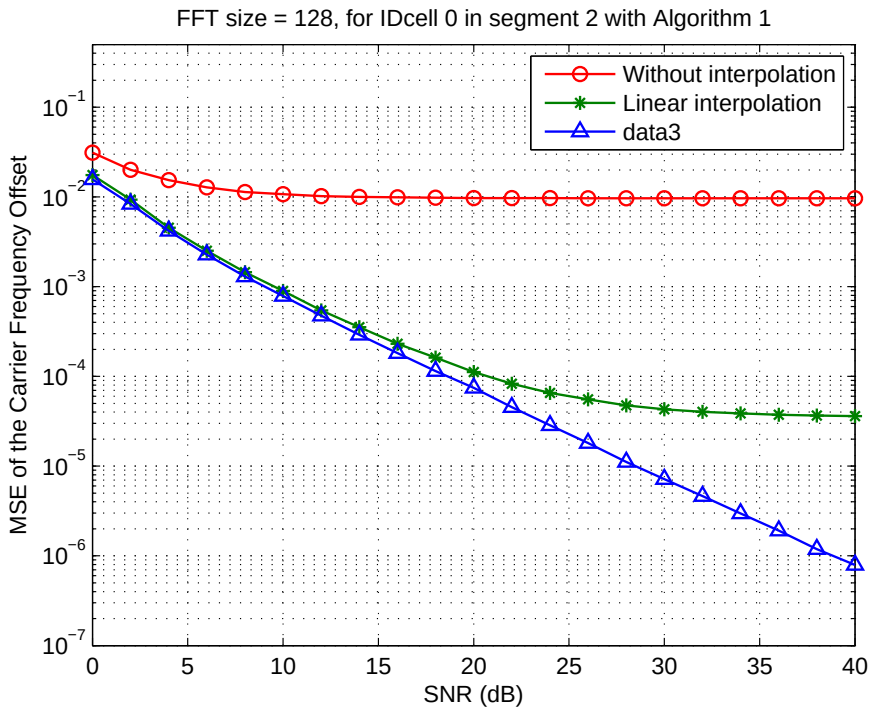

Figure 4.22: MSE of normalized CFO $\hat{\varepsilon}$ estimate as a function of the SNR in multipath fading channel using IDcell 0 preamble in segment 2 via Algorithm 1.

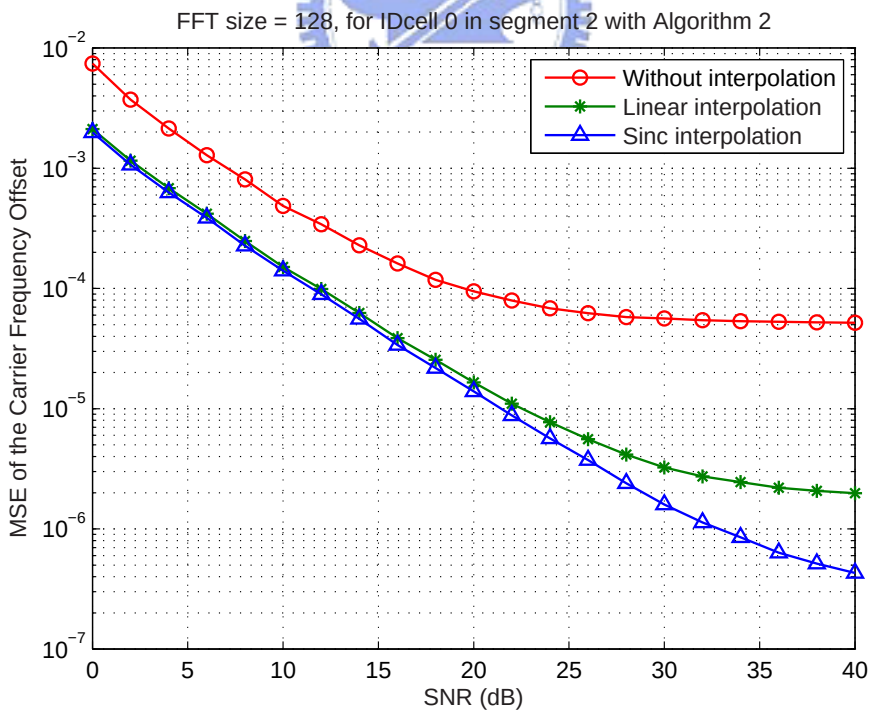

Figure 4.23: MSE of normalized CFO $\hat{\varepsilon}$ estimate as a function of the SNR in AWGN channel using IDcell 0 preamble in segment 2 via Algorithm 2.

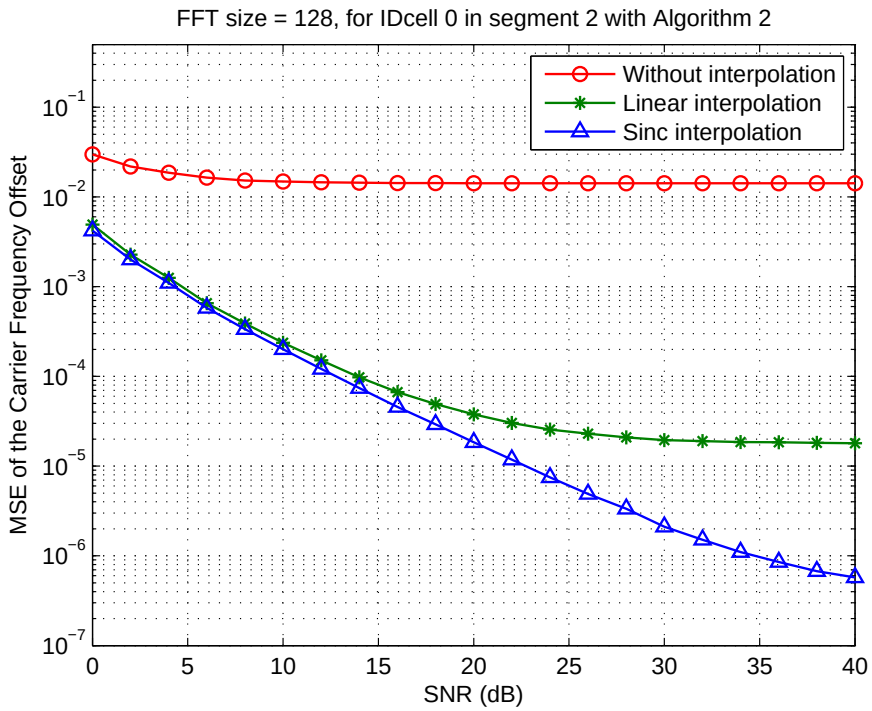

Figure 4.24: MSE of normalized CFO $\hat{\varepsilon}$ estimate as a function of the SNR in multipath fading channel using IDcell 0 preamble in segment 2 via Algorithm 2.

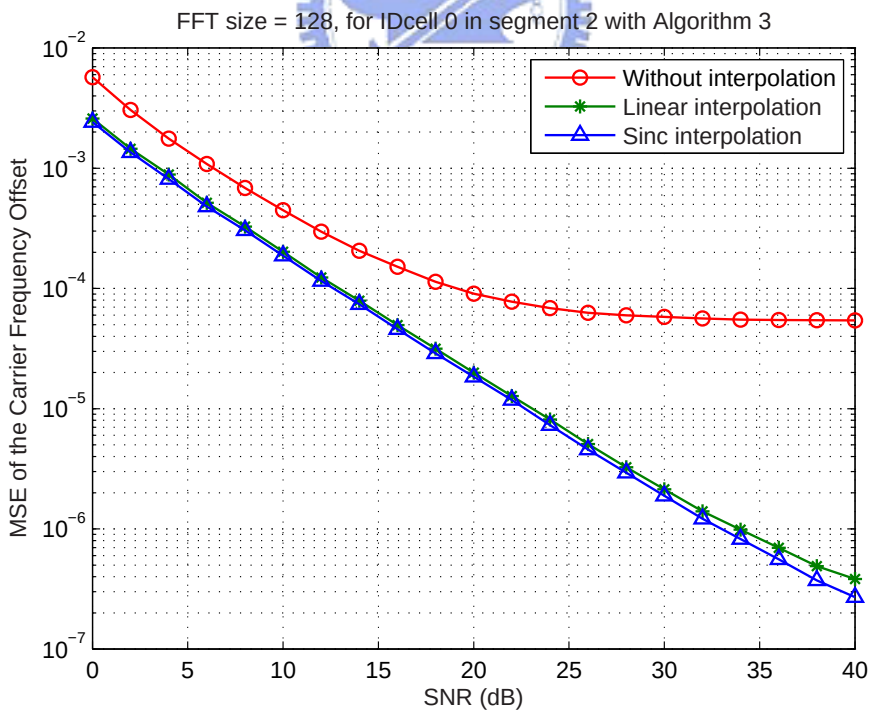

Figure 4.25: MSE of normalized CFO $\hat{\varepsilon}$ estimate as a function of the SNR in AWGN channel using IDcell 0 preamble in segment 2 via Algorithm 3.

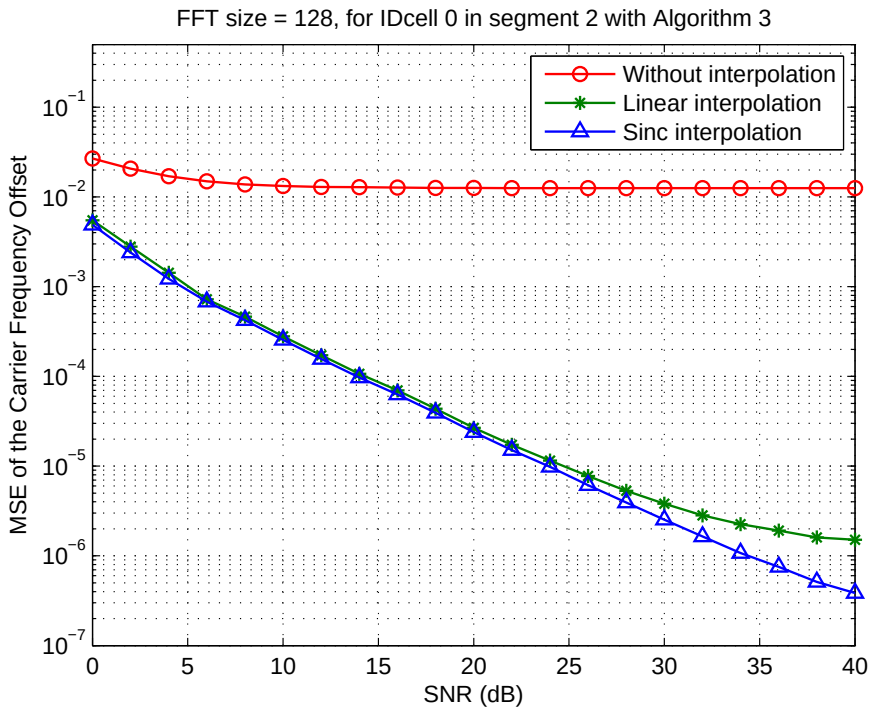

Figure 4.26: MSE of normalized CFO $\hat{\varepsilon}$ estimate as a function of the SNR in multipath fading channel using IDcell 0 preamble in segment 2 via Algorithm 3.

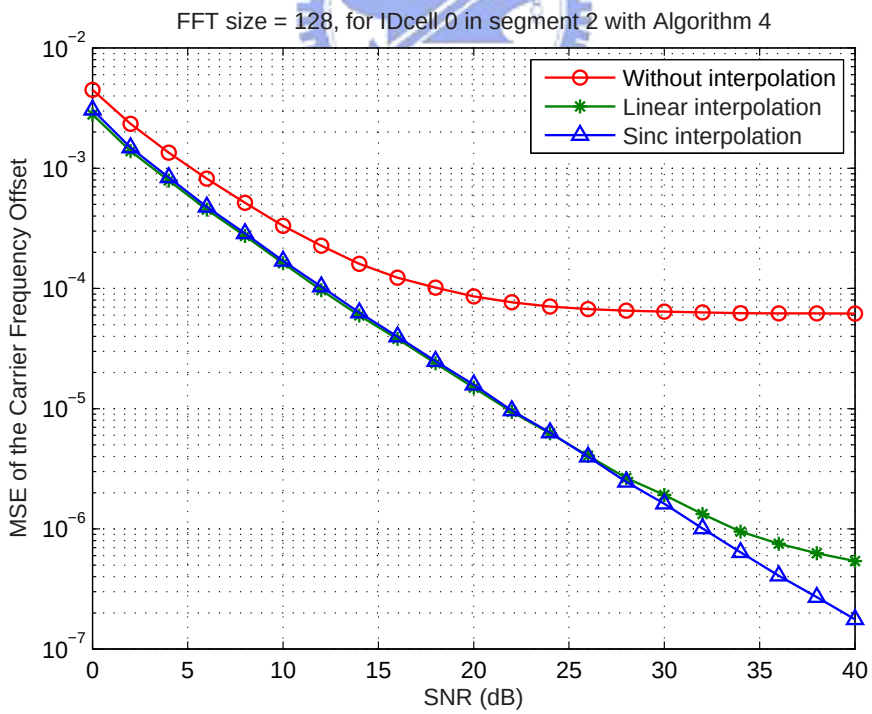

Figure 4.27: MSE of normalized CFO $\hat{\varepsilon}$ estimate as a function of the SNR in AWGN channel using IDcell 0 preamble in segment 2 via Algorithm 4.

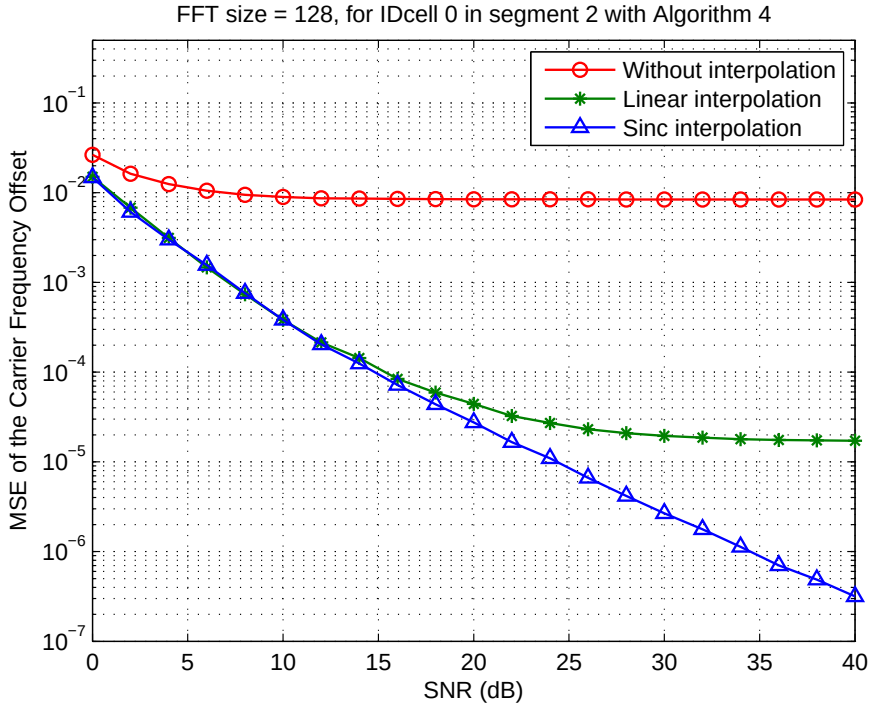

Figure 4.28: MSE of normalized CFO $\hat{\varepsilon}$ estimate as a function of the SNR in multipath fading channel using IDcell 0 preamble in segment 2 via Algorithm 4.

Chapter 5

Downlink Pilot-Assisted Maximum-Likelihood Frequency-Offset Estimation

This chapter further explore maximum-likelihood (ML) CFO estimates of TDD-OFDMA WiMAX downlink system that uses three of identical fractional-period OFDM blocks obtained from interpolations. An efficient algorithm is provided to solve the associated highly nonlinear ML equation. We convert the problem of obtaining the ML solution from searching exhaustively over the entire uncertainty range to that of solving a spectrum polynomial of degree 4, thereby greatly reducing the computational load. By properly truncating the polynomial, we obtain a closed-form expression for the corresponding zeros so that the root-searching procedure is greatly simplified.

5.1 Maximum-Likelihood Estimation of Carrier Frequency Offset

Let $s(p,q)$ be the qth sample of the pth(time-domain) short pilot symbol and assume that the preamble part of a transmitted package consists of three identical short pilot symbols obtained from interpolations, as shown in **Fig. 2.6**. We thus have the relation $s(p,q) = r((p-1)N+q)$ for $p = 1,2,3$ and $q = 1,...,N$ where $r(\cdot)$ is the interpolated preamble samples. Consider a frequency-selective channel with a maximum delay spread

shorter than a CP duration. After discarding the CP, the remaining received three pilot symbols $y(p,q)$ can be represented as

$$y(p,q) = e^{\frac{j2\pi\varepsilon((p-1)N+q)}{3N}} x(p,q) + v(p,q) \tag{5.1}$$

for $p = 1, 2, 3$, and $q = 1, ..., N$, where $x(p,q) = x_{int}((p-1)N+q)$ is the interpolated channel output corresponding to the transmitted pilot symbol $s(p,q)$, $y(p,q) = y_{int}((p-1)N+q)$ and $v(p,q) = w((p-1)N+q)$.

Define the two vectors

$$\mathbf{Y}(q) = \left[\begin{array}{ccc} y(1,q) & y(2,q) & y(3,q) \end{array} \right]^T \tag{5.2}$$

and

$$\mathbf{A}(\varepsilon) = \left[\begin{array}{ccc} 1 & e^{\frac{j2\pi\varepsilon N}{3N}} & e^{\frac{j2\pi\varepsilon 2N}{3N}} \end{array} \right]^T \tag{5.3}$$

where $(\cdot)^T$ denotes the matrix transpose. Then, we have

$$\begin{aligned} \mathbf{Y}(q) &= \mathbf{A}(\varepsilon) e^{\frac{j2\pi\varepsilon q}{3N}} x(1,q) + \mathbf{V}(q) \\ &= \mathbf{A}(\varepsilon) x(q) + \mathbf{V}(q), \qquad q = 1, ..., N \end{aligned} \tag{5.4}$$

where $x(q) = e^{j2\pi\varepsilon q/3N} x(1,q)$, and $\mathbf{V}(q) = [v(1,q)\ v(2,q)\ v(3,q)]^T$. The received samples can thus be expressed compactly as

$$\underline{\mathbf{Y}} = \mathbf{A}(\varepsilon)\mathbf{X} + \underline{\mathbf{V}} \tag{5.5}$$

where $\underline{\mathbf{Y}} = [\mathbf{Y}(1), ..., \mathbf{Y}(N)]$, $\mathbf{X} = [x(1), ..., x(N)]$, and $\underline{\mathbf{V}} = [\mathbf{V}(1), ..., \mathbf{V}(N)]$. Hence, given the received sample vectors $\underline{\mathbf{Y}}$, we have to estimate ε through the deterministic vector $\mathbf{A}(\varepsilon)$.

Since the noise is temporally white Gaussian, $\mathbf{Y}(q)$ is a multivariate Gaussian distributed random vector with covariance matrix $\sigma_v^2\mathbf{I}$, where $\mathbf{I}$ is the identity matrix. The joint ML estimates of $\mathbf{A}$ and $\mathbf{X}$, treating $\mathbf{X}$ as a deterministic unknown vector, are

obtained by minimizing the joint probability density function

$$\begin{aligned} f(\underline{\mathbf{Y}}|\mathbf{A},\mathbf{X}) &= \prod_{q=1}^{N} f(\mathbf{Y}(q)|\mathbf{A},x(q)) \\ &\propto \exp\left[-\frac{1\sum_{q=1}^{N}\|\mathbf{Y}(q)-\mathbf{A}x(q)\|^2}{\sigma_v^2}\right] \end{aligned} \tag{5.6}$$

The corresponding log-likelihood function, after dropping constant and unrelated terms, is given by

$$\Lambda(\mathbf{A},x(q)) = \sum_{q=1}^{N}\|\mathbf{Y}(q)-\mathbf{A}x(q)\|^2 \tag{5.7}$$

For a given $\mathbf{A}$, setting $\nabla_{x(q)}\|\mathbf{Y}(q)-\mathbf{A}x(q)\|^2 = 0$, where $\nabla_{x(q)}$ denotes complex gradient operation with respect to $x(q)$, we obtain the conditional ML estimate $\hat{x}(q) = x_{LS}(q) = \mathbf{A}^{+}\mathbf{Y}(q)$, where $\mathbf{A}^{+} = \mathbf{A}^{H}/K$ and ^{H} denotes the Hermitian operation. Substituting the least-square solution $x_{LS}(q)$ into (5.7), we obtain

$$\begin{aligned} \Lambda(\mathbf{A}) &= \sum_{q=1}^{N}\|\mathbf{Y}(q)-\mathbf{A}\mathbf{A}^{+}\mathbf{Y}(q)\|^2 \\ &= \sum_{q=1}^{N}\|\mathbf{P}_A^{\perp}\mathbf{Y}(q)\|^2 \\ &= N\mathrm{tr}\left(\mathbf{P}_A^{\perp}\hat{\mathbf{R}}_{YY}\right) \end{aligned} \tag{5.8}$$

where $\mathrm{tr}(\cdot)$ denotes the trace of a matrix, $\hat{\mathbf{R}}_{YY} = (1/N)\sum_{q=1}^{N}\mathbf{Y}(q)\mathbf{Y}^{H}(q)$, and $\mathbf{P}_A^{\perp} = \mathbf{I}-\mathbf{A}\mathbf{A}^{\perp}$. Note that the (i,j)th entry of the matrix $\hat{\mathbf{R}}_{YY}$, $\hat{R}_{YY}(i,j)$, is the correlation value of ith and jth received symbols, i.e., $\hat{R}_{YY}(i,j) = N^{-1}\sum_{q=1}^{N}y(i,q)y^{*}(j,q)$. As $\hat{\mathbf{R}}_{YY}$ is the (time-averaged) autocorrelation matrix of the received sample vectors $\mathbf{Y}(q)$, it is a Hermitian matrix such that $\hat{R}_{YY}(i,j) = \hat{R}_{YY}^{*}(j,i)$, where $(*)$ denotes the complex conjugate. The CFO estimate is then given by

$$\begin{aligned} \hat{\varepsilon} &= \arg\left\{\min_{\varepsilon}\mathrm{tr}\left(\mathbf{P}_A^{\perp}\hat{\mathbf{R}}_{YY}\right)\right\} \\ &= \arg\left\{\max_{\varepsilon}\mathrm{tr}\left(\mathbf{P}_A\hat{\mathbf{R}}_{YY}\right)\right\} \\ &= \arg\left\{\max_{\varepsilon}\mathbf{A}^{H}\hat{R}_{YY}\mathbf{A}\right\} \end{aligned} \tag{5.9}$$

Although (5.9) gives a compact representation of the ML CFO estimate, it requires an exhaustive search over the entire uncertainty range. The resulting complexity may make its implementation infeasible.

We observe, however, that $\mathbf{A}$ has a special structure that can be of use to reduce the complexity of searching the desired CFO solution of (5.9). Invoking an approach similar to that used by the MUSIC algorithm, we set $z = e^{j2\pi\varepsilon N/3N}$ and define the parameter vector

$$\mathbf{A}(z) = [1, z, z^2]^T \tag{5.10}$$

so that the log-likelihood $\Lambda = \mathbf{A}^H \hat{\mathbf{R}}_{YY} \mathbf{A}$ can be expressed as a polynomial of order 5 as follows:

$$\Lambda(z) = \mathbf{A}(z)^H \hat{\mathbf{R}}_{YY} \mathbf{A}(z) = \sum_{n=-2}^{2} s(n) z^n \tag{5.11}$$

where $s(n) = \sum_{i,j} \hat{R}_{YY}(i,j)$, for $n = j - i$, and $n = -2, ..., 2$. To highlight the usefulness of this important observation, we restate it in the form of the following proposition.

Proposition 1: The log-likelihood function for a candidate CFO ε is given by

$$\Lambda(\varepsilon) = \sum_{n=-2}^{2} s(n) e^{\frac{j2\pi n\varepsilon N}{3N}} \tag{5.12}$$

Some remarks about this proposition are in order.

Remarks:

R1. $s(n)$ is the summation of diagonal entries of $\hat{\mathbf{R}}_{YY}$ and is also equivalent to the aperiodic autocorrelation value of the waveform $\{y(i,j), 1 \le i \le 3, 1 \le j \le N\}$, i.e., $s(n) = \sum_{m=1}^{3-n} \sum_{j=1}^{N} y^*(m+n, j) y(m, j)$.

R2. It can be shown that, in the absence of noise

$$s(n) = \hat{\sigma}_x^2 (K - |n|) e^{-jn\theta_o} = \Delta(n) \tag{5.13}$$

where $\theta_o = 2\pi\varepsilon N/3N$, and $\hat{\sigma}_x^2 = (1/N) \sum_{n=1}^{N} |x(n)|^2$. When noise is present, the mean value of $s(n)$ is the same as its noiseless value except for $n = 0$; more

specifically, $E[s(n)] = \Delta(n) + K\sigma_w^2\delta(n)$, where $\delta(\cdot)$ is the Kronecker delta function. Evaluating (5.11) at the unit circle $z = e^{j2\pi\varepsilon N/3N} = e^{j\theta}$, we obtain the DTFT of the sequence $s(n)$, which has an envelope similar to $\text{sinc}^2(\varepsilon)$ whose maximum value is at the correct "modified" frequency $\varepsilon' = \varepsilon(N/3N)$.

R3. Due to the Hermitian nature of $\hat{\mathbf{R}}_{YY}$, $s(n)$ is a conjugate symmetric sequence of length 5. The symmetric property of $s(n)$ guarantees that its Fourier transform $\Lambda(e^{j2\pi\varepsilon})$ is real and nonnegative. This also follows from the semi-positive definiteness of the quadratic form $\mathbf{A}^H\hat{\mathbf{R}}_{YY}\mathbf{A}$. Because $s(n)$ and the log-likelihood function constitute a Fourier transform pair, we will henceforth refer to $\Lambda(e^{j2\pi\varepsilon})$ as the log-likelihood spectrum or spectrum, for short, and the polynomial defined by (5.11) the spectrum polynomial.

R4. $\{s(n), n = 0, 1, 2\} = C$ constitutes a set of sufficient statistic for estimating ε. Almost all previous correlation-based algorithms use only a subset of C. It is expected that an algorithm that uses the sufficient statistic would outperform those that use only a part of the sufficient statistic.

R5. Computing the desired CFO estimate through (5.11) is equivalent to searching for the peak of the candidate spectrum $\Lambda(e^{j2\pi\varepsilon})$. Hence, the spectrum can be computed using a DFT, but the resolution of the CFO estimate $\hat{\varepsilon}$ depends on the size of the DFT. Padding more zeros in the sequence $s(n)$ results in higher resolution at the expense of inducing higher computation complexity.

As the spectrum is a real smooth function of θ, taking a derivative of $\Lambda(e^{j\theta})$ with respect to θ and setting $\partial\Lambda(e^{j\theta})/\partial\theta = \dot{\Lambda}(\theta) = 0$, we obtain

$$F(z) = F^*(z) \tag{5.14}$$

where $F(z) = \sum_{n=1}^{2} ns(n)z^n$ is a polynomial of order 2. As mentioned before, in a noiseless environment, $\Lambda(e^{j2\pi\varepsilon})$, the Fourier transform of $\{s(n)\}$, is a scaled version of

the function $sinc^2(\varepsilon)$, and all roots of $\dot{\Lambda}(z) = \dot{\Lambda}(\theta)|_{e^{j\theta}=z} = j(F(z) - F^*(z))$ are on the unit circle.

For simplicity, we shall use the first approach, i.e., the desired estimate is to be obtained by

$$\hat{\varepsilon} = \frac{3N}{j2\pi N}\ln\hat{z} \tag{5.15}$$

where

$$\hat{z} = \arg\left\{\max_{z_i\in\Omega}\Lambda(z)\right\}, \quad \Omega = \left\{z|\dot{\Lambda}(z) = 0, |z| = 1\right\} \tag{5.16}$$

Note that we have converted the exhaustive search problem of (5.9) to a root-finding problem, reducing the candidate solution number from infinity to at most 4.

We summarize the procedure leading to (5.16) as follows.

1) Collect three received symbols obtained from interpolations and construct the sample correlation matrix $\hat{\mathbf{R}}_{YY}$.

2) Calculate the coefficients of $F(z)$ based on $\hat{\mathbf{R}}_{YY}$.

3) Find the nonzero unit-magnitude roots of (5.14).

4) Obtain the CFO estimate from (5.15) and (5.16).

We notice that the solutions of (5.14) are the nonzero roots of the polynomial

$$G(z) = z^2(F(z) - F^*(z)) \tag{5.17}$$

On the other hand, (5.14) implies that the roots of $\dot{\Lambda}(z)$ satisfy the equation $\mathrm{Im}\{F(z)\} = 0$, where $\mathrm{Im}\{F(z)\}$ is the imaginary part of $F(z)$. This observation indicates that the nonzero roots of $F_1(z) = z^{-1}F(z) = 0$ (the root $z = 0$ of $F(z)$ is undesired) are a subset of the roots of $\mathrm{Im}\{F(z)\} = 0$. When $F(z)$ is an arbitrary polynomial, its roots are not necessarily a subset of those of the corresponding $G(z)$ defined by (5.17).

Proposition 2: In the absence of noise, the polynomial defined by (5.17), $G(z)$, can be decomposed into

$$G(z) = F_1(z)Q(z) \tag{5.18}$$

where the desired CFO estimate is one of the roots of $Q(z)$ defined by

$$Q(z) = z^3 - \frac{s(-1)}{2 \times s(2)} = z^3 - d \tag{5.19}$$

where $d = s(-1)/(2 \times s(2))$.

When noise is present, the above equality becomes an approximation only. Nevertheless, the desired CFO estimate can still be derived immediately from taking the 3th root of d. The global maximum that collocated with a root of $Q(z)$ corresponds to the desired CFO estimate while the remaining roots of $Q(z)$ locate at a local minimum (null) of the spectrum. On the other hand, the roots of $F_1(z)$ are at the local sidelobe peaks of the spectrum. It is clear that the union of the roots of $Q(z)$ and $F_1(z)$ is the set of the roots of $G(z)$. Hence, the complexity of extracting the roots is significantly reduced, for we only have to solve the equation $Q(z) = 0$, which happens to have a closed-form expression for its roots. The above discussion suggests the following simplified CFO estimate algorithm.

1) Collect three received symbols obtained from interpolations and construct the sample correlation matrix $\hat{\mathbf{R}}_{YY}$.

2) Compute the coefficients d based on two correlation values $s(-1)$ and $s(2)$.

3) Solve $Q(z) = 0$ for the three unit-magnitude roots of d, $\{z_i\}$.

4) Find the estimate from (5.15) and (5.16).

5.2 Simulation Results and Discussions

Numerical examples are provided in this section to examine the behavior of the proposed CFO estimation technique. We utilize three short training symbols which are

the same as those used in the IEEE 802.16e downlink preamble. CFO is normalized by subcarrier spacing and the mean values and mean-squared errors (MSE) of various estimates are computed by 10^4 independent trials.

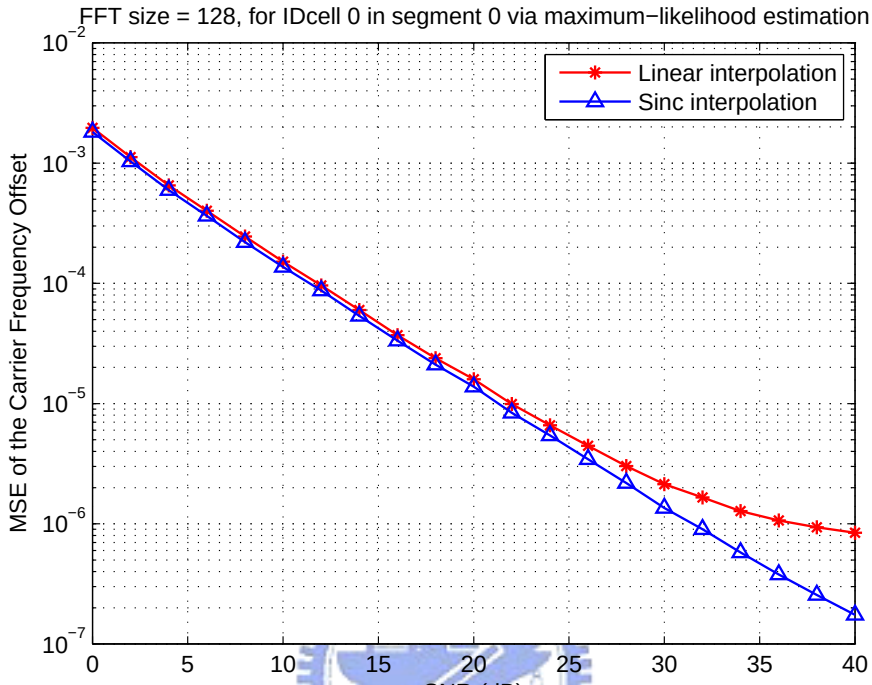

Figure 5.1: MSE of normalized CFO $\hat{\varepsilon}$ estimate as a function of the SNR in AWGN channel using IDcell 0 preamble in segment 0 via maximum-likelihood estimation.

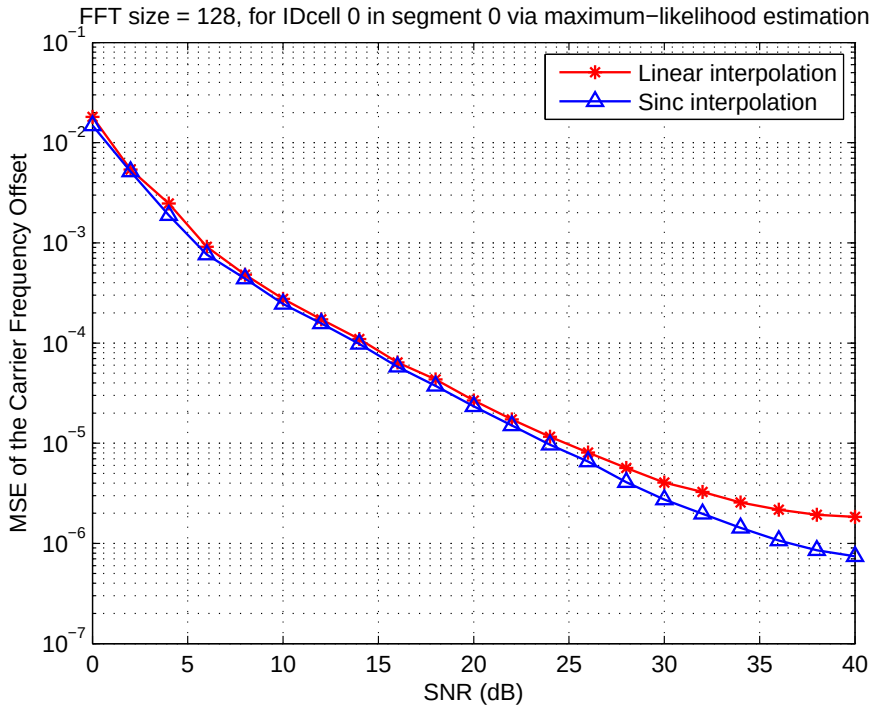

Figure 5.2: MSE of normalized CFO $\hat{\varepsilon}$ estimate as a function of the SNR in multipath fading channel using IDcell 0 preamble in segment 0 via maximum-likelihood estimation.

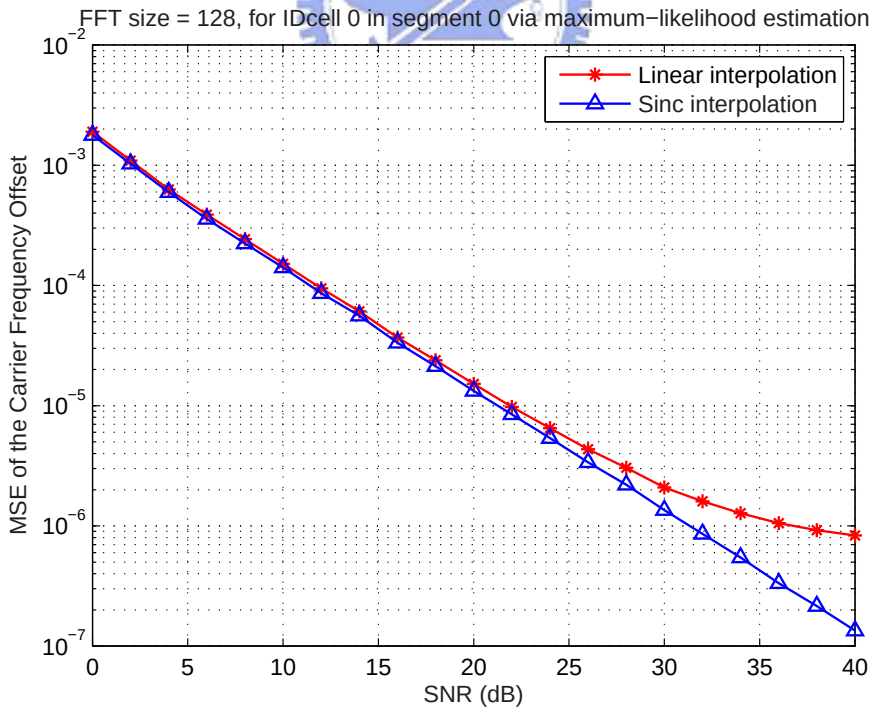

Figure 5.3: MSE of normalized CFO $\hat{\varepsilon}$ estimate as a function of the SNR in AWGN channel using IDcell 0 preamble in segment 1 via maximum-likelihood estimation.

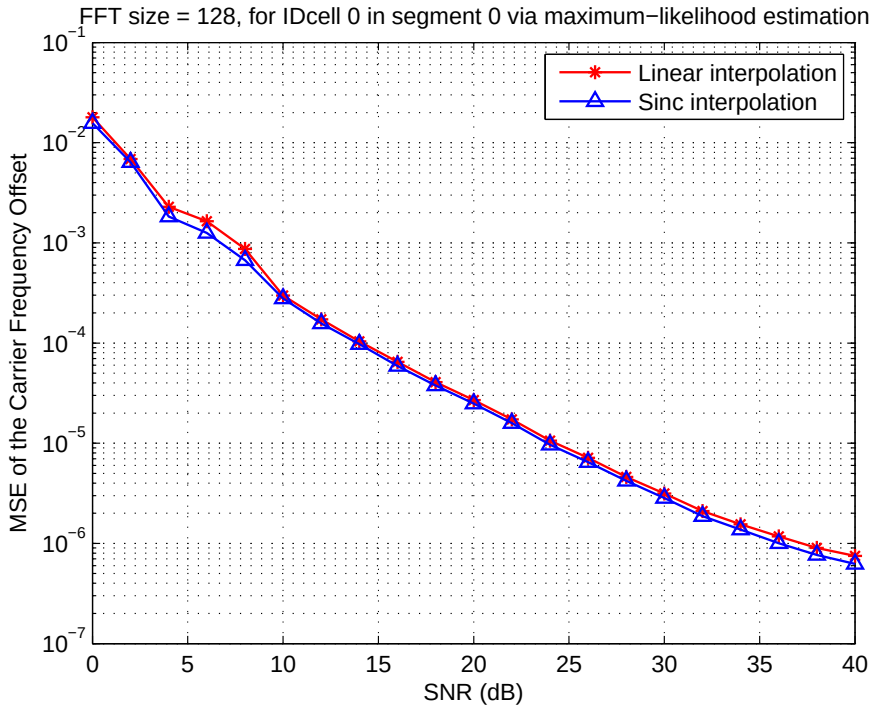

Figure 5.4: MSE of normalized CFO $\hat{\varepsilon}$ estimate as a function of the SNR in multipath fading channel using IDcell 0 preamble in segment 1 via maximum-likelihood estimation.

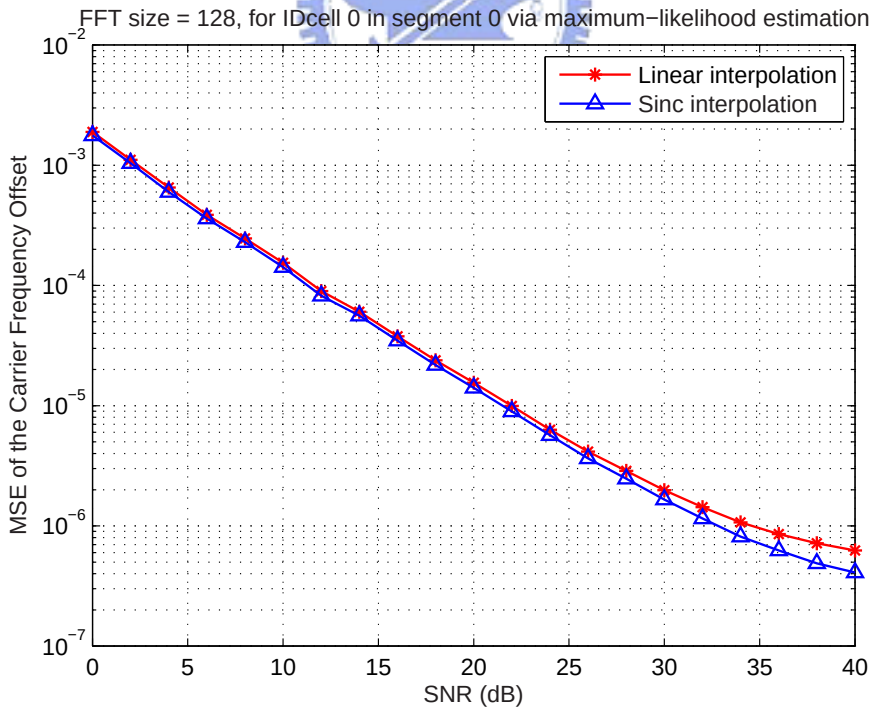

Figure 5.5: MSE of normalized CFO $\hat{\varepsilon}$ estimate as a function of the SNR in AWGN channel using IDcell 0 preamble in segment 2 via maximum-likelihood estimation.

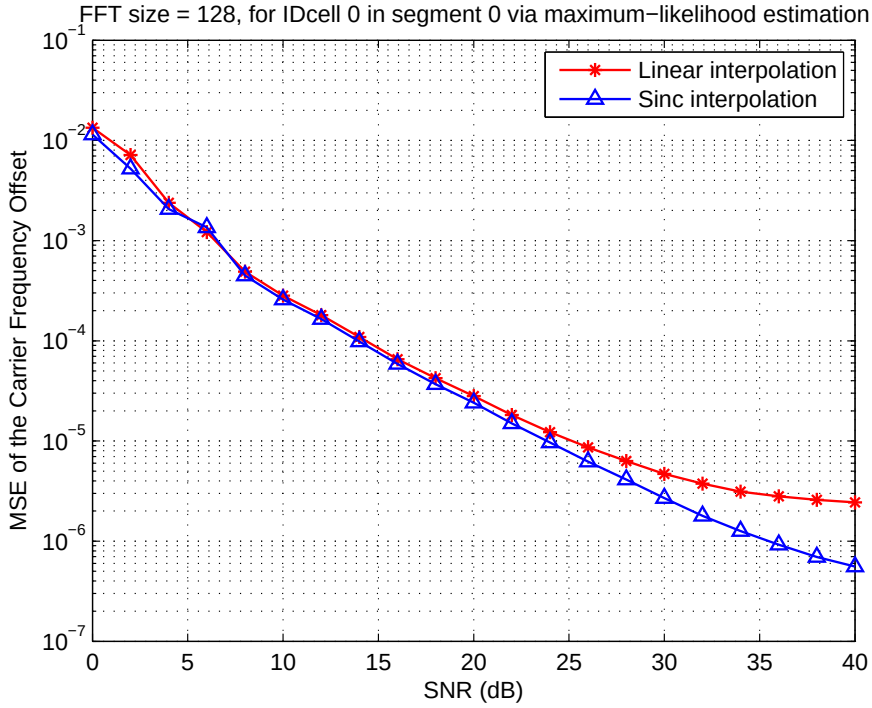

Figure 5.6: MSE of normalized CFO $\hat{\varepsilon}$ estimate as a function of the SNR in multipath fading channel using IDcell 0 preamble in segment 2 via maximum-likelihood estimation.

Chapter 6

Uplink Pilot-Assisted Frequency Synchronization via Interpolation

In this chapter, we consider the problem of estimating CFOs of all active users in the uplink communication of an OFDMA system. It is assumed that each user transmits a training block (carrying known symbols) at the beginning of the uplink frame for synchronization purposes. Our methods are only suitable for a subband-based carrier assignment scheme, where a group of adjacent subcarriers is allocated to one user so that signals from different users can be easily separated at the BS through a filter bank. Hence, if the preamble is still almost-periodic in time-domain as described in chapter 2, then the interpolation introduced in chapter 3 and the proposed algorithms introduced in chapter 4 can be applied for uplink environments.

6.1 Signal Models for OFDMA Uplink Transmissions

We consider the uplink of an OFDMA network in which Q active users simultaneously communicate with the BS as depicted in **Fig. 6.1**. The waveform arriving at the BS is given by the superposition of the signals from all active users. The frequency-domain subcarriers allocation of each active user for subband-based OFDMA is depicted in **Fig. 6.2**. We use N to denote the total number of subcarriers. In the presence of

CFOs, the time-domain received signal samples of the OFDMA block is given by

$$\begin{aligned} r(n) &= \sum_{q=1}^{Q} \{e^{\frac{j2\pi n\varepsilon_q}{N}} \frac{1}{\sqrt{N}} \sum_{k=0}^{N-1} X_{q,k} H_{q,k} e^{\frac{j2\pi nk}{N}}\} + w(n) \\ &= \sum_{q=1}^{Q} x_q(n) e^{\frac{j2\pi n\varepsilon_q}{N}} + w(n) \\ n &= 0, 1, 2, ...N-1 \end{aligned} \tag{6.1}$$

where $X_{q,k}$ is the transmitted frequency-domain complex data of the qth user, $H_{q,k}$ is the associated channel frequency responses of the qth user, $x_q(n)$ is the time-domain complex signal after passing $X_{q,k}$ through a multipath channel without both CFO and AWGN effect, ε_q is the qth CFO normalized to the subcarrier spacing and $w(n)$ is the noise contribution and it is modeled as a circularly symmetric white Gaussian process with variance $\sigma_v^2 = 2N_0$, where $N_0/2$ is the two-sided power spectral density of the thermal noise.

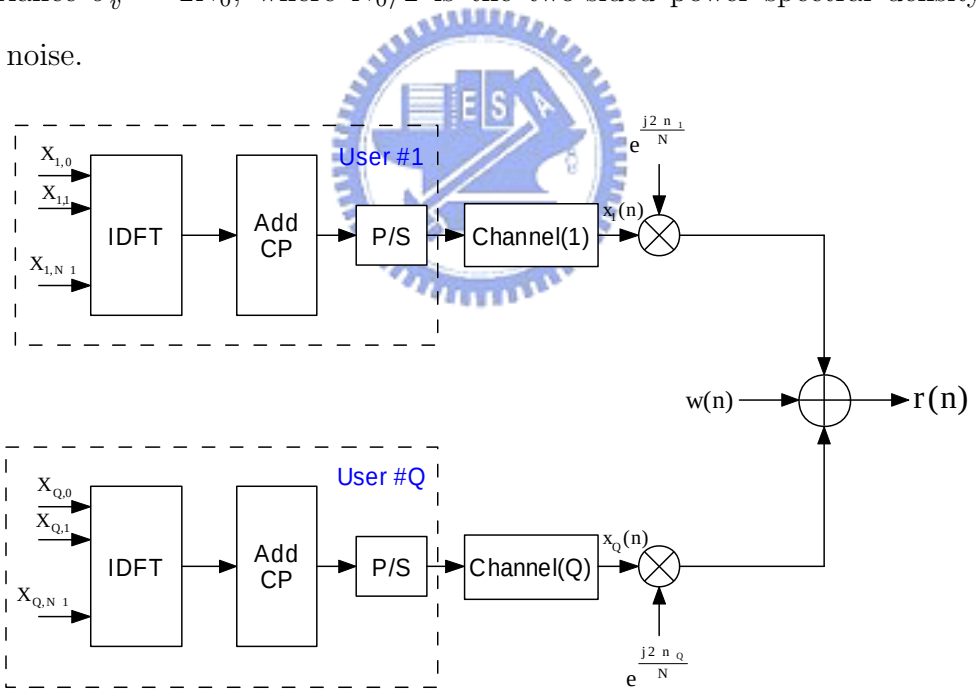

Figure 6.1: Discrete-time model of the baseband OFDMA system.

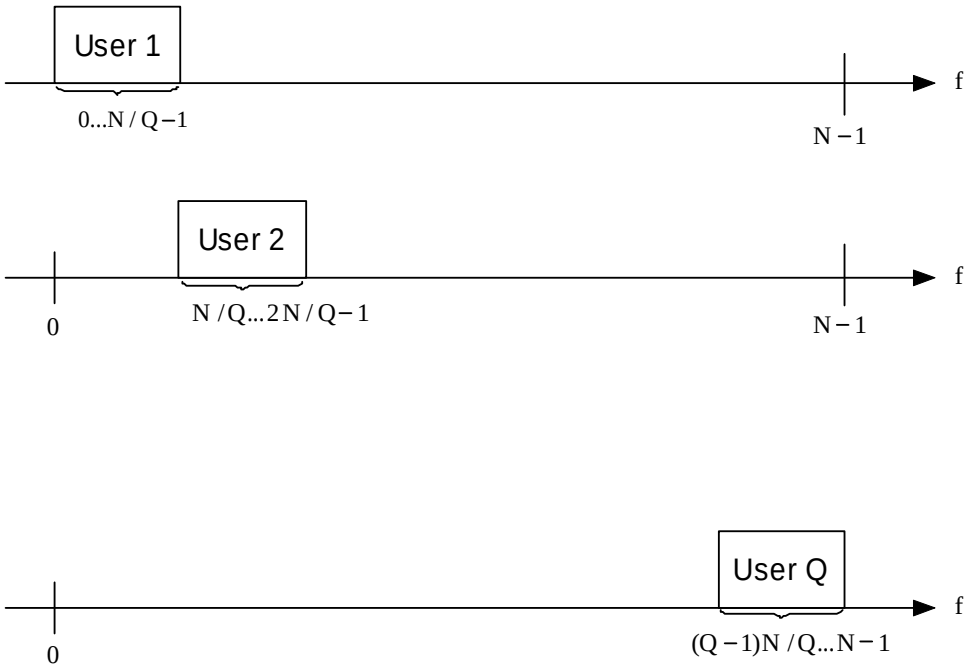

Figure 6.2: Frequency-domain subcarriers allocation for each active user.

6.2 Carrier Frequency Offset Estimation

When the time-domain signal $r(n)$ is received, we first transform to frequency-domain by FFT operation to obtain $R(k)$

$$R(k) = \sum_{n=0}^{N-1} r(n) e^{-\frac{j2\pi kn}{N}} \tag{6.2}$$

and utilize the frequency-domain filter bank to separate each user $R_q(k)$.

$$R_q(k) = \begin{cases} R(k), & (q-1)N/Q \le k \le qN/Q - 1 \\ 0, & otherwise \end{cases} \qquad 0 \le k \le N-1 \tag{6.3}$$

Then we transform the isolated frequency-domain signal of each active user $\{R_q(k)\}_{q=1}^{Q}$ into time-domain by IFFT operation to obtain $\{r_q(n)\}_{q=1}^{Q}$

$$r_q(n) = \frac{1}{\sqrt{N}} \sum_{k=0}^{N-1} R_q(k) e^{\frac{j2\pi nk}{N}} \tag{6.4}$$

and interpolations (chapter 3) follow IFFT operation. After that, we also have almost three identical parts. Finally, the time-domain correlation-based CFO estimation (chapter 4) can be performed well.

6.3 Simulation Results and Discussions

In this section, numerical results are presented to demonstrate the performance of our proposed design. The total number of subcarriers is 512 and is equally distributed among 4 active users. Hence, each active user has 128 subcarriers. From the simulation results, we have demonstrated that the interpolations can enhance the estimation accuracy when correlation-based fractional CFO estimation is implemented with almost-periodic preamble.

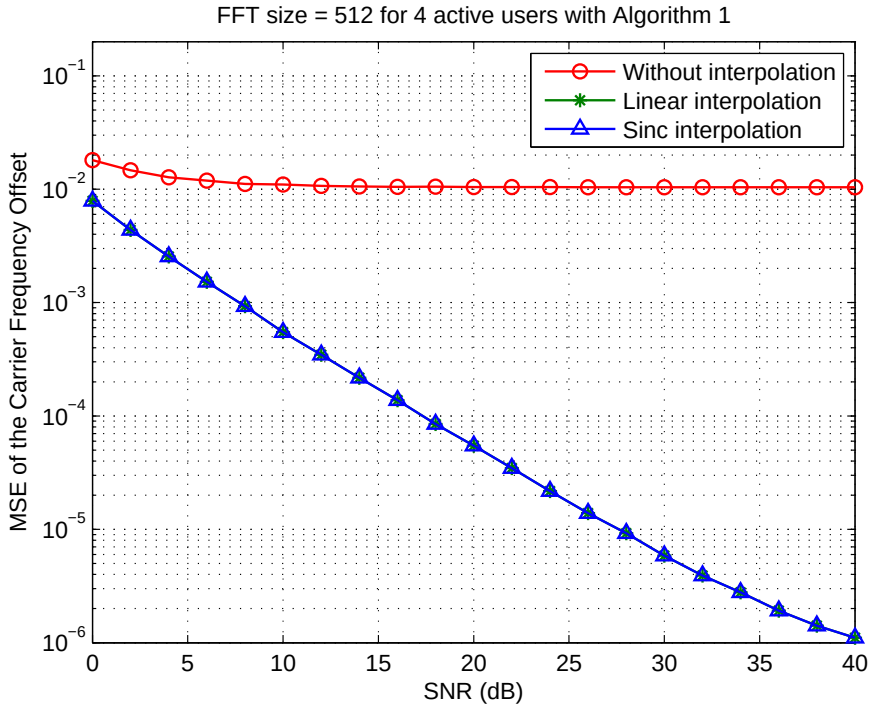

Figure 6.3: MSE of normalized CFO $\hat{\varepsilon}$ estimate as a function of the SNR in AWGN channel via Algorithm 1.

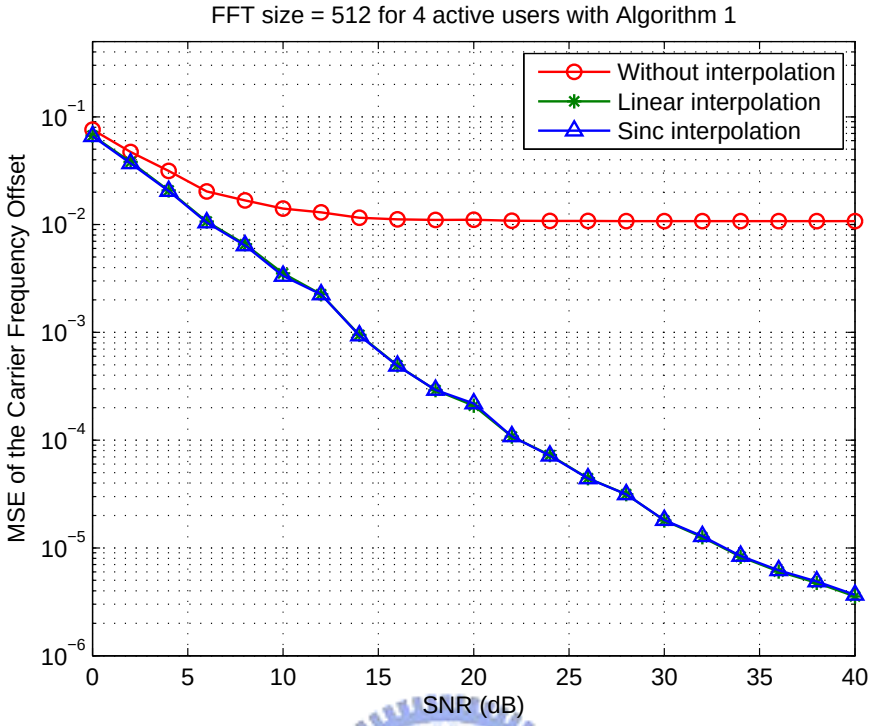

Figure 6.4: MSE of normalized CFO $\hat{\varepsilon}$ estimate as a function of the SNR in multipath fading channel via Algorithm 1.

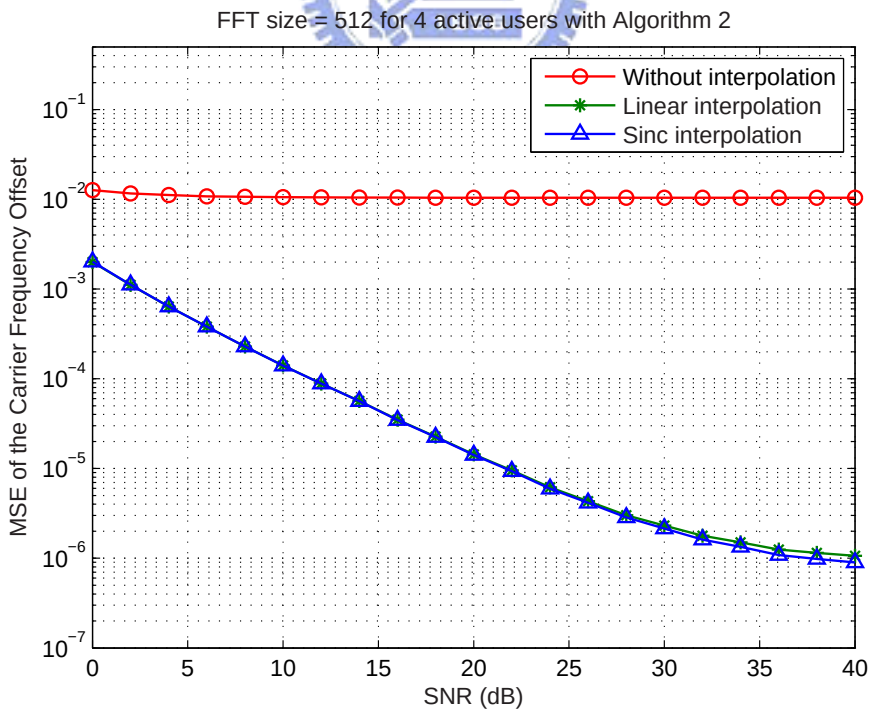

Figure 6.5: MSE of normalized CFO $\hat{\varepsilon}$ estimate as a function of the SNR in AWGN channel via Algorithm 2.

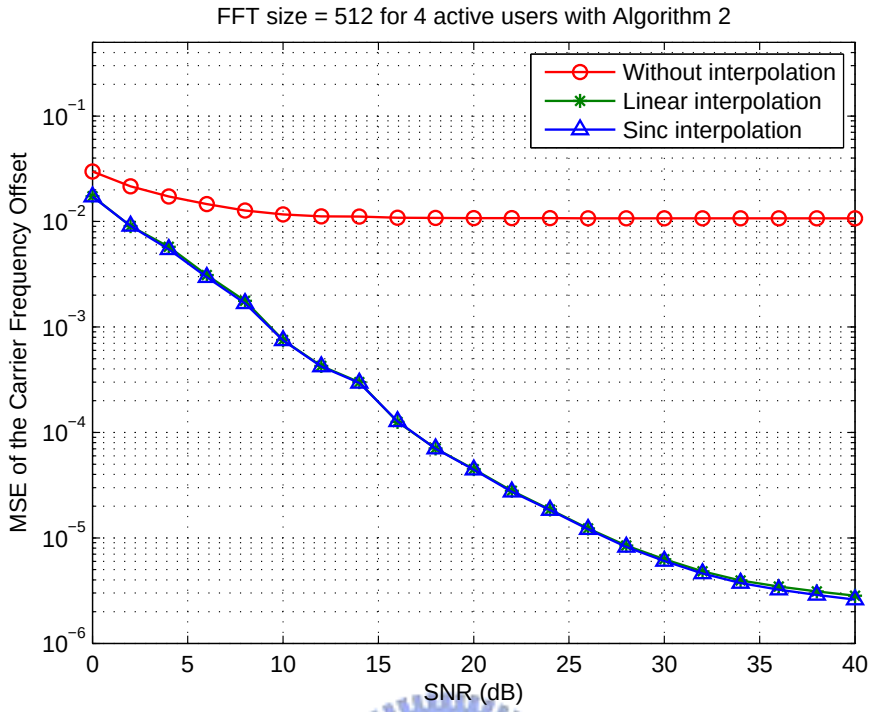

Figure 6.6: MSE of normalized CFO $\hat{\varepsilon}$ estimate as a function of the SNR in multipath fading channel via Algorithm 2.

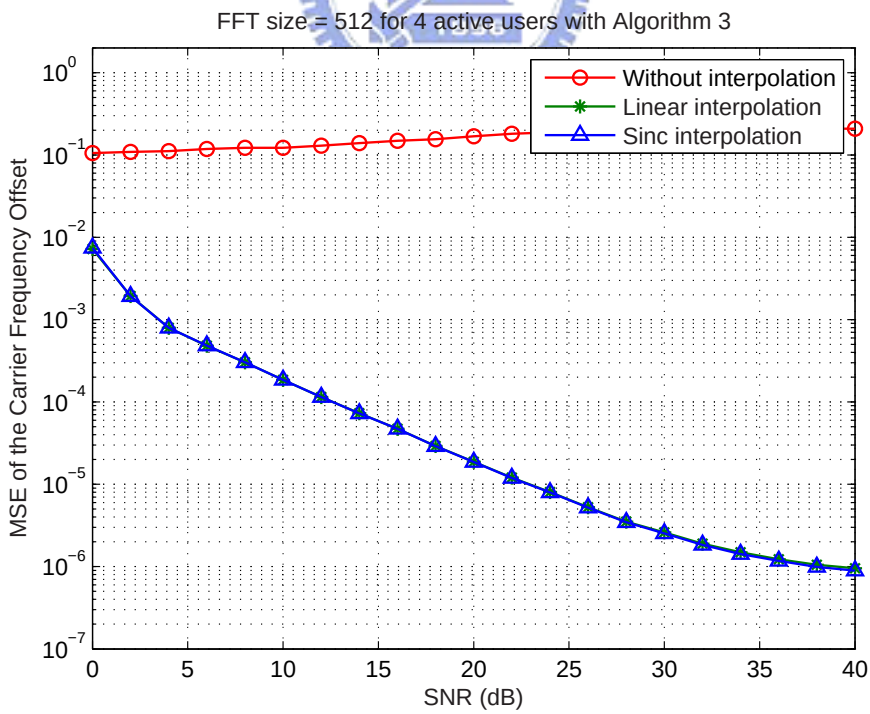

Figure 6.7: MSE of normalized CFO $\hat{\varepsilon}$ estimate as a function of the SNR in AWGN channel via Algorithm 3.

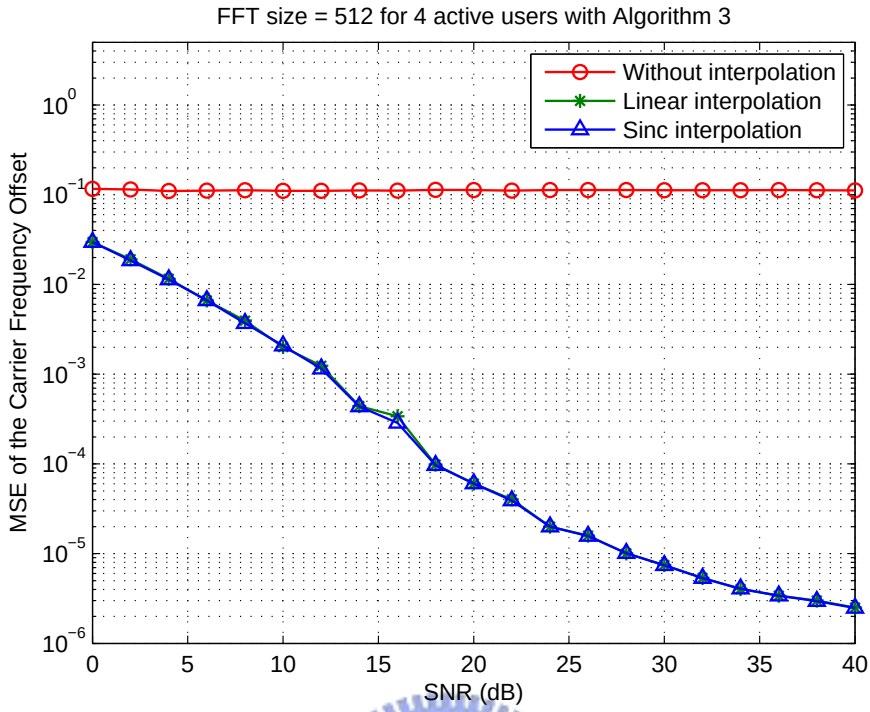

Figure 6.8: MSE of normalized CFO $\hat{\varepsilon}$ estimate as a function of the SNR in multipath fading channel via Algorithm 3.

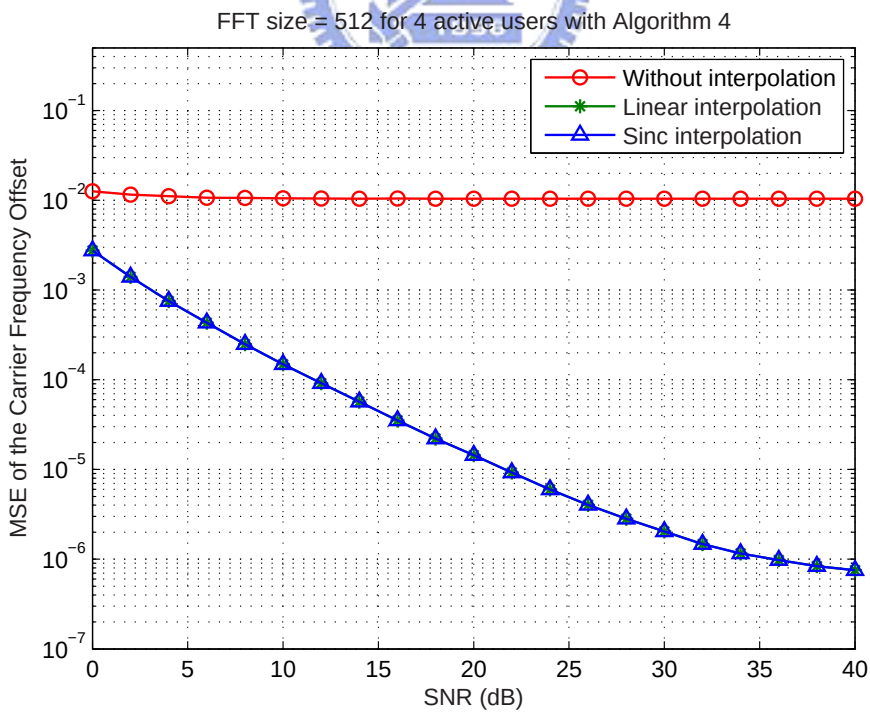

Figure 6.9: MSE of normalized CFO $\hat{\varepsilon}$ estimate as a function of the SNR in AWGN channel via Algorithm 4.

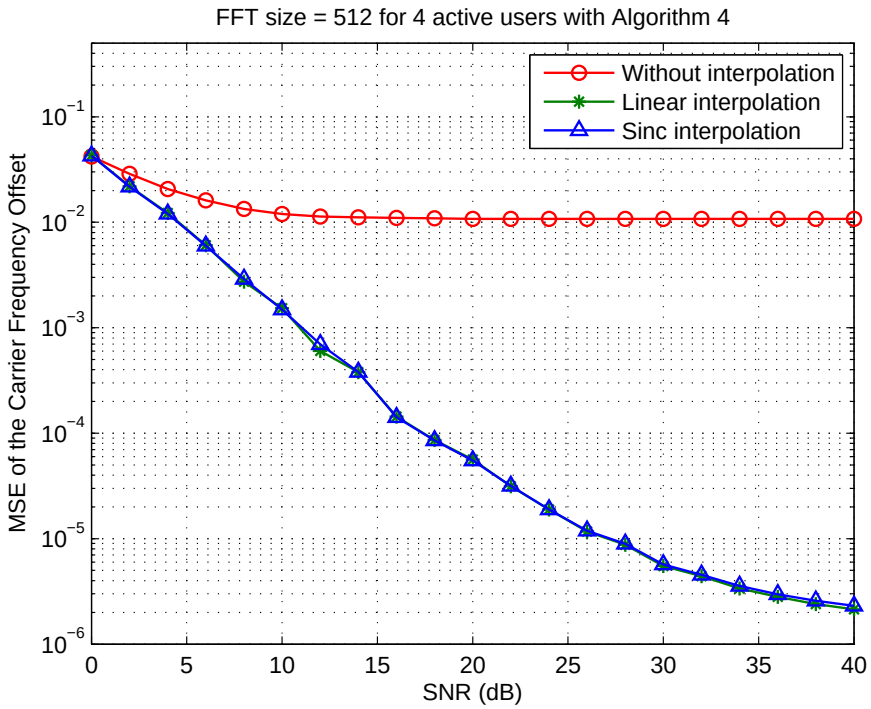

Figure 6.10: MSE of normalized CFO $\hat{\varepsilon}$ estimate as a function of the SNR in multipath fading channel via Algorithm 4.

Chapter 7

Conclusion

In this thesis, we consider the problem of pilot-aided estimation of the fractional CFO for TDD-OFDMA systems when the time domain pilot sequence has a almost-periodic structure. We propose an interpolation approach to reconstruct a periodic structure of the received pilot samples. Both linear and sinc-based interpolation filters are considered. The sinc-based filter yields better performance at high SNR region. We also find that the interpolation (performance) gain is an increasing function of SNR and depends on the pilot sequence length and channel condition. Dividing the pilot length of the WiMAX system by three, we obtain a remainder r which measures the degree of non-periodicity of the pilot length. The interpolation gain is more impressive when $r = 2$ than the $r = 1$ case. Numerical results also indicate the gain is larger in fading channels than in AWGN channels.

Appendix A

A Technical Overview of Physical Layer in Mobile WiMAX System

The term WiMAX (Worldwide Interoperability for Microwave Access) has become synonymous with the IEEE 802.16 Wireless Metropolitan Area Network (MAN) air interface standard. The IEEE 802.16 WirelessMAN standard provides specifications for an air interface for fixed, portable, and mobile Broadband Wireless Access (BWA) systems. The standard includes requirements for high data rate Line of Sight (LOS) operation in the 10-66 GHz range for fixed wireless networks as well as requirements for Non Line of Sight (NLOS) fixed, portable, and mobile systems operating in licensed and unlicensed bands from 2 to 11 GHz bands. The latest 802.16e amendment is supporting for mobility in WiMAX system. In this appendix, we provide a general introduction to IEEE 802.16e TDD OFDMA system.

A.1 WiMAX Architecture and Applications

Mobile WiMAX is a broadband wireless solution that enables convergence of mobile and fixed broadband networks through a common wide area broadband radio access technology and flexible network architecture. The Mobile WiMAX Air Interface adopts OFDMA for improved multi-path performance in non-line-of-sight environments. Scalable OFDMA (SOFDMA) is introduced in the IEEE 802.16e Amendment to support scalable channel bandwidths from 1.25 to 20 MHz.

A.2 OFDMA Sub-Channelization

Active (data and pilot) sub-carriers are grouped into subsets of sub-carriers called subchannels. The WiMAX OFDMA PHY [5] supports sub-channelization in both DL and UL. The minimum frequency-time resource unit of sub-channelization is one slot, which is equal to 48 data tones (sub-carriers).

There are two types of sub-carrier permutations for sub-channelization: *diversity* and *contiguous*. The diversity permutation draws sub-carriers pseudo-randomly to form a sub-channel. It provides frequency diversity and inter-cell interference averaging. The diversity permutations include DL FUSC (Fully Used Sub-Carrier), DL PUSC (Partially Used Sub-Carrier) and UL PUSC and additional optional permutations. With DL PUSC, for each pair of OFDM symbols, the available or usable sub-carriers are grouped into clusters containing 14 contiguous sub-carriers per symbol, with pilot and data allocations in each cluster in the even and odd symbols as shown in **Fig. A.1**.

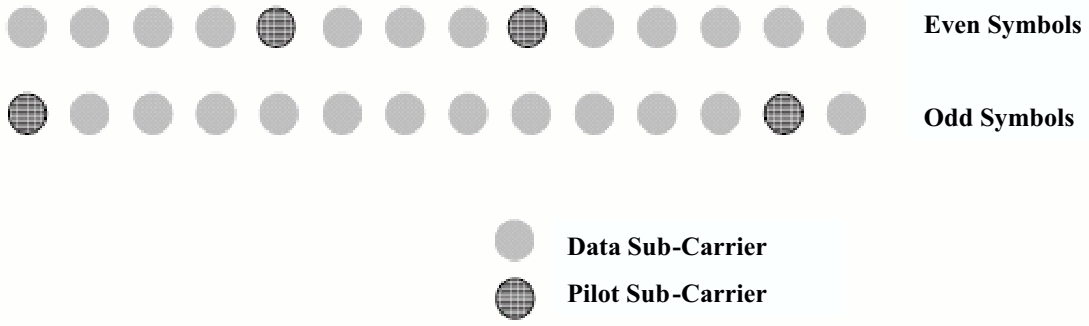

Figure A.1: DL Frequency Diverse Sub-Channel

A re-arranging scheme is used to form groups of clusters such that each group is made up of clusters that are distributed throughout the sub-carrier space. A sub-channel in a group contains two (2) clusters and is comprised of 48 data sub-carriers and eight (8) pilot subcarriers.

Analogous to the cluster structure for DL, a *tile* structure is defined for the UL PUSC whose format is shown in **Fig. A.2**.

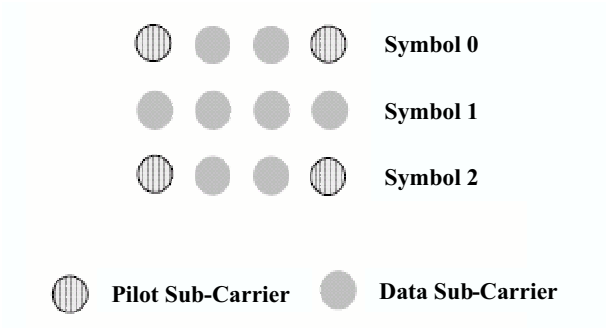

Figure A.2: Tile Structure for UL PUSC

The available sub-carrier space is split into tiles and six (6) tiles, chosen from across the entire spectrum by means of a re-arranging/permutation scheme, are grouped together to form a slot. The slot is comprised of 48 data sub-carriers and 24 pilot sub-carriers in 3 OFDM symbols.

The contiguous permutation groups a block of contiguous sub-carriers to form a subchannel. The contiguous permutations include DL AMC and UL AMC, and have the same structure. A bin consists of 9 contiguous sub-carriers in a symbol, with 8 assigned for data and one assigned for a pilot. A slot in AMC is defined as a collection of bins of the type (N x M = 6), where N is the number of contiguous bins and M is the number of contiguous symbols. Thus the allowed combinations are [(6 bins, 1 symbol), (3 bins, 2 symbols), (2 bins, 3 symbols), (1 bin, 6 symbols)]. AMC permutation enables multi-user diversity by choosing the sub-channel with the best frequency response.

In general, diversity sub-carrier permutations perform well in mobile applications while contiguous sub-carrier permutations are well suited for fixed, portable, or low mobility environments. These options enable the system designer to trade-off mobility for throughput.

Parameters	Values			
System Channel Bandwidth (MHz)	1.25	5	10	20
Sampling Frequency (F_p in MHz)	1.4	5.6	11.2	22.4
FFT Size (N_{FFT})	128	512	1024	2048
Number of Sub-Channels	2	8	16	32
Sub-Carrier Frequency Spacing	10.94kHz			
Useful Symbol Time ($T_b = 1/f$)	91.4 microseconds			
Guard Time ($T_g = T_b/8$)	11.4 microseconds			
OFDMA Symbol Duration ($T_s = T_b + T_g$)	102.9 microseconds			
Number of OFDMA Symbols (5 ms Frame)	48			

Table A.1: OFDMA Scalability Parameters

A.3 Scalable OFDMA

The IEEE 802.16e Wireless MAN OFDMA mode is based on the concept of scalable OFDMA (S-OFDMA). S-OFDMA supports a wide range of bandwidths to flexibly address the need for various spectrum allocation and usage model requirements. The scalability is supported by adjusting the FFT size while fixing the sub-carrier frequency spacing at 10.94 kHz. Since the resource unit sub-carrier bandwidth and symbol duration is fixed, the impact to higher layers is minimal when scaling the bandwidth. The S-OFDMA parameters are listed in **Tab. A.1**.

A.4 TDD Frame Structure

The 802.16e PHY supports TDD, FDD, and Half-Duplex FDD operation; however the initial release of Mobile WiMAX certification profiles will only include TDD. With ongoing releases, FDD profiles will be considered by the WiMAX Forum to address specific market opportunities where local spectrum regulatory requirements either prohibit TDD or are more suitable for FDD deployments. To counter interference issues, TDD does require system-wide synchronization; nevertheless, TDD is the preferred duplexing mode for the following reasons:

- TDD enables adjustment of the downlink/uplink ratio to efficiently support asym-

metric downlink/uplink traffic, while with FDD, downlink and uplink always have fixed and generally, equal DL and UL bandwidths.

- TDD assures channel reciprocity for better support of link adaptation, MIMO and other closed loop advanced antenna technologies.
- Unlike FDD, which requires a pair of channels, TDD only requires a single channel for both downlink and uplink providing greater flexibility for adaptation to varied global spectrum allocations.
- Transceiver designs for TDD implementations are less complex and therefore less expensive.

Figure A.3 illustrates the OFDM frame structure for a Time Division Duplex (TDD) implementation. Each frame is divided into DL and UL sub-frames separated by Transmit/Receive and Receive/Transmit Transition Gaps (TTG and RTG, respectively) to prevent DL and UL transmission collisions. In a frame, the following control information is used to ensure optimal system operation:

- **Preamble:** The preamble, used for synchronization, is the first OFDM symbol of the frame.
- **Frame Control Head (FCH):** The FCH follows the preamble. It provides the frame configuration information such as MAP message length and coding scheme and usable sub-channels.
- **DL-MAP and UL-MAP:** The DL-MAP and UL-MAP provide sub-channel allocation and other control information for the DL and UL sub-frames respectively.
- **UL Ranging:** The UL ranging sub-channel is allocated for mobile stations (MS) to perform closed-loop time, frequency, and power adjustment as well as bandwidth requests.

- **UL CQICH:** The UL CQICH channel is allocated for the MS to feedback channelstate information.

- **UL ACK:** The UL ACK is allocated for the MS to feedback DL HARQ acknowledgement.

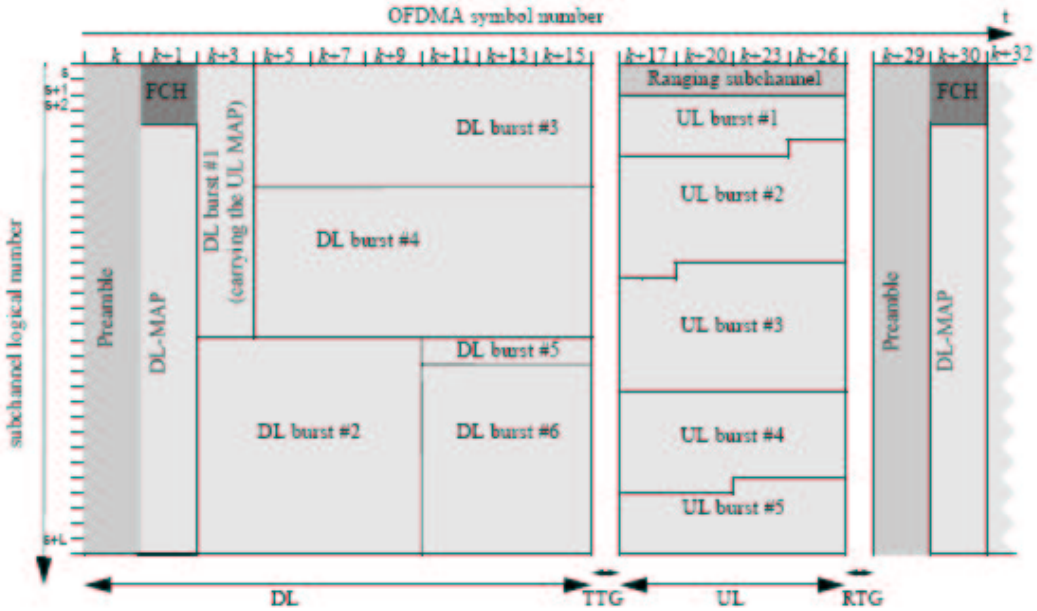

Figure A.3: WiMAX OFDMA Frame Structure

Index	IDcell	Segment	Series to modulate (in hexadecimal format)
0	0	0	0x01E52A9B3
1	1	0	0xC96FF8AB1
2	2	0	0xA1F5CE648
3	3	0	0x1E2BF6919
4	4	0	0x051798B72
5	5	0	0x932D7FA8E
6	6	0	0x2CBD50F73
7	7	0	0xF86F6A451
8	8	0	0x2BA44F7E7
9	9	0	0xEEFA172C3
10	10	0	0xFF46C729A
11	11	0	0x0362D5C61
12	12	0	0x27DDC7CA5
13	13	0	0x17EAEDAC6
14	14	0	0x94ACD9E03
15	15	0	0x1A1AC22DD
16	16	0	0xFD5E18DA6
17	17	0	0x35DEB6E0E
18	18	0	0xA0185E326
19	19	0	0x93B3F9C75
20	20	0	0x632481EA8
21	21	0	0x8BB8104A5
22	22	0	0x87C89EF75
23	23	0	0x207AA794C
24	24	0	0x6A4D1C403
25	25	0	0x7761B4BD7
26	26	0	0x31ABBF06D
27	27	0	0x69C6E455F
28	28	0	0xAB3B3CFF0
29	29	0	0x731412685
30	30	0	0xA3135C034
31	31	0	0xFECCB2B85
32	0	1	0xAA37BDA7C
33	1	1	0x90955CE1F
34	2	1	0xADBC1B844
35	3	1	0xA04A3B197
36	4	1	0x015E56CB3
37	5	1	0x64D6F4038

Table A.2: Preamble modulation series per segment and IDcell for the 128 FFT mode

Index	IDcell	Segment	Series to modulate (in hexadecimal format)
38	6	1	0xD2DD02238
39	7	1	0xFEA763CB2
40	8	1	0x8CE0D5FB6
41	9	1	0xCC25D7A7E
42	10	1	0x7019D3A92
43	11	1	0x784CF7EAB
44	12	1	0x07085DAC8
45	13	1	0x4CEEB5E1F
46	14	1	0x9E5CD5B80
47	15	1	0x63A76FD05
48	16	1	0xAA276F96F
49	17	1	0x3370F5082
50	18	1	0x35A644170
51	19	1	0x16FD73B8B
52	20	1	0xEEE990E94
53	21	1	0x28A3120FC
54	22	1	0xC2FBC2993
55	23	1	0x880BCACD3
56	24	1	0xAFA4DB918
57	25	1	0xAE1E49884
58	26	1	0xF7945E264
59	27	1	0x38374CA42
60	28	1	0x5AAE39B00
61	29	1	0x138069E54
62	30	1	0x966707005
63	31	1	0xA5037759E
64	0	2	0x3FE158D96
65	1	2	0xAED3B839F
66	2	2	0xF5AE23268
67	3	2	0x1895E68BE
68	4	2	0x1443C94EC
69	5	2	0x929547307
70	6	2	0xA17D3230C
71	7	2	0xD54FC0C33
72	8	2	0xAB77F079C
73	9	2	0xC3CA00A66
74	10	2	0x025519879
75	11	2	0x6CF39F815

Table A.3: Preamble modulation series per segment and IDcell for the 128 FFT mode (*continued*)

Index	IDcell	Segment	Series to modulate (in hexadecimal format)
76	12	2	0xF69E451B1
77	13	2	0x91BC72EBF
78	14	2	0xF964A5447
79	15	2	0xF8CD36F4A
80	16	2	0x726A3C802
81	17	2	0x118D1B682
82	18	2	0xDED9E703A
83	19	2	0x3E8929773
84	20	2	0x2C64AA7F9
85	21	2	0x2249CEA0F
86	22	2	0x01363A94E
87	23	2	0x69D77721F
88	24	2	0xAE103C9B9
89	25	2	0x89E2A6940
90	26	2	0xA7BC42645
91	27	2	0xBBB6B9C0F
92	28	2	0x5BF7598F8
93	29	2	0x4AE4C79FE
94	30	2	0x1FDC748C9
95	31	2	0x877D5E6E4
96	0	0	0x0FE322452
97	1	1	0x4DC778B5F
98	2	2	0xADD9E3F88
99	3	0	0x2C1C857DC
100	4	1	0xCFB4B5503
101	5	2	0xCD8505E21
102	6	0	0x82892F4CE
103	7	1	0x3979FD176
104	8	2	0x5FA49C311
105	9	0	0xBA7857B19
106	10	1	0xBC030C4CA
107	11	2	0x517F3CBD6
108	12	0	0x7E545BE73
109	13	1	0xDDCA69C3F
110	14	2	0xA01A2C8C7
111	15	0	0x1C0B64435
112	16	1	0x330282DF2
113	17	2	0x147FCCF4B

Table A.4: Preamble modulation series per segment and IDcell for the 128 FFT mode (*continued*)

Bibliography

[1] *Local and Metropolitan Area Networks–Part 16: Air Interface for Fixed Broadband Wireless Access Systems*, IEEE Standard 802.16-2004, Oct. 2004.

[2] *Corrigendum to IEEE Standard for Local and Metropolitan Area Networks–Part 16: Air Interface for Fixed Broadband Wireless Access Systems*, IEEE Standard P802.16-2004/Cor1/D5, Sep. 2005.

[3] *Local and Metropolitan Area Networks–Part 16: Air Interface for Fixed and Mobile Broadband Wireless Access Systems–Amendment for Physical and Medium Access Control Layers for Combined Fixed and Mobile Operation in Licensed Bands*, IEEE P802.16e/D12, Oct. 2005.

[4] *Local and Metropolitan Area Networks–Part 16: Air Interface for Fixed and Mobile Broadband Wireless Access Systems–Amendment2: Physical and Medium Access Control Layers for Combined Fixed and Mobile Operation in Licensed Bands and Corrigendum 1*, IEEE Std 802.16e^{TM}-2005 and IEEE Std 802.16^{TM}-2004/Cor 1-2005, Feb. 2006.

[5] H. Yagoobi, "Scalable OFDMA physical layer in IEEE 802.16 WirelessMAN," *Intel Technology Journal*, vol. 8, Aug. 2004.

[6] *Part II: Wireless LAN Medium Access Control (MAC) and Physical Layer (PHY) Specifications: High-Speed Physical Layer in the 5 GHz Band*, IEEE Standard 802.11a-1999, Sep. 1999.

[7] Broadband Radio Access Networks (BRAN); High Performance Radio Local Area Networks (HIPERLAN) Type 2, System Overview, ETSI TR 101 683, v0.1.2, 1999.

[8] G. L. Stüber, J. R. Barry, S. W. Mclaughlin, Y. (G.) Li, M. A. Ingram, and T. G. Pratt, "Broadband MIMO-OFDM wireless communications," *IEEE Proceedings*, vol. 92, no. 2, pp. 271-294, Feb. 2004.

[9] I. Barhumi, G. Leus, and M. Moonen, "Optimal training design for MIMO OFDM systems in mobile wireless channels," *IEEE Trans. Signal Process.*, vol. 51, no. 6, pp. 1615-1624, Jun. 2003.

[10] X. Ma, M.-K. Oh, G. B. Giannakis, and D.-J. Park, "Hopping pilots for estimation of frequency-offset and multiantenna channels in MIMO-OFDM," *IEEE Trans. Commun.*, vol. 53, no. 1, pp. 162-172, Jan. 2005.

[11] A. van Zelst, and T. C. W. Schenk, "Implementation of a MIMO OFDM-based wireless LAN system," *IEEE Trans. Signal Process.*, vol. 52, no. 2, pp. 483-494, Feb. 2004.

[12] P. H. Moose, "A technique for orthogonal frequency division multiplexing frequency offset correction," *IEEE. Trans. Commun.*, vol. 42, pp. 2908-2914, Oct. 1994.

[13] T. M. Schmidl and D. C. Cox, "Robust frequency and timing synchronization for OFDM," *IEEE Trans. Commun.*, vol. 45, no. 12, pp. 1613-1621, Dec. 1997.

[14] J. J. van de Beek, M. Sandell, and P. O. Borjesson, "ML estimation of time and frequency offset in OFDM systems," *IEEE Trans. Signal Process.*, vol. 45, no. 7, pp. 1800-1805, Jul. 1997.

[15] B. Chen and H. Wang, "Blind estimation of OFDM carrier frequency offset via oversampling," *IEEE Trans. Signal Process.*, vol. 52, No. 7, pp. 2047-2057, Jul. 2004.

[16] J. H. Yu and Y. T. Su, "Pilot-assisted maximum-likelihood frequency-offset estimation for OFDM systems," *IEEE Trans. Commun.*, vol. 52, no. 11, pp. 1997-2008, Nov. 2004.

[17] T. Lv, H. Li, and J. Chen, "Joint estimation of symbol timing and carrier frequency offset of OFDM signals over fast time-varying multipath channels," *IEEE Trans. Signal Process.*, vol. 53, no. 12, pp. 4526-4535, Dec. 2005.

[18] Z. Zhang, K. Long, M. Zhao, and Y. Liu, "Joint frame synchronization and frequency offset estimation in OFDM systems," *IEEE Trans. Broadcast.*, vol. 51, no. 3, pp. 389-394, Sep. 2005.

[19] C. C. Ko, R. Mo, and M. Shi, "A new data rotation based CP synchronization scheme for OFDM systems," *IEEE Trans. Broadcast.*, vol. 51, no. 3, pp. 315-321, Sep. 2005.

[20] P. Y. Tsai, H. Y. Kang, and T. D. Chiueh, "Joint weighted least-squares estimation of carrier-frequency offset and timing offset for OFDM systems over multipath fading channels," *IEEE Trans. Veh. Technol.*, vol. 54, no. 1, pp. 211-223, Jan. 2005.

[21] M.-O. Pun, M. Morelli, and C.-C. Jay Kuo, "Maximum-likelihood synchronization and channel estimation for OFDMA uplink transmissions," *IEEE Trans. Commun.*, vol. 54, no. 4, pp. 726-736, Apr. 2006.

[22] Z. Cao, U. Tureli, and Y.-D. Yao, "Deterministic multiuser carrier-frequency offset estimaion for interleaved OFDMA uplink," *IEEE Trans. Commun.*, vol. 52, no. 9, pp. 1585-1594, Sep. 2004.

[23] M. Morelli, "Timing and frequency synchronization for the uplink of an OFDMA system," *IEEE Trans. Commun.*, vol. 52, no. 2, pp. 296-306, Feb. 2004.

[24] S.-H. Tsai, Y.-P. Lin, and C.-C. Jay Kuo, "An approximately MAI-free multiaccess OFDM system in carrier frequency offset environment," *IEEE Trans. Signal Process.*, vol. 53, no. 11, pp. 4339-4353, Nov. 2005.

[25] D. Huang and K. B. Letaief, "An interference-cancellation scheme for carrier frequency offsets correction in OFDMA systems," *IEEE Trans. Commun.*, vol. 53, no. 7, pp. 1155-1165, Jul. 2005.

[26] A. V. Oppenheim and R. W. Schafer, *Discrete-Time Signal Processing*, Second Edition, Prentice Hall, 1999.

[27] S. K. Mitra, *Digital Signal Processing*, Third Edition, McGraw-Hill, 2006.

[28] J. G. Proakis and D. G. Manolakis, *Digital Signal Processing*, Third Edition, Prentice Hall, 1996.

[29] J. G. Proakis, *Digital Communications*, Fourth Edition, New York: McGraw-Hill, 2001.

[30] W. C. Jakes, Jr., Ed., *Microwave Mobile Communications*, New York: Wiley, Jun. 1974.

[31] X. Wang and H. V. Poor, *Wireless Communication Systems: Advanced Techniques for Signal Reception*, Prentice Hall, 2004.

[32] L. Hanzo, S. X. Ng, T. Keller, and W. Webb, *Quadrature Amplitude Modulation*, Second Edition, John Wiley & Sons, 2004.

[33] M. K. Simon and M.-S. Alouini, *Digial Communication over Fading Channels*, Second Edition, John Wiley & Sons, 2005.

[34] S. Glisic, *Advanced Wireless Communications*, John Wiley & Sons, 2004.

[35] L. Hanzo, M. Münster, B. J. Choi, and T. Keller, *OFDM and MC-CDMA*, John Wiley & Sons, 2003.